ISSN 2732–0189 (Online)
ISSN 1586–2070 (Print)

JOURNAL OF COMPUTATIONAL AND APPLIED MECHANICS

An Open Access International Journal

Published by the University of Miskolc

VOLUME 17, NUMBER 1 (2022)

MISKOLC UNIVERSITY PRESS

ISSN 2732–0189 (Online)
ISSN 1586–2070 (Print)

JOURNAL OF COMPUTATIONAL AND APPLIED MECHANICS

An Open Access International Journal

Published by the University of Miskolc

VOLUME 17 NUMBER 1 (2022)

MISKOLC UNIVERSITY PRESS

Journal of Computational and Applied Mechanics, Vol. 17, No. 1, (2022), pp. 3–14
DOI: 10.32973/jcam.2022.001

MATHEMATICAL ASPECTS OF NON-FOURIER HEAT EQUATIONS

Róbert Kovács
Department of Energy Engineering, Budapest University of Technology and Economics
Műegyetem rkp. 3., H-1111, Budapest, Hungary
Department of Theoretical Physics, Wigner Research Centre for Physics, Hungary
kovacsrobert@energia.bme.hu

[Received: January 21, 2022; Accepted: March 12, 2022]

Abstract. Due to technological advancement, as materials with complex structures (e.g., metamaterials and foams) appear in practice there is a need to develop advanced thermal models. These are called non-Fourier equations, and all have particular mathematical properties differing from the conventional attributes of Fourier's law. The present paper discusses the thermodynamic origin of non-Fourier equations and their consequences. The second law of thermodynamics influences the relations among the material parameters, and therefore, it restricts how the temperature-dependent properties can be included in the model. Furthermore, we present the properties of initial and boundary conditions, since these are crucial in solving any practical problems and are different from the usual interpretation used for the Fourier equation.

Mathematical Subject Classification: 35B30, 35B09, 35E20
Keywords: generalised heat conduction, nonequilibrium thermodynamics, nonlinearities

1. Introduction

In engineering practice, continuum models are used to describe the behaviour of fluids and solids in space and time, usually utilising a finite element method. These software consist of knowledge about all the classical equations for fluid flow, solid mechanics and heat transfer. While this is suitable in numerous situations, there are cases in which these conventional methods are not applicable, such as the thermal modelling of thin layers [1, 2] and heterogeneous materials [3, 4, 5]. These, in general, can be described with advanced models in which the classical Fourier equation is extended with new space and time derivatives, forming the so-called non-Fourier models [6, 7].

Fourier's law prescribes a proportionality between the heat flux and the temperature gradient. That relation eases the initial and boundary conditions definitions as showing a straightforward connection between the field variables. However, this is not the case for non-Fourier equations. The Fourier constitutive equation is exchanged with a (partial) differential equation, thus modelling a significantly more complex relationship between the heat flux and temperature gradient. This generalisation has far-reaching consequences in the mathematical treatment of heat equations.

Therefore, this paper aims to present the aforementioned essential consequences related to initial and boundary conditions. Furthermore, we also present a less-known attribute that becomes crucial for nonlinearities: the functional dependence of the coefficients. These together are the most common aspects needed for engineers in the problem-solving procedure. It is challenging to obtain physically sound and reliable solutions without clarifying these properties.

In what follows, we begin with the thermodynamic background, from which it becomes visible how the coefficients in the equations (interpreted as material parameters) are connected. After that, we place our focus on the initial and boundary conditions by presenting the critical steps in the solution method.

2. Thermodynamics of heat equations

While the approach of Classical Irreversible Thermodynamics (CIT) [8] was successful, it turned out that its basic hypothesis about local equilibrium is a substantial restriction, and therefore other ways must be discovered for the description of non-equilibrium phenomena. Thus numerous thermodynamic approaches have been developed in recent decades, such as Extended Irreversible Thermodynamics (EIT) [9, 10], Rational Extended Thermodynamics (RET) [11], GENERIC [12, 13] and the framework of internal variables [14, 15, 16, 17, 18]. Each approach has its specific advantages and disadvantages, depending on the particular problem. For instance, RET is better for rarefied gaseous materials but cannot be used for macroscale solids at room temperature. GENERIC is helpful in constructing numerical methods, and EIT fits best for low-temperature (< 20 K) problems.

For our purpose, the approach of internal variables is the best option as this theory does not restrict the model either to rarefied or low-temperature states. In that sense, it is more general than the other thermodynamic theories, since this approach does not necessarily introduce variables with strict physical interpretation. It restricts the tensorial order of the variable and fixes how that variable contributes to the potential functions entropy and internal energy, but leaves open its exact physical meaning, being understood as an 'internal degree of freedom'. For our purpose, that freedom is not necessary, and to obtain compatibility with EIT, that internal variable can be identified as the heat flux, thus it is a non-equilibrium contribution to the heat conduction process. We focus on two non-Fourier heat equations in the following. These are the Maxwell-Cattaneo-Vernotte (MCV) [19, 20] and Guyer-Krumhansl (GK) [21] equations. These are the most common models in the non-Fourier literature. The GK equation seems to be the next reasonable and practically important extension of Fourier's law due to its advantageous properties [22]. For the detailed derivation, we refer to the work of Fülöp and Ván [23, 24]; here we show only the essential steps and outcomes.

2.1. Fourier equation.

The derivation of constitutive equations - such as Fourier's law - is based on the balance of entropy density s. In CIT, s depends only on the specific internal energy e. Together with the entropy density current $\mathbf{J}_s = \mathbf{q}/T$ (with T is the temperature and $\mathbf{q}$ is the heat flux), it is possible to determine the entropy

production (σ_s) using the balance equation,

$$\rho\dot{s} + \nabla \cdot \mathbf{J}_s = \sigma_s \geq 0, \tag{2.1}$$

where the upper dot represents the time derivative and $\nabla\cdot$ stands for the divergence. Eq. (2.1) mathematically forms the second law of thermodynamics for continuum systems [25]. It is a balance equation for entropy density, which is a concave potential function of e, thus having a maxima at the equilibrium. The entropy production σ_s appears as a source term, and that must be positive semi-definite, $\sigma_s = 0$ only in equilibrium for dissipative phenomena. Mathematically, the solution of $\sigma_s \geq 0$ results in the constitutive relations. Interestingly, while infinitely many solutions are possible [28], mostly the linear solutions are investigated as they are simple enough to understand, interpret and implement in practice. To obtain Fourier's law, after substitution, (2.1) leads to the Onsagerian equation [26, 27],

$$\sigma_s = \mathbf{q} \cdot \nabla \frac{1}{T} \geq 0, \tag{2.2}$$

for which we choose a linear solution,

$$\mathbf{q} = \frac{l}{T^2}\nabla T = -\lambda \nabla T = -\lambda \ \mathrm{grad}T. \tag{2.3}$$

This is called Fourier's law, and the thermal conductivity λ is naturally formed by a positive coefficient $l > 0$ to satisfy the inequality's positive semi-definiteness. The calculation of entropy production requires the balance of internal energy e,

$$\rho\dot{e} + \nabla \cdot \mathbf{q} = 0, \tag{2.4}$$

in which we neglected the volumetric heat sources, and $e = cT$ is considered with c being the isochoric specific heat. Here, we restrict ourselves to rigid materials in order to clearly reveal the difficulties and the limits of the theory. The derivation of non-Fourier equations with internal variables repeats this procedure.

2.2. **Models beyond Fourier.** In any of the generalised thermodynamic theories, the variable space is extended with a new type of non-equilibrium variable. In the internal variable approach, that non-equilibrium variable is not necessarily interpreted or connected to a known physical quantity, merely its existence and its tensorial order are restricted. In other words, one can suppose that $s = s(e, \xi)$, where ξ is a vectorial quantity. This is a general approach indeed. However, we do not need to keep this level of generality to derive the MCV and GK equations. Instead, it is possible to identify ξ with the heat flux $\mathbf{q}$ at that step, achieving compatibility with EIT and RET [29], i.e., having $s = s(e, \mathbf{q})$, which must be a concave function. The concavity is ensured by using

$$s(e, \mathbf{q}) = s_{eq}(e) - \frac{m}{2}\mathbf{q}^2, \tag{2.5}$$

where the first term $s_{eq}(e)$ expresses the classical local equilibrium assumption and $\frac{m}{2}\mathbf{q}^2$ represents a deviation from this local equilibrium with $m \geq 0$. The derivation also requires $\mathbf{J}_s$. According to the paper [24], $\mathbf{J}_s$ can be formulated using a so-called Nyíri multiplier ($\mathbf{B}$), as $\mathbf{J}_s = \mathbf{B}\mathbf{q}$ [30]. In EIT, $\mathbf{J}_s = \frac{\mathbf{q}}{T} + \mu\nabla\mathbf{q} \cdot \mathbf{q}$ is used. These approaches are equivalent, as the inequality (2.1) automatically restricts $\mathbf{B}$ so that

$\mathbf{B} = \frac{1}{T}\mathbf{I} + \mu\nabla\mathbf{q}$ holds. Recently, Szücs et al. showed [31] that $\mathbf{J}_s = \frac{\mathbf{q}}{T} + \mathbf{B}\mathbf{q}$ is a more natural introduction of a current multiplier $\mathbf{B}$ as it is $\mathbf{B} = \nabla\mathbf{q}$, thus having a more direct and clear physical interpretation. The entropy production becomes

$$\sigma_s = \nabla\mathbf{q} : \left(\mathbf{B} - \frac{1}{T}\mathbf{I}\right) + \mathbf{q}\cdot(\nabla\cdot\mathbf{B} - \rho m\dot{\mathbf{q}}) \geq 0, \tag{2.6}$$

and its solution, the Onsagerian relations are

$$\begin{aligned} \mathbf{B} - \frac{1}{T}\mathbf{I} &= l_1\nabla\mathbf{q}, \\ \nabla\cdot\mathbf{B} - \rho m\dot{\mathbf{q}} &= l_2\mathbf{q}, \end{aligned} \tag{2.7}$$

with $l_1, l_2, m \geq 0$, furthermore

$$\tau = \frac{\rho m}{l_2}, \quad \lambda = \frac{1}{l_2 T^2}, \quad \kappa^2 = \frac{l_1}{l_2}, \tag{2.8}$$

forming the coefficients of the GK equation, which reads

$$\tau\partial_t q + q = -\lambda\partial_x T + \kappa^2\partial_{xx} q \tag{2.9}$$

in one spatial dimension for simplicity. If $l_1 = 0$, the model reduces to the MCV equation, i.e., $\kappa^2 = 0$ and

$$\tau\partial_t q + q = -\lambda\partial_x T. \tag{2.10}$$

The MCV and GK constitutive equations (2.9)-(2.10) are coupled to the internal energy balance (2.4), and thus form a mathematically and physically complete system of equations, describing the time evolution of temperature and heat flux in space and time.

Initially, the GK equation is derived on the basis of kinetic theory and therefore the coefficients (2.8) are strictly restricted to a particular heat transfer mechanism. That original approach would not be applicable for engineering problems in general. However, the present continuum model does not require assumptions about the heat conduction mechanism prior to the derivation. Therefore the coefficients (2.8) can be freely adjusted and fitted to experiments, as is usual with the thermal conductivity λ in the Fourier equation. Consequently, while the form of the GK equation remains the same, the coefficients differ from the original case. Therefore, in this sense, the internal variable approach extends the range of validity.

3. Nonlinear models

It is well-known that the behaviour of materials depends on numerous factors. Here, for demonstration, we consider only the temperature dependence of the coefficients defined by (2.8) and appearing in the GK equation (2.9). We want to emphasise that the new thermal parameters (τ and κ^2) are not independent of the thermal conductivity λ and are connected through the Onsagerian relations. This is demonstrated in the following.

Let us suppose that $\lambda(T) = \lambda_0 \exp\big(a(T - T_0)\big)$, with λ_0 being thermal conductivity at a reference temperature T_0. Consequently,

$$\frac{1}{l_2 T^2} = \lambda_0 e^{a(T-T_0)} \Rightarrow \frac{1}{l_2} = \lambda_0 T^2 e^{a(T-T_0)} \Rightarrow l_2 = \frac{1}{\lambda_0 T^2} e^{-a(T-T_0)} \tag{3.1}$$

restricts one Onsagerian coefficient l_2. Moreover, as l_2 is also present in both coefficients τ and κ^2, it influences their treatment. This follows from The second law of thermodynamics directly, and has an impact on the entire model, that is,

$$\tau = \frac{\rho m}{l_2} = \rho m \lambda_0 T^2 e^{a(T-T_0)}, \quad \kappa^2 = \frac{l_1}{l_2} = l_1 \lambda_0 T^2 e^{a(T-T_0)}. \tag{3.2}$$

Interestingly, κ^2 alone can depend on the temperature through l_1.

Now let us assume a more complex situation, i.e., both τ and λ possess a linear temperature dependence

$$\lambda(T) = \lambda_0 + a(T - T_0), \quad \text{and} \quad \tau(T) = \tau_0 + b(T - T_0), \tag{3.3}$$

from which

$$l_2 = \frac{1}{\big(\lambda_0 + a(T - T_0)\big)T^2}, \quad \text{and} \quad \rho m = \frac{\tau_0 + b(T - T_0)}{\big(\lambda_0 + a(T - T_0)\big)T^2} \tag{3.4}$$

follows [32]. This is a real, experimentally measured set of parameters. Interestingly, we have a choice about which coefficient is assigned to satisfy (3.4), either ρ, m or both can be temperature dependent. If m alone becomes a function of the temperature, then it introduces further terms into the constitutive equation being proportional with $\mathrm{d}m/\mathrm{d}T$. If ρ is considered to be a function of T, then the introduction of the mechanical field is essential in order to take account of thermal expansion with the corresponding balance equations and its contribution to the internal energy [33]. The temperature dependence of κ^2, however, is still an open question, as experimental data are lacking. Although that parameter is experimentally determined for various heterogeneous materials at room temperature [34], the reference temperature is not yet varied. Either way, the derivation must be restarted in order to preserve the physical and mathematical consistency [32]. This is a notable difference compared to the Fourier equation.

Overall, even the simplest nonlinearity originating in the state dependence of the material coefficients can make the situation significantly more difficult. While this is common for Fourier's law, it is not straightforward for a non-Fourier equation. Without a proper thermodynamic background, one cannot discover the relationship of the coefficients. This is one reason, among many others, why the so-called dual phase lag (DPL) model is not recommended. This is an ad hoc model, based on the assumption that there is a time lag for both the heat flux and the temperature gradient [35],

$$q(x, t + \tau_q) = -\lambda \partial_x T(x, t + \tau_T). \tag{3.5}$$

Usually, Taylor series expansion is utilised on (3.5) up to an arbitrarily decided order. This manifests in ill-posed problems and instability [36, 37, 38, 39, 40, 41]. However, in a particular case, that model might be reduced to the MCV equation (2.10) and could

be viable for strictly restricted situations. However, as a thermodynamic background is missing, it is impossible to recover the connection between the two relaxation times τ_q and τ_T. Together with the mathematical issues, this is a severe limitation on the model, and thus it is not possible to reliably implement the DPL model for practical engineering tasks.

4. Initial and boundary conditions

To be clear with the analogies among Fourier and non-Fourier models, we first briefly discuss the classical approach for one spatial dimension. For the Fourier equation, the usual initial condition is straightforward: the temperature distribution ($T(x, t = 0) = T_0(x)$) must be given at the initial time instant. For instance, $T_0(x)$ is also enough to calculate the initial heat flux $q_0(x)$. However, this is valid only for the T-representation of the Fourier heat equation (4.1). In case of q-representation (4.2), only q can be defined at the initial time instant since the temperature as a variable is completely missing in that situation. In other words, we have a choice of which field variable we eliminate using Eqs. (2.3) and (2.4):

$$\text{T-representation:} \qquad \partial_t T = \alpha \partial_{xx} T, \tag{4.1}$$

$$\text{q-representation:} \qquad \partial_t q = \alpha \partial_{xx} q, \tag{4.2}$$

where $\alpha = \lambda/(\rho c)$ is the thermal diffusivity with constant coefficients. While Eq. (4.1) is well-known in the literature, Eq. (4.2) is usually omitted. The q-representation could be useful for analytical solutions as here the heat flux q is treated as a first-type boundary condition. For certain situations, it could be more suitable, such as for time-dependent heat flux boundaries. After obtaining the time and space evolution of q, the temperature field can be recovered using the balance of internal energy (2.4). Furthermore, that form also reveals an interesting aspect. Eq. (4.2) also allows us to define the gradient of the heat flux as a second-type boundary condition: here it is $\partial_x q$. The unit of $\partial_x q$ is $\mathrm{W/m^3}$, although it is not a volumetric heat source. The unit can be rewritten as $\mathrm{W/m^3 = J/(s\ m^3) = Pa/s}$. This is, interestingly, a pressure rate whose quantity appears in models for low-temperature phenomena, and therefore this type of boundary condition could be viable in such cases.

The T-representation of the Fourier heat equation (4.1) is commonly used due to practical reasons, such as that T is a measurable quantity. Moreover, as Fourier's law (2.3) is an equality, it becomes straightforward how to use the temperature in the definition of a boundary condition. Hence, it does not matter which variable we choose to use as a boundary condition, either T or q is adequate, even for temperature-dependent thermal conductivity. Unfortunately, following that thread is misleading for non-Fourier equations.

4.1. **Linear case.**

For constant coefficients, it is straightforward to eliminate one of the field variables and obtain the representations, e.g., for the GK equation using

(2.4) and (2.9):

$$\text{T-representation:} \qquad \tau\partial_{tt}T + \partial_t T = \alpha\partial_{xx}T + \kappa^2\partial_{txx}T, \tag{4.3}$$

$$\text{q-representation:} \qquad \tau\partial_{tt}q + \partial_t q = \alpha\partial_{xx}q + \kappa^2\partial_{txx}q. \tag{4.4}$$

Let us recall that the definition of the second-type boundary condition depends on the field variable. Therefore, having the form of (4.3), it is not possible to explicitly prescribe the heat flux q on the boundary, only $\partial_x T$. However, these quantities are not proportional with each other; the partial differential equation (2.9) restricts their relationship. Consequently, one cannot solve the GK equation in the form of (4.3) for situations with prescribed q on the boundaries [28, 43]. This is the point where the q-representation becomes advantageous and can be used to determine the time (and space) evolution of q. The temperature can be recovered at the end by exploiting the energy balance (2.4). We also emphasise that both of these representations are the consequence of the system (2.4) and (2.9), which is more useful for analytical and numerical solutions [45, 43]. In the following, in Sec. 4.3, the discrete treatment of heat flux boundary conditions is presented. Overall, Eq. (4.3) is suggested only for T-type initial and boundary conditions. For any other situation, the most advantageous form is the system of equations (2.4) and (2.9), without eliminating any variables. For analytical solutions, however, Eq. (4.4) could be more suitable. Keeping in mind these properties, the usual boundary conditions remain valid, and the most suitable form can be chosen for the particular problem.

The treatment of initial conditions is also not evident. In many situations, the steady initial state is disturbed through the boundary (e.g., by a heat pulse), but non-equilibrium initial conditions are rarely investigated in regard to non-Fourier equations. As we mentioned, such a problem is straightforward in the Fourier model as it requires only the initial temperature distribution. However, for a non-Fourier equation, the initial time derivative is also necessary.

As the energy balance (2.4) suggests, the initial time derivative of temperature is determined by the initial heat flux field. It turned out recently [42] that the heat flux for the initial state can be determined using Fourier's law if the initial non-equilibrium state is close to equilibrium for both the MCV and GK equations. Moreover, as the energy balance is exploited in that step, a heat source could also contribute to the initial state. However, whether the initial state is close or far from equilibrium is still an open question. For such a non-equilibrium initial state, the initial time derivative can be found by exploiting the energy balance (2.4). The difficulty originates in the mathematical treatment of the initial conditions, where the differentiability stands as a crucial question. For further details, see [42].

4.2. **Nonlinear case.** With temperature-dependent parameters, such as (3.3) for the MCV equation, it is no longer possible to eliminate any of the variables, therefore pure T and q representations no longer exist. That difficulty does not affect the required number of boundary conditions, and the numerical treatment of the system of partial differential equations is still feasible with a staggered grid for the spatial domain [22]. The role of non-equilibrium initial conditions is still unclear as it has not yet been investigated with nonlinear non-Fourier models.

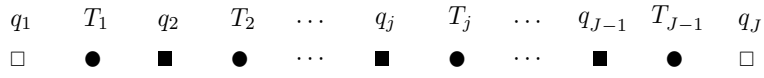

Figure 1. The staggered grid for the numerical solutions [43].

4.3. **Time-delayed boundary.** Fourier's law can be seen as the differential analogy of the Newton law for cooling, i.e., $q = h(T - T_\infty)$, where h stands for the heat transfer coefficient. In the following, let us suppose that this relationship changes together with the constitutive equation, i.e., for the MCV equation (2.10), it has a form of $\tau \mathrm{d}_t q + q = h(T - T_\infty)$. It describes a time delay on the boundary as it is also a part of the same material for which the MCV equation is used. Here, for demonstration, we provide a particular example of a heat pulse experiment. In order to keep the temperature history and the parameters realistic for the MCV model, we chose a low-temperature experiment performed by McNelly et al. [46]. Therefore, let the parameters be $\lambda = 3000$ W/(m K), $\rho = 2800$ kg/m^3, $c = 3.5$ J/(kg K), $\tau = 6$ μs, with a heat pulse duration $t_p = 10$ μs, on a 10 mm long NaF sample.

Initially, the sample is in a steady state. A short heat pulse is applied on the front side, and the temperature is recorded in time on the rear end. The heat pulse is modelled using $q(x = 0, t \leq t_p) = q_0(1 - \cos\left(2\pi t/t_p\right))$, then $q(x, t > t_p) = 0$ W/m^2. We assume a cooling boundary on the rear side. The heat transfer coefficient is the same for both cases, $h = 10^4$ W/(m^2 K). We solve this model utilising a finite difference method [43] on a staggered grid, illustrated in Figure 1. That staggering helps us to avoid problems on the boundary by allowing us to explicitly prescribe the heat flux on the boundary points. That structure can be realised for any other system with thermodynamic compatibility, even in a three-dimensional case [44]. Figure 2 presents the rear side temperature history, comparing the two cooling boundary conditions. Visibly, the vicinity of the wave shows significant differences; the temperature rises higher, which could be an essential part in the reproduction of such low-temperature heat pulse experiments [46, 47]. When the strong wave signal disappears, the temperature histories run together for both boundary conditions.

5. Discussion

In the present paper, we discussed the thermodynamic origin of two non-Fourier equations, called Maxwell-Cattaneo-Vernotte and Guyer-Krumhansl equations. We took a closer look at the new material coefficients (τ and κ^2). Furthermore, it turned out that the thermal conductivity connects these parameters. That is, in the case of temperature-dependent thermal conductivity, the other coefficients inherit that dependence. Moreover, the mechanical field must be included as well through thermal expansion effects.

We investigated the analogies between the Fourier and non-Fourier equations related to the boundary conditions, showing that the usual approach does not work for advanced heat equations. This also holds for the initial conditions. Moreover, we performed a numerical analysis of how a possible time delay would modify the

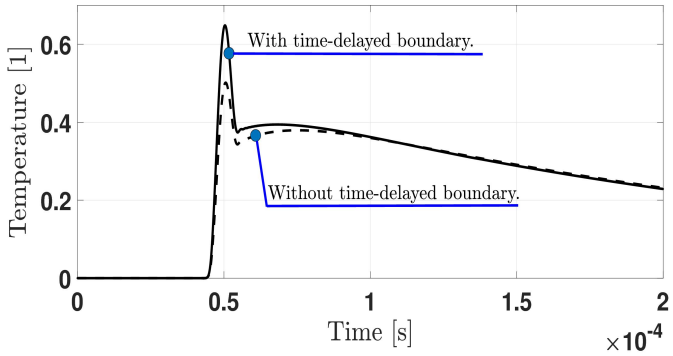

Figure 2. Rear side temperature history for both types of boundary conditions according to the MCV equation

temperature history. The time delay of the heat transfer causes significant differences in the vicinity of the wavefront. However, that difference disappears soon, and after a certain time instant, both boundaries predict the exact temperature history.

Acknowledgement. The research reported in this paper and carried out at BME has been supported by the grants National Research, Development and Innovation Office-NKFIH FK 134277 and the New National Excellence Program of the Ministry for Innovation and Technology project ÚNKP-21-5-BME-368. This paper was supported by the János Bolyai Research Scholarship of the Hungarian Academy of Sciences.

References

1. Majumdar, A.: Microscale heat conduction in dielectric thin films. *Journal of Heat Transfer*, **115**(1), (1993), 7–16. DOI: 10.1115/1.2910673
2. Brorson, S. D., Fujimoto, J. G., and Ippen, E. P.: Femtosecond electronic heat-transport dynamics in thin gold films. *Physical Review Letters*, **59**(17), (1987), 1962. DOI: 10.1103/PhysRevLett.59.1962
3. Sobolev, S. L.: Heat conduction equation for systems with an inhomogeneous internal structure. *Journal of Engineering Physics and Thermophysics*, **66**(4), (1994), 436–440. DOI: 10.1007/BF00853470
4. Roetzel, W., Putra, N., and Das, S. K.: Experiment and analysis for non-Fourier conduction in materials with non-homogeneous inner structure. *International Journal of Thermal Sciences*, **42**(6), (2003), 541–552. DOI: 10.1016/S1290-0729(03)00020-6
5. Józsa, V. and Kovács, R.: *Solving Problems in Thermal Engineering: A Toolbox for Engineers*. Springer, 2020. ISBN: 978-3-030-33475
6. Joseph, D. D. and Preziosi, L.: Heat waves. *Reviews of Modern Physics*, **61**(1), (1989), 41. DOI: 10.1103/RevModPhys.61.41
7. Straughan, B.: *Heat Waves*. Springer Science & Business Media, 2011. DOI: 10.1007/978-1-4614-0493-4
8. de Groot, S. R. and Mazur, P.: *Non-Equilibrium Thermodynamics*. Dover Publications, 1963. ISBN: 0-486-64741-2

9. Jou, D., Casas-Vazquez, J., and Lebon, G.: Extended irreversible thermodynamics revisited (1988-98). *Reports on Progress in Physics*, **62**(7), (1999), 1035. DOI: 10.1088/0034-4885/62/7/201
10. Lebon, G.: Heat conduction at micro and nanoscales: a review through the prism of extended irreversible thermodynamics. *Journal of Non-Equilibrium Thermodynamics*, **39**(1), (2014), 35–59. DOI: 10.1515/jnetdy-2013-0029
11. Müller, I. and Ruggeri, T.: *Rational Extended Thermodynamics*. Springer, 1998. DOI: 10.1007/978-1-4612-2210-1
12. Grmela, M.: Why GENERIC? *Journal of Non-Newtonian Fluid Mechanics*, **165**(17-18), (2010), 980–986. DOI: 10.1016/j.jnnfm.2010.01.018
13. Öttinger, H. C.: GENERIC integrators: structure preserving time integration for thermodynamic systems. *Journal of Non-Equilibrium Thermodynamics*, **43**(2), (2018), 89–100. DOI: 10.1515/jnet-2017-0034
14. Gyarmati, I.: *Non-equilibrium Thermodynamics.* Springer, 1970. ISBN: 978-3-642-51067-0
15. Maugin, G. A. and Muschik, W.: Thermodynamics with internal variables. Part I. General concepts. *Journal of Non-Equilibrium Thermodynamics*, **19**(3), (1994), 217–249. DOI: 10.1515/jnet.1994.19.3.217
16. Maugin, G. A. and Muschik, W.: Thermodynamics with internal variables. Part II. Applications. *Journal of Non-Equilibrium Thermodynamics*, **19**(3), (1994), 250–289. DOI: 10.1515/jnet.1994.19.3.250
17. Verhás, J.: *Thermodynamics and Rheology.* Akadémiai Kiadó-Kluwer Academic Publisher, 1997. ISBN: 0-7923-4251-8
18. Berezovski, A. and Ván, P.: *Internal Variables in Thermoelasticity.* Springer, 2017. DOI: 10.1007/978-3-319-56934-5
19. Cattaneo, C.: Sur une forme de lequation de la chaleur eliminant le paradoxe dune propagation instantanee. *Comptes Rendus Hebdomadaires Des Seances De L'Academie Des Sciences*, **247**(4), (1958), 431–433.
20. Vernotte, P.: Les paradoxes de la théorie continue de léquation de la chaleur. *Comptes Rendus Hebdomadaires Des Seances De L'Academie Des Sciences*, **246**(22), (1958), 3154–3155.
21. Guyer, R. A. and Krumhansl, J. A.: Solution of the linearized phonon Boltzmann equation. *Physical Review*, **148**(2), (1966), 766–778. DOI: 10.1103/PhysRev.148.766
22. Fehér, A. and Kovács, R.: On the evaluation of non-Fourier effects in heat pulse experiments. *International Journal of Engineering Science*, **169**, (2021), 103577. DOI: 10.1016/j.ijengsci.2021.103577
23. Ván, P.: Weakly nonlocal irreversible thermodynamics – the Guyer-Krumhansl and the Cahn-Hilliard equations. *Physics Letters A*, **290**(1-2), (2001), 88–92. DOI: 10.1016/S0375-9601(01)00657-0
24. Ván, P. and Fülöp, T.: Universality in heat conduction theory – weakly nonlocal thermodynamics. *Annalen der Physik (Berlin)*, **524**(8), (2012), 470–478. DOI: 10.1002/andp.201200042
25. Matolcsi, T.: *Ordinary Thermodynamics.* Akadémiai Kiadó, 2004. ISBN 978-615-80157-2-1

26. Onsager, L.: Reciprocal relations in irreversible processes. I. *Physical Review*, **37**(4), (1931), 405. DOI: 10.1103/PhysRev.37.405

27. Onsager, L.: Reciprocal relations in irreversible processes. II. *Physical Review*, **38**(12), (1931), 2265. DOI: 10.1103/PhysRev.38.2265

28. Szücs, M., Kovács, R., and Simić, S.: Open mathematical aspects of continuum thermodynamics: Hyperbolicity, boundaries and nonlinearities. *Symmetry*, **12**, (2020), 1469. DOI: 10.3390/sym12091469

29. Kovács, R., Madjarević, D., Simić, S., and Ván, P.: Non-equilibrium theories of rarefied gases: internal variables and extended thermodynamics. *Continuum Mechanics and Thermodynamics*, **33**, (2021), 307–325 DOI: 10.1007/s00161-020-00888-y

30. Nyíri, B.: On the entropy current. *Journal of Non-Equilibrium Thermodynamics*, **16**(2), (1991), 179–186. DOI: 10.1515/jnet.1991.16.2.179

31. Szücs, M., Pavelka, M., Kovács, R., Fülöp, T., Ván, P., and Grmela, M.: A case study of non-Fourier heat conduction using Internal Variables and GENERIC. *Journal of Non-Equilibrium Thermodynamics*. DOI: 10.1515/jnet-2021-0022

32. Kovács, R. and Rogolino, P.: Numerical treatment of nonlinear Fourier and Maxwell-Cattaneo-Vernotte heat transport equations. *International Journal of Heat and Mass Transfer*, **150**, (2020), 119281. DOI: 10.1016/j.ijheatmasstransfer.2019.119281

33. Balassa, G., Rogolino, P., Rieth, A., and Kovács, R.: New perspectives for modelling ballistic-diffusive heat conduction. *Continuum Mechanics and Thermodynamics*, **33**, (2021), 2007–2026. DOI: 10.1007/s00161-021-00982-9

34. Fehér, A., Lukács, N., Somlai, L., Fodor, T., Szücs, M., Fülöp, T., Ván, P., and Kovács, R.: Size effects and beyond-fourier heat conduction in room-temperature experiments. *Journal of Non-Equilibrium Thermodynamics*, **46**, (2021), 403–411. DOI: 10.1515/jnet-2021-0033

35. Tzou, D. Y.: *Macro- to Micro-scale Heat Transfer: The Lagging Behavior*. CRC Press, 1996. ISBN: 978-1-118-81822-0

36. Fabrizio, M. and Franchi, F.: Delayed thermal models: stability and thermodynamics. *Journal of Thermal Stresses*, **37**(2), (2014), 160–173. DOI: 10.1080/01495739.2013.839619

37. Fabrizio, M. and Lazzari, B.: Stability and second law of thermodynamics in dual-phase-lag heat conduction. *International Journal of Heat and Mass Transfer*, **74**, (2014), 484–489. DOI: 10.1016/j.ijheatmasstransfer.2014.02.027

38. Kovács, R. and Ván, P.: Thermodynamical consistency of the Dual Phase Lag heat conduction equation. *Continuum Mechanics and Thermodynamics*, pp. 1–8. DOI: 10.1007/s00161-017-0610-x

39. Quintanilla, R. and Racke, R.: Qualitative aspects in dual-phase-lag heat conduction. *Proceedings of the Royal Society of London A: Mathematical, Physical and Engineering Sciences*, **463**(2079), (2007), 659–674. DOI: 10.1098/rspa.2006.1784

40. Rukolaine, S. A.: Unphysical effects of the dual-phase-lag model of heat conduction: higher-order approximations. *International Journal of Thermal Sciences*, **113**, (2017), 83–88. DOI: 10.1016/j.ijthermalsci.2016.11.016

41. Rukolaine, S. A.: Unphysical effects of the dual-phase-lag model of heat conduction. *International Journal of Heat and Mass Transfer*, **78**, (2014), 58–63. DOI: 10.1016/j.ijheatmasstransfer.2014.06.066

42. Kovács, R.: Analytical treatment of nonhomogeneous initial states for non-Fourier heat equations. *International Communications in Heat and Mass Transfer*, **134**, (2022), 106021. DOI: 10.1016/j.icheatmasstransfer.2022.106021

43. Rieth, A., Kovács, R., and Fülöp, T.: Implicit numerical schemes for generalized heat conduction equations. *International Journal of Heat and Mass Transfer*, **126**, (2018), 1177 – 1182. DOI: 10.1016/j.ijheatmasstransfer.2018.06.067

44. Pozsar, A., Szücs, M., Kovács, R., and Fülöp, T.: Four spacetime dimensional simulation of rheological waves in solids and the merits of thermodynamics. *Entropy*, **22**, (2020), 1376 DOI: 10.3390/e22121376

45. Kovács, R.: Analytic solution of Guyer-Krumhansl equation for laser flash experiments. *International Journal of Heat and Mass Transfer*, **127**, (2018), 631–636. DOI: 10.1016/j.ijheatmasstransfer.2018.06.082

46. McNelly, T. F., Rogers, S. J., Channin, D. J., Rollefson, R. J., Goubau, W. M., Schmidt, G. E., Krumhansl, J. A., and Pohl, R. O.: Heat pulses in NaF: Onset of second sound. *Physical Review Letters*, **24**(3), (1970), 100–102. DOI: 10.1103/PhysRevLett.24.100

47. Kovács, R. and Ván, P.: Second sound and ballistic heat conduction: NaF experiments revisited. *International Journal of Heat and Mass Transfer*, **117**, (2018), 682–690. DOI: 10.1016/j.ijheatmasstransfer.2017.10.041

Journal of Computational and Applied Mechanics, Vol. 17, No. 1, (2022), pp. 15–43
DOI: 10.32973/jcam.2022.002

MODELING RAPID SOLIDIFICATION AND MELTING PROCESSES FOR MULTIPHASE FLOWS IN A WELDING TECHNOLOGY APPLICATION

Xin Xiong
Centre for Computational Engineering Sciences, Cranfield University,
Cranfield, Bedfordshire, MK43 0AL, United Kingdom
xin.xiong@cranfield.ac.uk

László Könözsy
Centre for Computational Engineering Sciences, Cranfield University,
Cranfield, Bedfordshire, MK43 0AL, United Kingdom
laszlo.konozsy@cranfield.ac.uk

[Received: March 20, 2022; Accepted: May 9, 2022]

Abstract. This article presents unsteady simulations of laser welding based on a rapid solidification/melting model using the ANSYS-FLUENT software package with the implementation of a UDF (User Defined Function) C code. It assumes a flat interface of liquid and gas without plasma plume, evaporation and reflection and absorption effect. In the simulations, a variety of parameters are considered with different welding speeds and laser powers. The results show that with the increase of laser power, liquid fraction and velocity, penetration depth and bead width all increase. In contrary, with the increase of welding speed, the temperature, liquid fraction, penetration depth, and bead width all decrease, while the velocity magnitude is an exception. It has also been found that the increase of welding speed distorts the pool shape and forms a long tail in temperature, liquid fraction and velocity contour. The buoyancy force did not have a significant impact on the results, while the convective term makes the velocity, temperature and liquid fraction smaller. Furthermore, the negative Marangoni shear stress makes the velocity along the height and the width direction smaller in the middle of the workpiece and larger on the edges. The simulation results show a similar tendency to that obtained by other authors. The reason for the possible differences is due to the unsteadiness of the fluid flow field and the slightly different boundary conditions imposed in the model presented here. The novelties of this work are unsteady simulations, new boundary conditions and parametric studies relevant to industrial applications.

Mathematical Subject Classification: 76G25, 76M12, 76F60, 76F55
Keywords: Rapid Solidification/Melting, Laser Welding, Laser Power, Welding Speed, Computational Fluid Dynamics (CFD), Engineering

1. Introduction

Laser welding has many advantageous features over traditional welding techniques such as spot resistance welding. Due to the fact that the laser power and speed can be controlled precisely, laser welding can be accurate and flexible. According to Steen [1], laser welding can be utilized in many regimes such as electronics, medical devices,

automobiles, dies, and tools. It overcomes certain problems that traditional welding has with its high energy intensity. The process of laser welding can be described as follows: a) a high intensity laser beam is irradiated on the workpiece, and once the laser beam reaches the workpiece and its temperature exceeds the melting point, it begins to melt; b) after melting, a molten pool is formed with the further irradiation of the laser beam, and the liquid in the molten pool starts to evaporate, which will further form the keyhole; c) during the evaporation process, recoil pressure is created, which further drives the liquid flow outward from the molten pool; d) once the keyhole is formed, it will generate a plasma plume, which will scatter and absorb part of the laser energy, thus reducing the absorption of the objective surface.

To accurately examine the dynamics of the keyhole and the molten pool, different experimental methods have been devised such as cameras, photo diodes, spectrometer, acoustic sensor, pyrometer, and plasma charge sensor according to Shin et al. [2]. Eriksson et al. [3] utilized high speed photography to successfully visualize the dynamics of the molten pool and the keyhole. Normann et al. [4] successfully combined theoretical analysis and photo diodes to monitor the defects of laser welding. Zhang et al. [5] also examined the defect of workpieces using a spectrometer. Although different experiment measurement methods exist to investigate the dynamics of keyholes and molten pooleach has several drawbacks. Another option is Computational Fluid Dynamics (CFD), an advanced computational approach that is widely used in both academic research and industrial areas.

In the case of this specific problem, researchers conducted CFD simulations. First of all, researchers developed simplified theoretical models. For example, Swift-Hook and Gick [6] developed a theoretical analysis based on the solution of the heat diffusion equation. Lankalapalli et al. [7] developed a two-dimensional model with the assumption of a conical keyhole. Dowden et al. [8] analyzed the effect of plasma, combining the plasma model with a simple line heat source model. Secondly, researchers studied this problem using the Finite Element Method (FEM) without consideration of the fluid flow field. For example, Carmignani et al. [9] predicted residual stress and strains using FEM. In the work of Mares et al. [9], an elasto-viscoplastic constitutive equation was added to model the plastic material. Another model is the enthalpy-porosity model to consider the phase change of the workpiece between the solid and the liquid phases. Ye and Chen [10] investigated the three-dimensional effect of the surface tension and the density together assumed to be linear functions of the temperature.

Other models based on free surface tracking algorithms are the level-set method and the VOF (Volume-of-Fluid) method. The level-set method is a self-consistent free surface tracking approach, according to Mohanty and Mazumder [11]. It introduces an equation of motion of interface as a scalar conservation law with viscosity and boundary conditions for the laser welding model [11]. Geiger et al. [12] modeled the joining of zinc coated sheets. They used an open-source software package called OpenFOAM with the VOF model. They also implemented the Gaussian distribution as a surface heat source. They considered the Fresnel absorption, evaporation pressure and surface tension in their computational model. Because of the evaporation effect,

it was found that there are low frequency oscillations in the melt pool and high frequency oscillations on the keyhole.

In this paper, a novel unsteady CFD simulation approach for the laser welding model is developed and presented. The effects of surface tension, unsteady fluid flow field, non-isothermal effect, natural convection, heat conduction and melting effects have been considered to provide numerical results that are compared with the work of Abderrazak et al. [13]. The implementation of the additional source terms of the rapid solidification and melting model is carried out in the ANSYS-FLUENT software package within the framework of the solidification and melting model using User-Defined Functions (UDFs), which are computer codes written in C programming language. The structure of the present work can be described as follows: Section 2 describes the governing equations; Section 3 focuses on the mesh and the geometrical model, including mesh sensitivity and time-step studies; Section 4 is the discussion of the computational resultsm which includes the parametric studies; and Section 5 addresses conclusions and recommendations for future work.

2. Governing Equations and Methodology

The governing equation of the rapid solidification model presented here is based on the enthalpy-porosity model. This model combines the solid and liquid equations as a single equation, which was also considered by Abderrazak et al. [13]. The continuity equation of three-dimensional fluid flows can be expressed by

$$\frac{\partial \rho}{\partial t} + \frac{\partial(\rho u)}{\partial x} + \frac{\partial(\rho v)}{\partial y} + \frac{\partial(\rho w)}{\partial z} = 0, \tag{2.1}$$

where ρ is the density of the material, t is the time for unsteady simulations, x, y, z are the Cartesian coordinates, u, v, w are the velocity components of the fluid flow in x, y and z directions, respectively. The scalar momentum equations are

$$\frac{\partial \rho u}{\partial t} + \nabla \cdot (\rho u \vec{u}) = -\frac{\partial p}{\partial x} + \nabla \cdot (\mu \nabla u) - \frac{\mu}{K}(u - u_x), \tag{2.2}$$

$$\frac{\partial \rho v}{\partial t} + \nabla \cdot (\rho v \vec{u}) = -\frac{\partial p}{\partial y} + \nabla \cdot (\mu \nabla v) - \frac{\mu}{K} v, \tag{2.3}$$

$$\frac{\partial \rho w}{\partial t} + \nabla \cdot (\rho w \vec{u}) = -\frac{\partial p}{\partial z} + \nabla \cdot (\mu \nabla w) - \frac{\mu}{K} w + \rho g \beta (T - T_{\text{ref}}), \tag{2.4}$$

where p is the pressure, $\vec{u}$ is the velocity vector, K is the permeability coefficient, μ is the dynamic viscosity, u_x is the welding speed in x direction, β is the thermal expansion coefficient, g is the magnitude of the gravitational acceleration, T is the temperature, and T_{ref} is the reference temperature. The energy equation is modeled as

$$\rho C_p \left(\frac{\partial T}{\partial t} + \nabla \cdot (T \vec{u}_1) \right) = \nabla \cdot (k \nabla T) + S(x, y, z) - \nabla \cdot ((\rho \vec{u}) \Delta H), \tag{2.5}$$

where $\vec{u}_1$ is the fluid velocity, which are $u - v_w$, v, w in x, y, z directions, v_w is the welding speed, $\vec{u}$ is the velocity, which are u, v, w in x, y, z directions, C_p is the

specific heat, k is the heat conduction coefficient, S is the additional heat source, ΔH is the latent heat. A Gaussian volume heat source was implemented in this model as

$$Q(x,y,z) = \frac{3P}{\pi abd} \exp\left(-\frac{3x^2}{a^2}\right) \exp\left(-\frac{3y^2}{b^2}\right) \exp\left(-\frac{3z^2}{d^2}\right), \tag{2.6}$$

where $Q(x,y,z)$ is the heat source, P is the power of laser beam, a, b, d are the length, width and depth of the laser beam, respectively. The boundary condition of the bottom surface is a convective boundary condition

$$q_{\mathrm{c}} = h_{\mathrm{ext}} \left(T_{\mathrm{ext}} - \mathrm{T_w}\right), \tag{2.7}$$

where q_c is the convective heat energy, h_{ext} is the convective heat transfer coefficient, T_{ext} is the exterior temperature, and T_w is the temperature of the bottom wall where the convective effect was set to be considered. The surface convection is only allowed between the bottom wall and the environment. The boundary condition of top surface is a constant shear stress as described below:

$$\mu \frac{\partial u}{\partial z} = C, \tag{2.8}$$

where C is a constant and the left term represents shear stress. This is different from the work of Abderrazak et al. [13], because in their work [13], the shear stress is used to model the negative Marangoni effect, which is related to the temperature gradient. However, the temperature gradient in this model is very small. Thus, the influence of the temperature gradient can be ignored, and thus constant shear stress is assumed here to simplify the model. The other boundary condition is set to a constant temperature of 300 K, except for the bottom wall.

In this model, thermal expansion is allowed in the normal direction, which can be seen from the z-momentum equation with the expansion term. The top wall is modeled as a flat surface model in this work. For the sake of simplicity, the solid top wall has been considered to be a rigid wall.

The material properties of the model are considered to be constant, except for the density, which is predicted based on the Boussinesq assumption. The thermal conductivity k has been considered as constant within the same phase as a modeling simplification. This simplification follows the model description of Abderrazak et al. [13], where the thermal conductivity was considered to be constant for each phase. Large temperature differences can be observed in the middle of the domain. The dynamic viscosity μ is constant for the liquid phase. Furthermore, the permeability parameter K is used to model the phase change, which is derived from the Kozeny–Carman equation [13] to make a smooth transition between two phases. Therefore, a unified equation is solved for both phases. When a solid phase is considered during the process, K is a very small value and the fluid flow velocity is approximately zero in the y and z directions, while K is equal to the welding speed in direction x. When melting occurs during the welding process, the permeability parameter K becomes a very large value.

3. Computational Domain, Mesh Sensitivity and Time-Step Study

As can be seen from Figure 1, the workpiece moved with the welding speed and a laser beam is introduced from above. The physical domain of this engineering problem is considered to be rectangular. The computational mesh is a structured mesh due to the simplicity of the rectangular geometry. Three mesh densities were generated to study the mesh sensitivity for the numerical solution (Table 1).

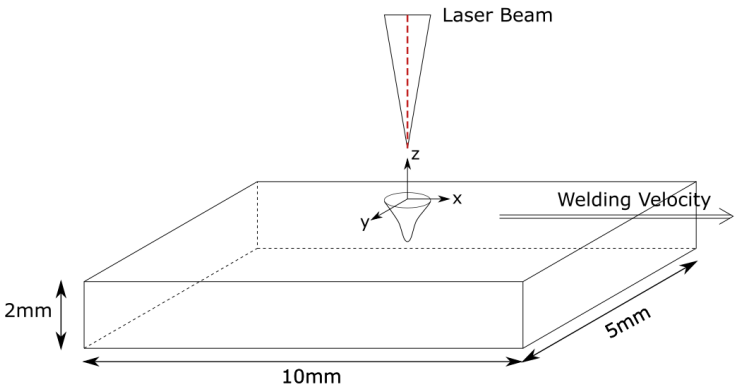

Figure 1. Geometry of the computational domain [13]

Table 1. Three mesh densities

	x	y	z	Total cells	Total faces
Coarse	100	50	20	92,169	284,170
Medium	200	100	40	768,339	2,336,340
Fine	400	200	80	6,272,679	18,944,680

The number of nodal points in x, y and z directions can be found in Table 1. To select the most appropriate time step size, three different levels of the CFL number were studied. It turns out that CFL=5 is too large and CFL=0.1 is not necessary to obtain a reasonable computational cost. These results are summarized in Table 2.

Table 2. Different time steps with different CFL numbers at different mesh densities

CFL Number	Time step (coarse)	Time step (medium)	Time step (fine)
0.1	1e-5	5e-6	2.5e-6
1	1e-4	5e-5	2.5e-5
5	5e-4	2.5e-4	1.25e-4

Three different physical times were investigated, 40 ms, 80 ms, and 120 ms, to select the best physical time scales of the welding process which were simulated. It is important to note that the physical time here means the time scales of the simulated welding process; therefore, these values are not related to the computational time. The effect of mesh sensitivity on the numerical results has been investigated in conjunction with the temperature field, and one can see in Figure 2 that the temperature contours using different mesh densities are almost identical. Figure 3 shows the temperature profiles along the center x line using three different mesh densities, which shows again that the predicted temperature profiles are very similar to each other.

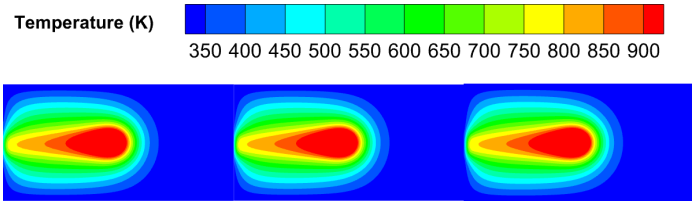

Figure 2. Temperature contour on x-y plane using three different meshes

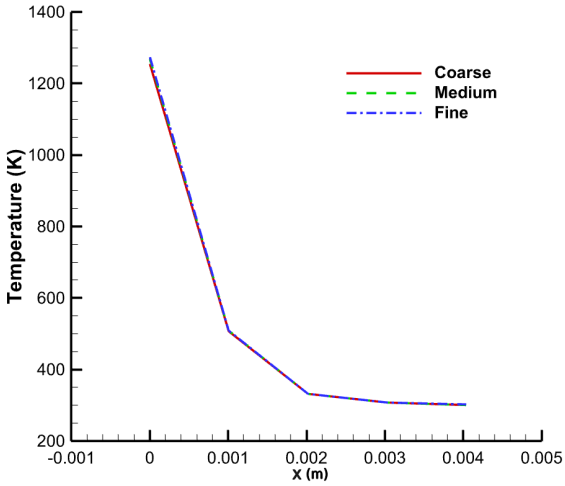

Figure 3. Temperature along the line x using three different meshes

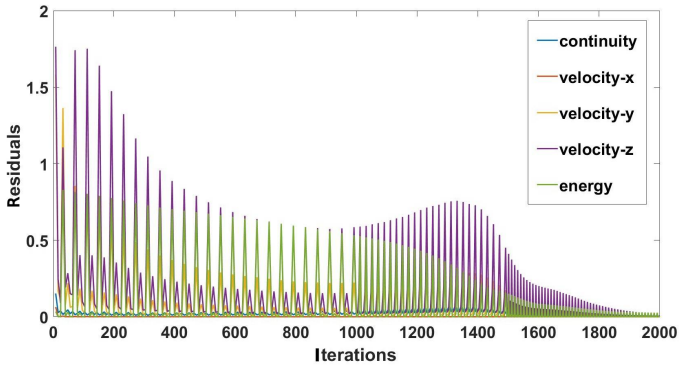

Figure 4. Residuals with CFL = 1 at 40 ms on the coarse mesh

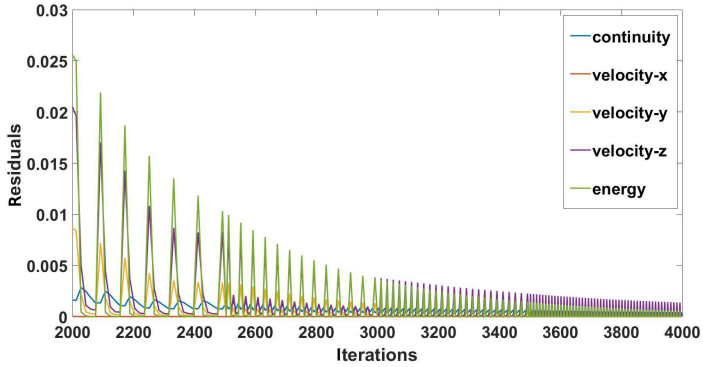

Figure 5. Residuals with CFL = 1 at 80 ms on the coarse mesh

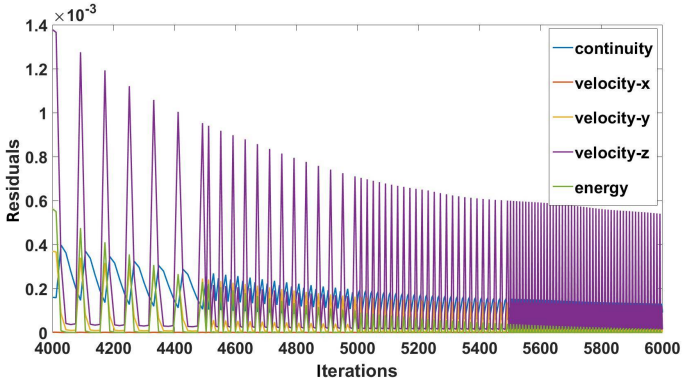

Figure 6. Residuals with CFL = 1 at 120 ms on the coarse mesh

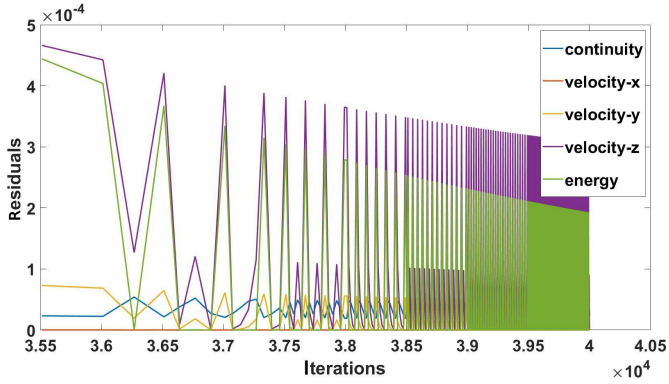

Figure 7. Residuals with CFL = 0.1 at 80 ms on the coarse mesh

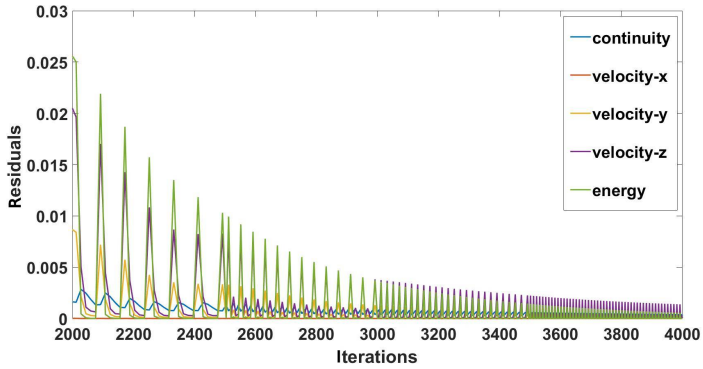

Figure 8. Residuals with CFL = 1.0 at 80 ms on the coarse mesh

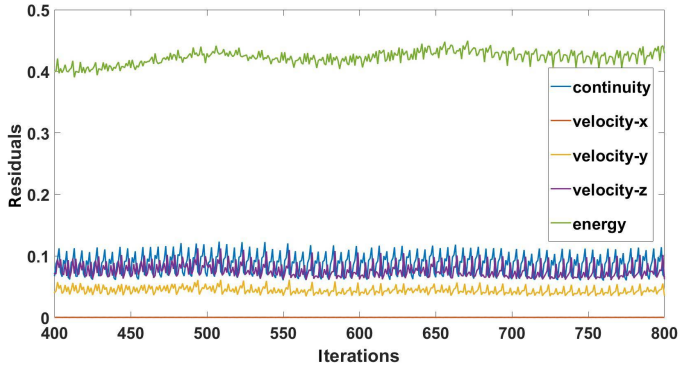

Figure 9. Residuals with CFL = 5.0 at 80 ms on the coarse mesh

To reduce computational time, based on the mesh sensitivity study on the numerical results (see Table 1 and Figures 2 and 3), the coarse mesh has been selected for the final simulations. Figures 4, 5, 6 show the residuals at three physical times. As can be seen in Figure 4, the residuals decline within 40 ms physical time, although they increase at the beginning of the simulations. Similarly to Figure 4, the residuals within 80 ms decline to 10 order of magnitude, which is much bigger than the residual obtained within 40 ms. However, after 80 ms, the residuals reach a statistical steady-state solution. Therefore, this simulation runs 80 ms physical time.

Figures 7, 8, 9 show the residuals with three different CFL numbers. One can see that the residual with CFL=1 is steady state, which is equal to 10^{-3} while it is 10^{-1} with CFL=5. Therefore, for the final simulations, CFL=1 has been selected. Thus, the time step of this model is 10^{-4} (see Table 2). To investigate different parameters, various benchmark test cases have been simulated, which are summarized in Table 3 and discussed in the next section.

Table 3. Different validation test cases

	Welding speed (m/min)	Laser power (W)	Shear stress (Pa)
case 1	1	700	6.40E-04
case 2	5	700	6.40E-04
case 3	10	700	6.40E-04
case 4	1	1000	6.40E-04
case 5	5	1000	6.40E-04
case 6	10	1000	6.40E-04
case 7	1	2000	6.40E-04
case 8	5	2000	6.40E-04
case 9	10	2000	6.40E-04
case 10	5	2000	6.40E-03
case 11	5	2000	6.40E-02
case 12	5	2000	6.40E-01
case 13 (no convective term)	5	2000	6.40E-04
case 14 (no buoyancy force)	5	2000	6.40E-04

4. Results and Discussion

In this section, simulation results for 12 cases are analyzed at different welding speeds and laser powers to investigate the impact of the welding speed and the laser power effects. In the first part, the temperature is analyzed at different laser powers and welding speeds. Figure 10 shows temperature contours on the top wall on x-y plane. From left to right, they are at welding speeds from 1 m/min to 10 m/min and from top to bottom, they are at different laser powers from 700 W to 2000 W. As can be seen from the figure, with the increase of the welding speed, the maximum temperature

decreases. This is due to the fact that with the increase of the welding speed, the interaction time between the laser beam and workpiece decreases so that the workpiece absorbs less energy. In addition, with the increase of the welding speed, the band of the temperature contour becomes longer and with an obvious "tail". This was more obvious at higher laser power.

Regarding the impact of different laser powers, it can be seen from figures that with the increase of the laser power, the maximum temperature on the center of top wall increases. This is reasonable because large laser power means more energy absorption. Moreover, Figure 11 shows the temperature contour on the x-z plane with different laser powers and welding speeds. The layout of this figure is identical with Figure 10 with different laser powers and welding speeds. However, the direction of this figure is in the width direction. As can be seen from the figure that with the increase of the laser power, the maximum temperature in the width direction increases, especially at the lowest welding speed. In term of the impact of the welding speed, the larger welding speed makes the temperature on the center much lower. The band of temperature contour with 5 m/min welding speed was longest among three contours. This is also because of the longer time of interaction between the laser beam and the workpiece.

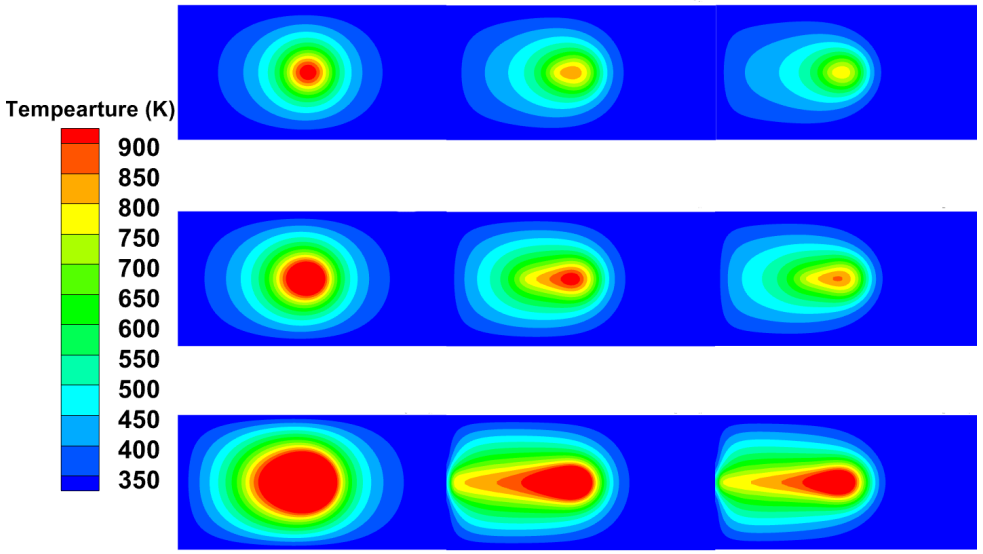

Figure 10. Temperature distribution with different parameters on x-y plane

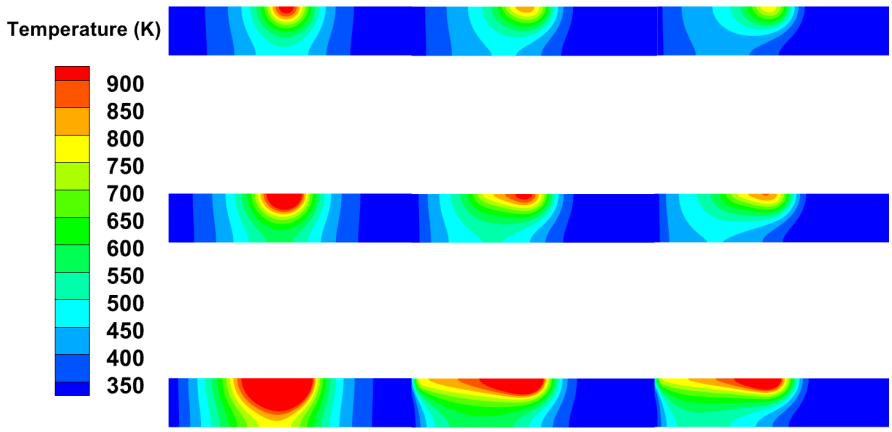

Figure 11. Temperature distribution with different parameters on x-z plane

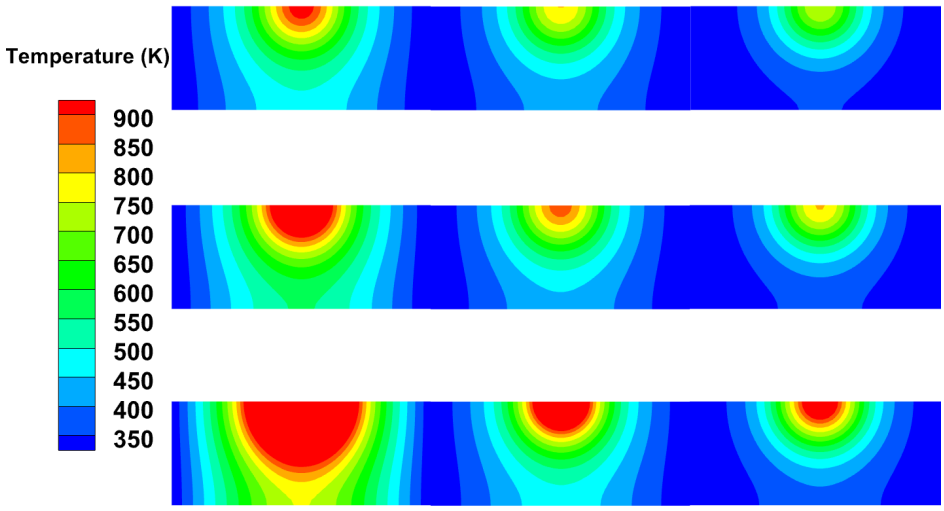

Figure 12. Temperature distribution with different parameters on y-z plane

Figure 12 demonstrates the temperature contour with different laser powers and welding speeds with the same layout as the previous figures in the y-z plane. It can also be seen from figures that with the increase of the laser power, the range of the maximum temperature increases. Another shared feature is that as the welding speed increases, the range of the maximum temperature decreases can also be seen. However, the long "tail" in figures with the increase in welding speed cannot be seen this time, which means the increase of the welding speed does not affect the symmetric feature in the depth direction. The symmetric temperature contour is because of the

Gaussian distribution heat source implemented in the energy equation. If a very low welding speed was implemented, the symmetrical feature was kept. More detailed effects of different welding speeds and laser powers can be seen in Figure 13.

In addition, Figures 10, 11, 12 show the Gaussian thermal distribution, which was implemented as a source term, with high temperature in the center, decreasing to the outside.

Figure 13(a) displays the temperature along the center x line with different welding speeds and laser powers. The same features were also seen in this figure. With respect to the welding speed, in Cases 1, 2 and 3, the maximum temperature decreases with the increase of the welding speed. In addition, there are always two parts of the curves: the first part is from bottom to the maximum temperature, and the second part is from the maximal part to the top. The same features can be seen with Cases 4, 5 and 6, although a certain amount of distortion can be observed in the first part of the curves. Similar features can be seen in Cases 7, 8 and 9. Larger distortion can be seen from the first part of the curve in Cases 8 and 9, which means that with higher laser power, the increase of the welding speed leads to larger distortion of the temperatures near the rear part of the workpiece.

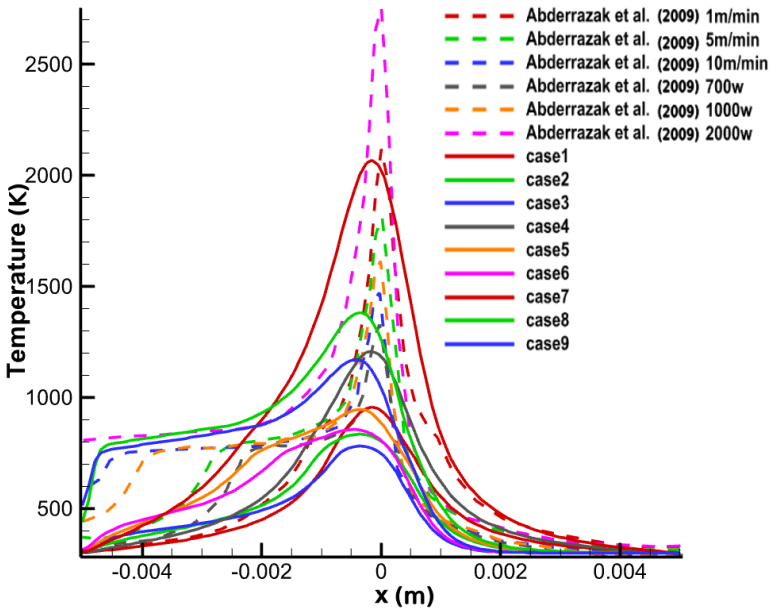

(a)

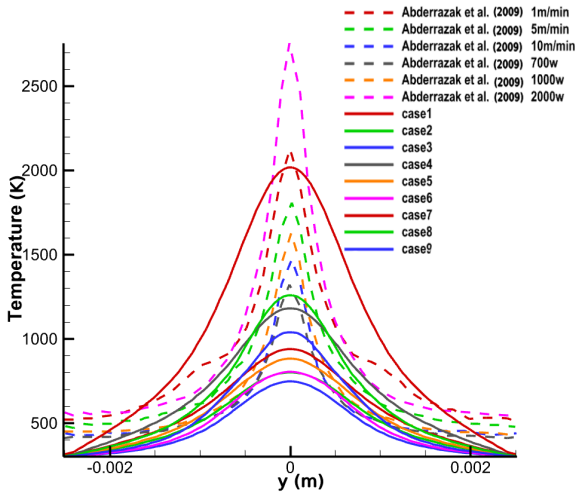

(b)

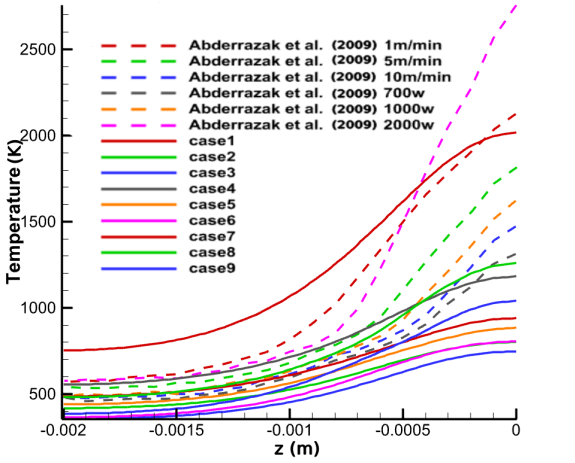

(c)

Figure 13. Temperature distribution with different laser power and welding speeds in comparison with the results of Abderrazak et al. [13] along x, y and z lines

With respect to the laser power, the maximum and overall temperature increases with the increase of the laser power in Cases 1, 4 and 7. This can also be seen from

Cases 2, 5 and 8 as well as 3, 6 and 9. In comparison with the results of Abderrazak et al. [13], it is also like a ring-bell shape curve. In addition, certain distortions are present at the beginning part of the curve, as can be seen in a few cases. Moreover, the results of the peak temperature of 2000 W of Abderrazak et al. [13] is larger than for the implemented model. The results of the shape of Abderrazak et al. [13] are a bit narrower than those of the implemented model. The combination of case settings pertaining to welding speed and laser power in the work of Abderrazak et al. [13] are not shown; therefore, the discrepancy between the reference paper and results of the implemented model is in an acceptable range. In other words, the overall shape generated by the implemented model and that of Abderrazak et al. [13] is similar.

Figure 13(b) presents the center y line with different welding speeds and laser powers. The same features with previous contours were also seen in this figure. However, distortions cannot be seen in this figure, unlike in Figure 13(a). With respect to the welding speed, Cases 1, 2 and 3 also show the trend that is similar to Figure 13(a). The same feature can be seen in Cases 4, 5 and 6 as well as 7, 8 and 9. There are also two parts of the curves, one of which is from negative y value part to the zero value and the other of which is from zero to positive y value part. In terms of the laser power, the same feature that the increase of the laser power increases the temperature can be seen in Cases 1, 4 and 7 as well as 2, 5 and 8 also 3, 6 and 9.

However, one thing worth noting is that the temperature along the center y line is almost identical with that of Cases 2 and 5. In comparison with the results obtained by Abderrazak et al. [13], it is also symmetrical. However, there are distortions in two sides of the results of Abderrazak et al. [13] with 1 m/min welding speed. Moreover, the results of the shape of Abderrazak et al. [13] are narrower than the implemented model as well. In addition, the temperature on the edge of the curve in the work of Abderrazak et al. [13] is a bit bigger than in the implemented model. However, as the combination of case settings pertaining to the welding speed and the laser power in the work of Abderrazak et al. [13] is not shown, some discrepancy between the reference paper and results with the implemented model is expected.

Figure 13(c) demonstrates the temperature along the center z line with different welding speeds and laser powers. In contrast to Figure 13(b), there is only one part of the curve, the temperature increases along the center z line, whose slope slowly increases and finally decreases to a plateau. However, with respect to the welding speed, Cases 1, 2 and 3 as well as 4, 5 and 6 also 7, 8 and 9 show the similar trend with previous contours and previous curves along x and y line. This is also true with respect to laser power. It is also interesting to note that Cases 2 and 5 have almost identical temperature, which is the same with Figure 13(b) for temperature along the center y line. In comparison with the results of Abderrazak et al. [13], the overall shape is an upward trend. However, the part behind -0.001 of the results of the slope in Abderrazak et al. [13] is higher than that of the implemented model, especially the one with 2000 W. Nevertheless, as the combination of case settings pertaining to the welding speed and the laser power in the work of Abderrazak et al. [13] is not given, a discrepancy between the reference paper and results with the implemented model is reasonable.

Figure 14 demonstrates the velocity contour on the top x-y plane with different laser powers from top to bottom and welding speeds from left to right. It can be seen from the figure that with the increase of the laser power, the range of maximum velocity becomes larger. However, it does not always decrease with the increase of the welding speed; the velocity contour with 5 m/min welding speed has the largest range of maximum velocity. Moreover, with 1000 W and 2000 W laser power, the velocity contour with 5 m/min and 10 m/min welding speed is almost identical. It is also interesting to note that with the laser power of 2000 W, the gradient of the velocity contour is much smaller. In addition, with the increase of the welding speed, the range of maximum velocity shrinks.

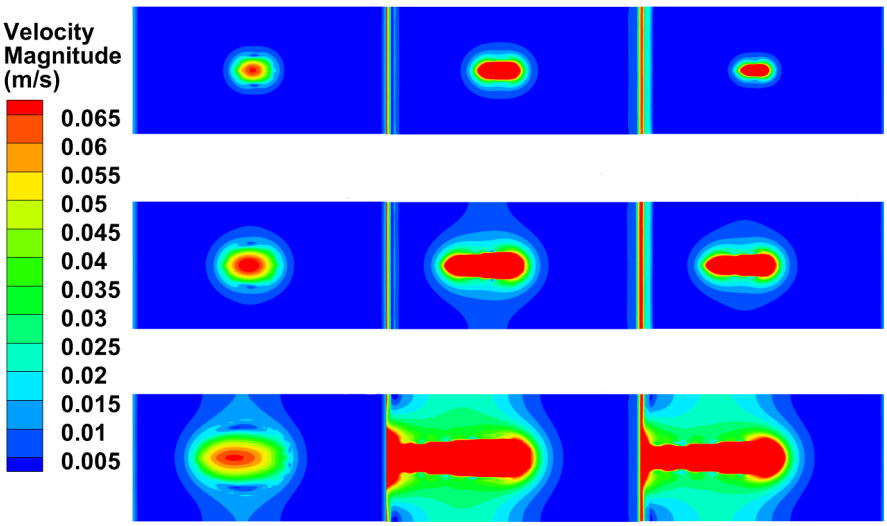

Figure 14. Velocity distribution with different parameters on x-y plane

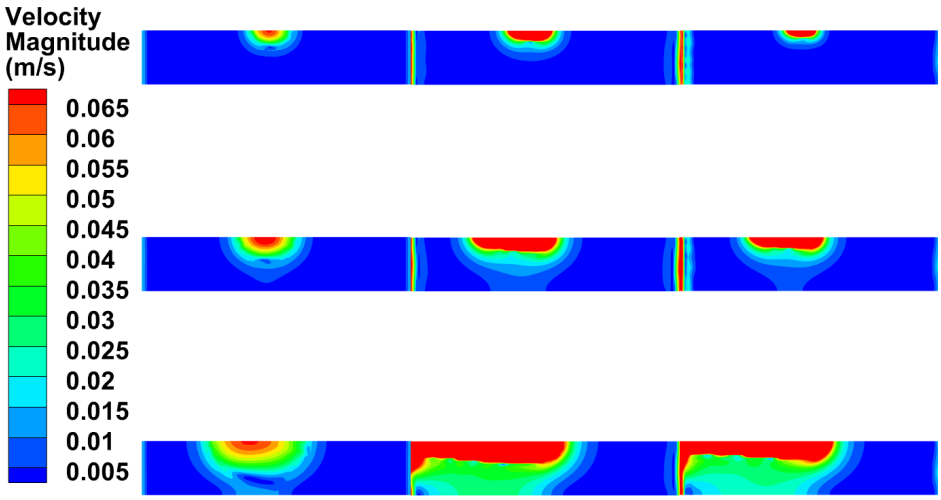

Figure 15. Velocity distribution with different parameters on x-z plane

Figure 15 shows the velocity contour on width direction on the x-z plane. It can also be seen from the figure that with the increase of the laser power from top to bottom, the range of velocity value greater than zero becomes larger. In terms of the welding speed, the velocity increase with the increase of the welding speed until 5 m/min. However, the velocity with 5 m/min and 10 m/min is almost the same. In addition, the increase of the welding speed also makes the tail of velocity contour much longer. This is similar to the temperature contour in the previous figures.

Figure 16 displays the velocity contour in the depth direction with different welding speeds and laser powers. The increase in the velocity contour with the increase of the laser power from bottom to top can also be seen from these figures. However, a special case is found with the welding speed of 1 m/min, where the velocity of maximum range decrease from with 1000 W to 2000 W. In addition, the increase of the welding speed does not make the long tail in the depth direction. In contrast to the temperature contour, there is no increasing trend with the increase of the welding speed. Moreover, the contours for 1 m/min and 5 m/min welding speed are almost identical, especially at 1000 W and 2000 W laser power.

In addition, the velocity contour also shows the Gaussian distribution feature, althoughthe Gaussian feature of velocity contour is not as strongly developed as with the temperature contour. The most symmetrical velocity contour is on the y-z plane in Figure 16. Thus, the velocity develops more strongly than the temperature contour. In comparison with the velocity results of Abederrazak et al. [13], the maximum velocity region of the center is bigger due to different boundary condition settings.

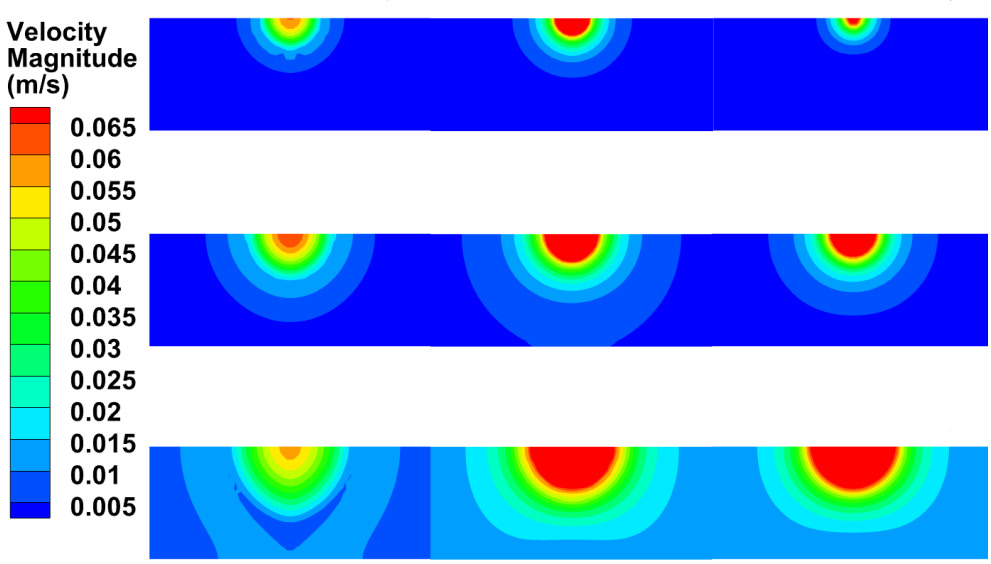

Figure 16. Velocity distribution with different parameters on y-z plane

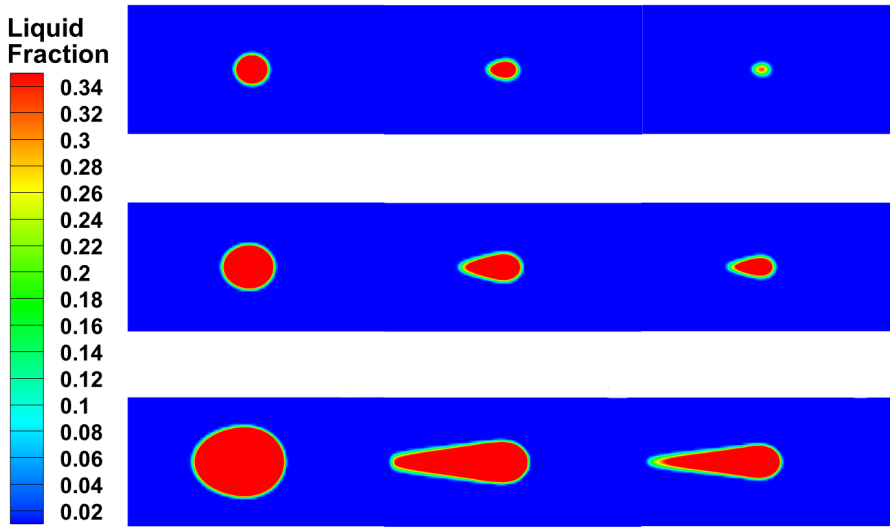

Figure 17. Liquid fraction with different parameters on x-y plane

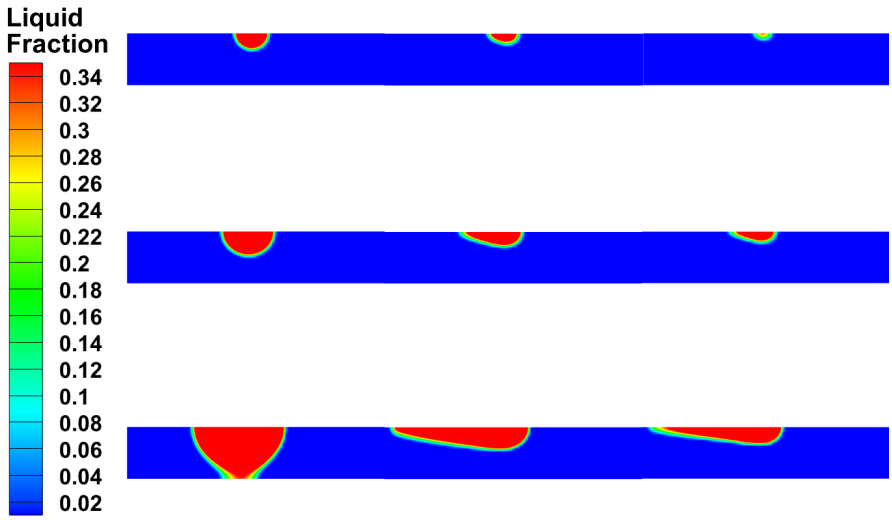

Figure 18. Liquid fraction with different parameters on x-z plane

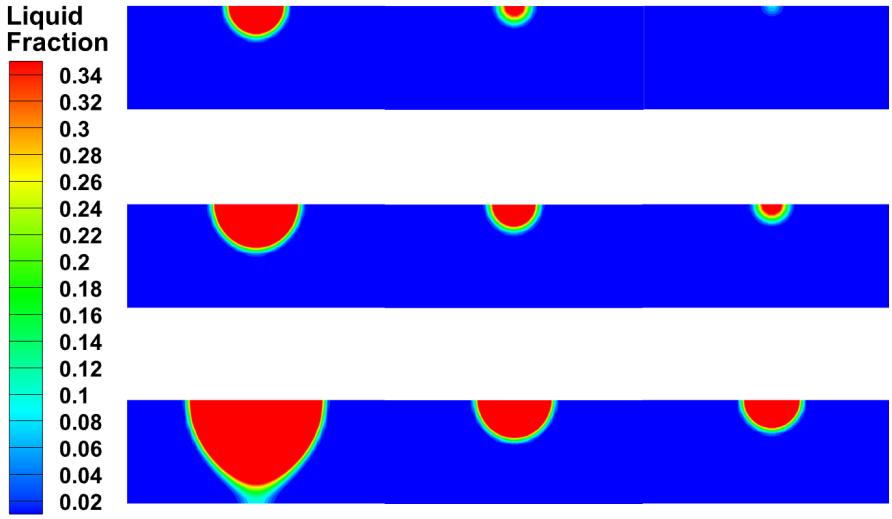

Figure 19. Liquid fraction with different parameters on y-z plane

Figure 17 demonstrates the liquid fraction on the top wall on the x-y plane with different laser powers and welding speeds. The same feature of temperature contours can be seen in this figure. In term of the laser power, the melting fraction becomes larger as the laser power increases. Regarding the welding speed, it also be seen that a longer tail is formed with the increase of the welding speed. However, with the

increase of the welding speed with the laser power of 700 W, the tail did not form, and only a small liquid fraction is present.

Figures 18 and 19 show the liquid fraction on the width and depth direction respectively. As can be seen from the figures, with the laser power increase, the liquid fraction increases both in width and depth. However, in the width direction, the long tail forms with the increase of the welding speed. In contrary, the tail does not form in the depth direction. It is also worth noting that with 700 W laser power and 10 m/min welding speed, the liquid fraction is very small both in width and depth direction.

Figure 20 shows a different pool shape with different velocity from left to right with different laser powers : 700 W, 1000 W, and 2000 W. From this figure, the long tail shape of the pool produced by the welding speed can be seen; with higher laser power, the length of tail is longer than with lower laser power. In addition, with the laser power increase, the pool shape becomes narrower at the same welding speed. It is also worth noticing that with 2000 W laser power and 1 m/min welding speed, the depth of penetration is the largest, penetrating almost the entire depth of the workpiece. Moreover, with the increase of the laser power, the center region of largest liquid increase. In terms of depth of the pool, the increase in the welding speed makes the pool shape shallower, while the laser power with small welding speed makes the pool shape deeper. Finally, the welding speed distortion impact with lower laser power is much less obvious, while the pool shape with 1000 W and 2000 W laser power becomes upward, with a longer tail, and more distorted with higher welding speed.

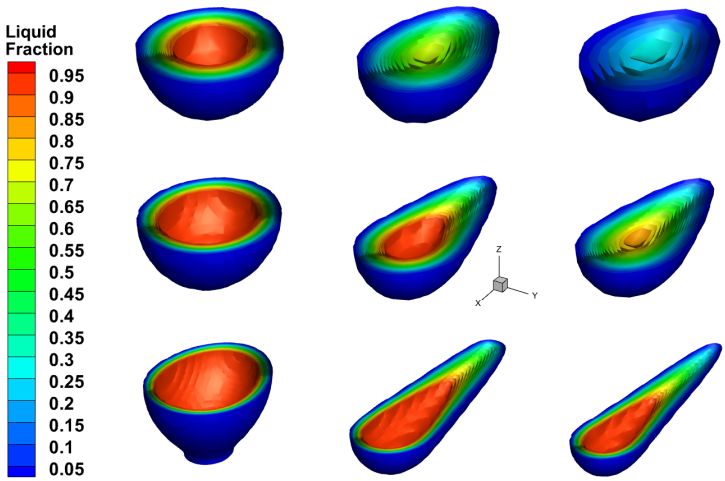

Figure 20. Pool shape with different parameters

Figure 21(a) shows the penetration depth with respect to the laser power at three different welding speeds. It can be seen from the figure that as the laser power increases, the penetration depth also increases. However, with 1 m/min welding speed, the penetration depth increases more than with 5 m/min and 10 m/min welding speeds from 1000 W to 2000 W laser power. From the range of 700 W to 1000 W, the penetration depth with three different welding speeds does not differ much. In addition, the penetration depth with 5m/min is quite similar to the results of Abderrazak et al. [13], especially with 1000 W laser power. There is little difference at 700 W and 2000 W between the two models.

Figure 21(b) demonstrates the penetration depth with respect to the welding speed at three different laser powers. As can be seen from the figure, as the welding speed increases, the penetration depth decreases, which was seen as well in the previous analysis. In addition, it is worth noting that at 2000 W laser power with the increase of the welding speed from 1 m/min to 5 m/min, the penetration depth decreases more than with lower laser power. With the increase of welding speed from 5 m/min to 10 m/min, the three penetration depths decrease to a similar degree with respect to the welding speed. This is very similar to the results of Abderrazak et al. [13] at 1000 W, especially at 1 m/min welding speed.

Figures 21(c) and 21(d) show the bead width respect to three different laser powers and three different welding speeds, respectively. It can be seen from these two figures that with the increase of the laser power the bead width of the pool increases, while it decreases with increased welding speed. Moreover, at 2000 W laser power, the bead width decreases more from the welding speed 1 m/min to 5 m/min than with lower laser power. Finally, with 1 m/min welding speed, the bead width increases more from laser power 700 W to 1000 W than with higher welding speed. This feature was also seen in the previous analysis. The reason for this may be that with lower welding speed, the interaction time between the laser beam and the workpiece is longer, so the increase in the laser powermore strongly affects the bead width. In terms of the high laser power, the increase of the welding speed leads to more energy loss with higher laser power. Regarding the comparison with the results of Abderrazak et al. [13], the bead width at 700 W is similar to the numerical values obtained by Abderrazak et al. [13]. Moreover, the bead width for 10 m/min welding speed is also similar to their results, except at 1000 W laser power.

Figures 22, 23, 24 are contours of temperature, velocity and liquid fraction at different planes with and without buoyancy force. As can be seen from the figures, the results with and without buoyancy force are almost identical. Thus at least in the implemented model settings, the buoyancy force does not have much impact on the results.

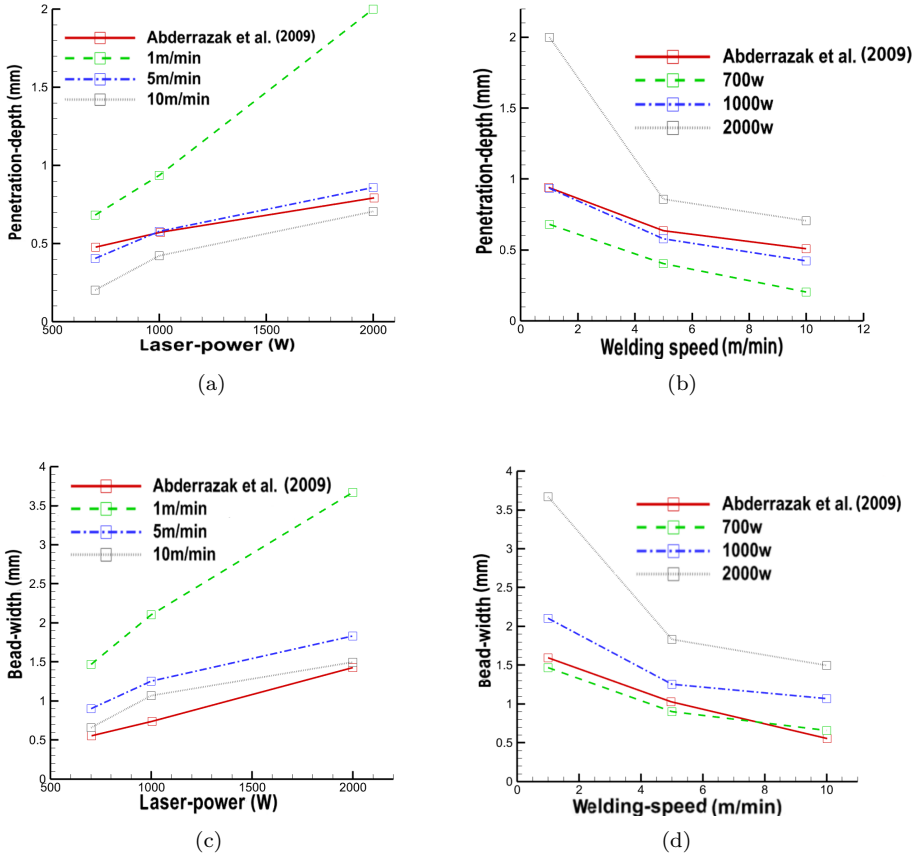

Figure 21. Penetration depth and bead width with different parameters compared to the results of Abderrazak et al. [13]

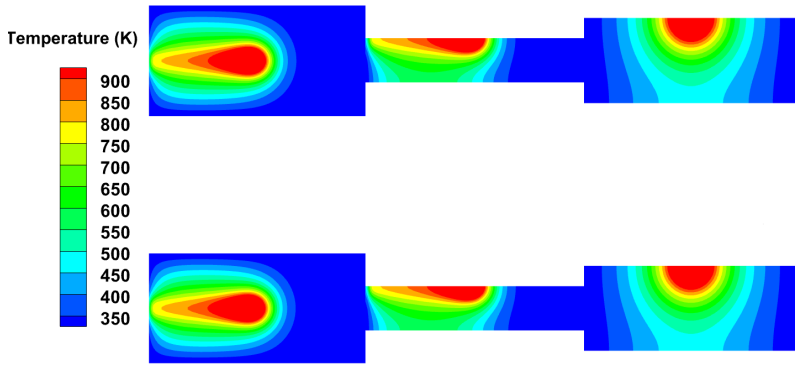

Figure 22. Temperature with and without taking the buoyancy force into account

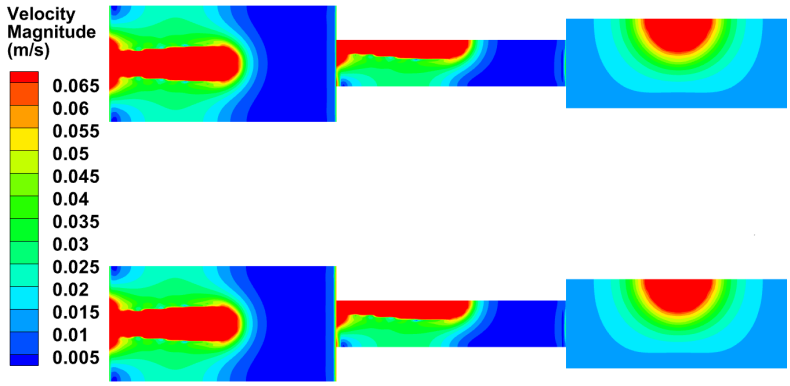

Figure 23. Velocity with and without taking the buoyancy force into account

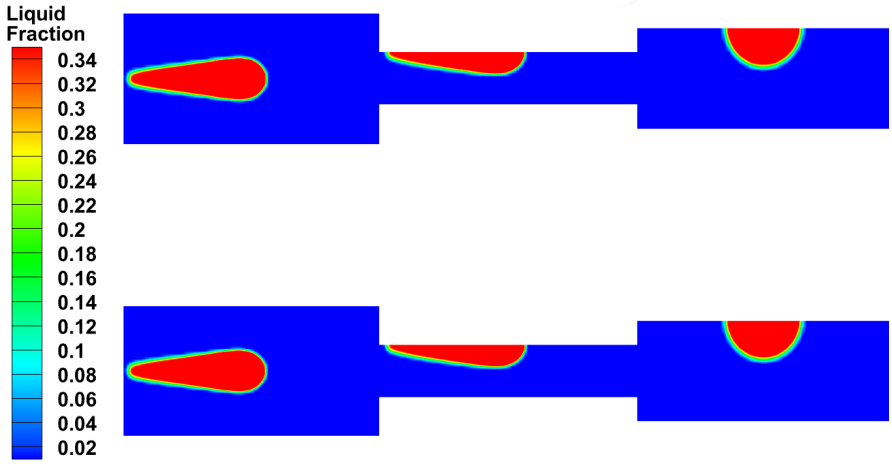

Figure 24. Liquid fraction distributions with and without taking the buoyancy force into account

In this work, we analyze the influence of buoyancy force on temperature, velocity and liquid fraction in comparison with the work of Abederrazak et al. [13] which can be considered as a novelty of this paper.

Figures 25, 26, and 27 display the temperature, velocity and liquid fraction contour with and without the convective term in the energy equation in different planes, respectively. As can be seen from Figure 25, the maximum temperature range increases without the convective term in the energy equation in the entire three planes. This is true because the convective term enhances the convection so that the pool shape becomes smaller and the maximum temperature range is much lower.

Figure 26 presents the velocity contour with and without the convective term in energy equation. As can be seen from the figure, without the convective term, the maximum velocity range becomes larger, especially in the depth and length directions. In the length direction, without the convective term, the maximum velocity range becomes wider. In the depth direction, the maximum velocity range becomes wider, while a lower number of velocity bands was seen without the convective term.

Figure 27 shows the liquid fraction with and without the convective term in the energy equation. It can be seen that without the convective term, the liquid fraction in all three planes is slightly larger than that with the convective term. This might be because without the convective term, there is no heat exchange between the hot liquid and cold solid so that the pool gets more heat, which makes a bigger pool shape.

As stated before, the analysis of convective term is also one of the novelty of this paper compared with Abederrazak et al. [13] Moreover, the influence of the convective term has an impact on the velocity due to the fact that convection produces changes in velocity while it has almost no impact on temperature and liquid fraction with the current boundary settings.

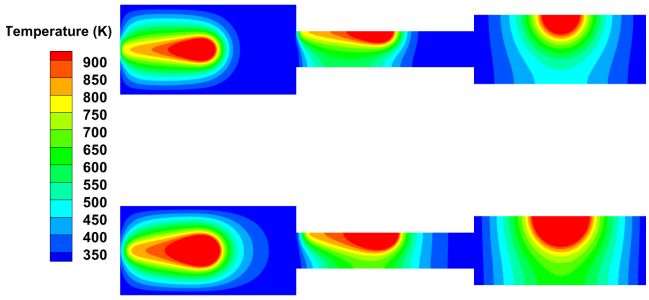

Figure 25. Temperature with and without taking the convective term into account

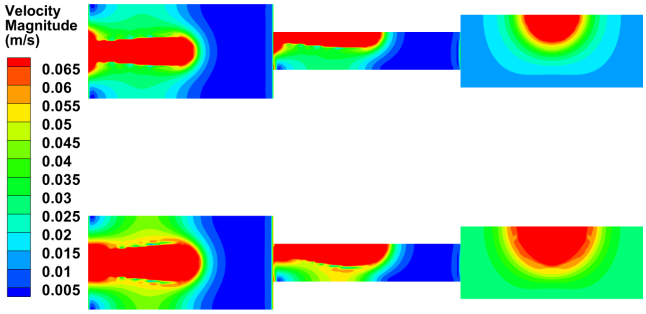

Figure 26. Velocity with and without taking the convective term into account

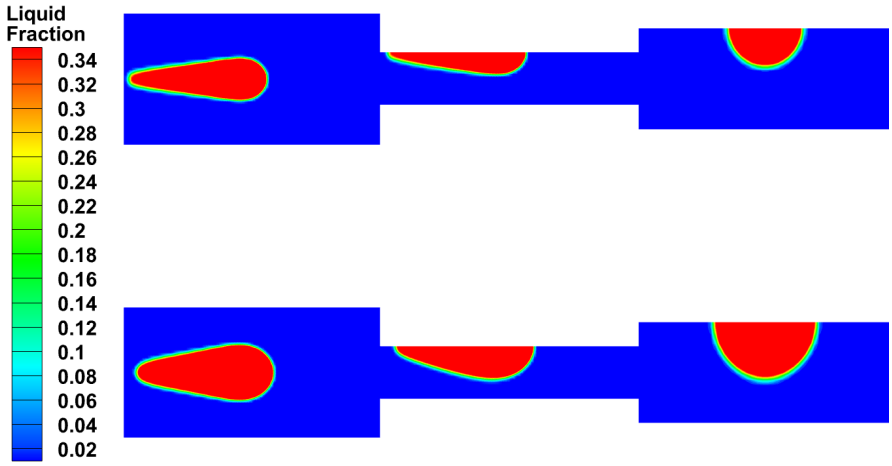

Figure 27. Liquid fraction distributions with and without taking the convective term into account

The effect of negative Marangoni force with three different shear stresses (6.4e-3 Pa, 6.4e-2 Pa and 6.4e-1 Pa) was investigated for Cases 10, 11 and 12. Figure 28 shows the velocity magnitude along the center x line with different shear stresses. As can be seen from the figure, the velocity magnitude is almost identical for the three different shear stresses. Figure 29 displays the velocity magnitude along the center y line. As can be seen from the figure, the results of Cases 10 and 11 are almost identical. While for Case 12 with the largest shear stress, the velocity magnitude in the center is lower than in the other two cases, while the velocity is larger at the edge of the workpiece. Figure 30 gives the velocity magnitude along the center z line. The figure shows that with smaller shear stress for Cases 10 and 11, the results are almost identical. For Case 12, with the largest shear stress, the velocity is a bit smaller than the other two cases near the top wall of the workpiece, while the velocity magnitude in the center is lower and the velocity is higher at the edge of the workpiece. Figure 30 is the velocity magnitude along the center z line. The figure shows that with smaller shear stress for Case 10 and 11, the results are almost identical, while near the top wall of the workpiece, Case 12 has lower velocity than the other two cases.

In addition, the Marangoni effect is also an important effect in laser welding application. Abederrazak et al. [13] did not analyze the specific influence of the Marangoni effect. Thus the analysis of the Marangoni effect is also one of the novelties of this paper. Through Figures 29 and 30, it can be seen that the Marangoni effect mainly affects flow in the y and z directions, which is in accordance with the definition of the Marangoni effect, because the Marangoni effect is due to the fact that surface tension gradient is different in y and z, while in the x direction, the surface tension gradient is almost identical.

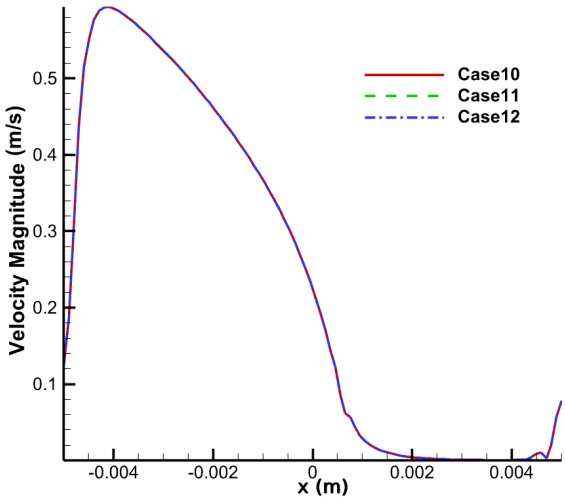

Figure 28. Velocity distribution with different shear stresses along x line

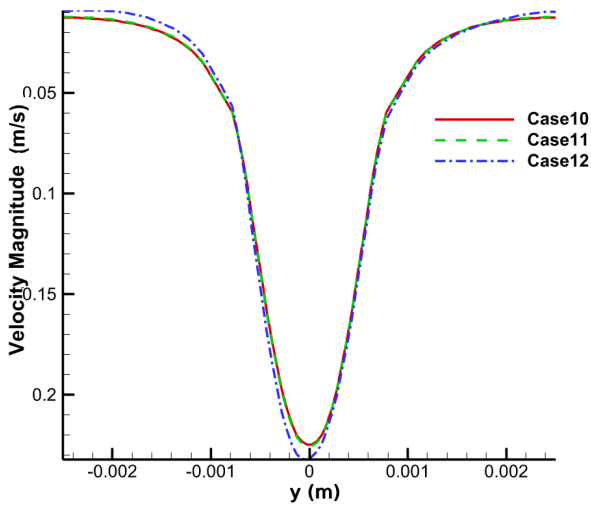

Figure 29. Velocity distribution with different shear stresses along y line

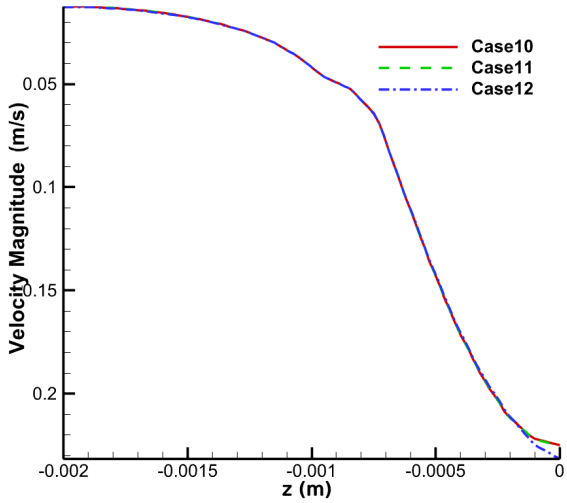

Figure 30. Velocity distribution with different shear stresses along z line

Figures 31, 32, and 33 show the velocity vector with Cases 10, 11 and 12 with different shear stresses. As can be seen in the figures, there are two vertices in Case 10, which is also mentioned in Abderrazak et al. [13]. However, with the increase of the shear stress, the two main vertices are not that obvious, as can be seen in Figure 32 and Figure 33.

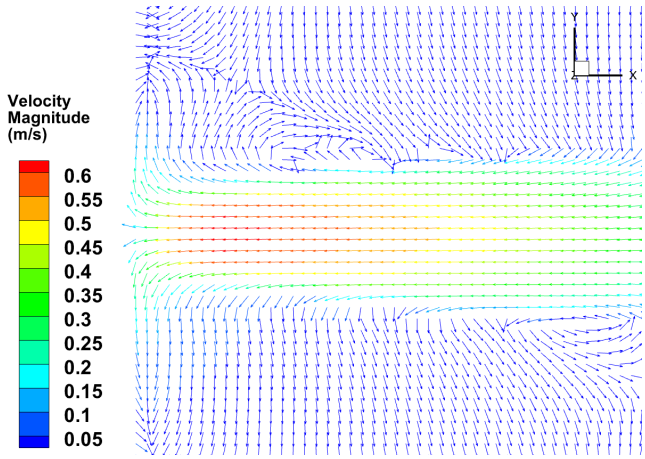

Figure 31. Velocity vector for Case 10

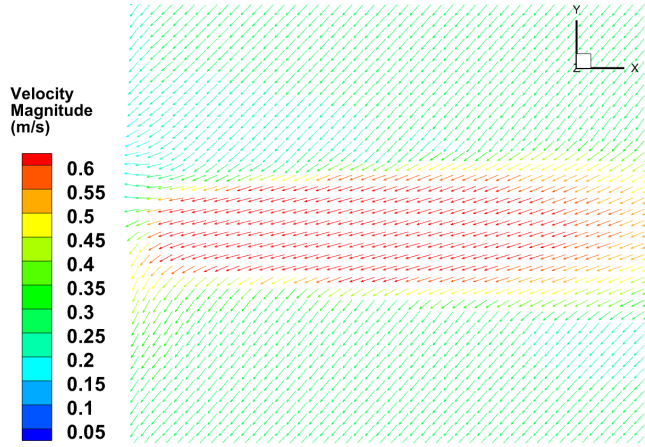

Figure 32. Velocity vector for Case 11

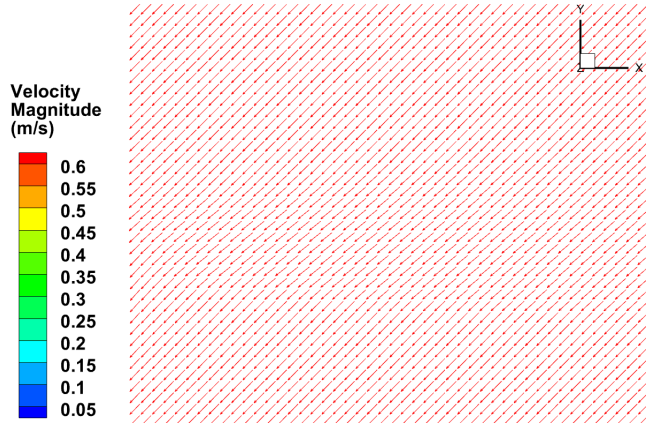

Figure 33. Velocity vector for Case 12

5. Conclusions and Recommendations

According to previous results and discussion, the following conclusions can be drawn:

- With the increase of the welding speed, the temperature and liquid fraction decreases and the contour forms a longer "tail" in width and length directions. However, velocity does not always decrease;
- Increasing the laser power leads to an increase in temperature, liquid fraction and velocity in all planes, which can also be seen from the temperature curves;
- The pool shape becomes more distorted and moves upward with larger welding speed and laser power;

- With the increase of the laser power, the penetration depth and bead width increase. With the increase of the welding speed, the penetration depth and welding speed decrease;
- Different shear stresses do not have much impact on the results of velocity magnitude along the center x line. However, along the center y line, the largest shear stress has the lowest velocity magnitude in the middle and the largest value on the edge of the workpiece. Moreover, along the center z line, the largest shear stress leads to the lowest velocity magnitude on the top of the wall. In addition, two vertices can be seen in Case 10 of this model, while with the increase of shear stress, the vertices become less obvious;
- Buoyancy force in this model does not make much difference to the results for velocity, temperature and liquid fraction;
- Without the presence of the convective term in the energy equation, the liquid fraction, temperature and velocity are higher than with the convective term in the energy equation.

Although several results were achieved based on this numerical model, there are still many extensions that can be done in the future. They are summarized as follows:

- The pool shape on the top wall was assumed to be flat; future work can remove this assumption and add a free surface tracking algorithm such as VOF or the level-set method;
- The laser beam in this model is a simple model that did not consider absorption or reflection. Future work can add a more realistic model of laser beam;
- The recoil pressure was not considered in this model; future work can add this feature;
- Other phenomena such as evaporation or plasma plume can also be added to this model in future work.

Acknowledgement. This project was financially supported by the Centre for Computational Engineering Sciences at Cranfield University under project code EEB6001R. For the purpose of open access, the authors have applied a Creative Commons Attribution (CC BY) licence to any author accepted manuscript version arising. Furthermore, we would like to acknowledge the IT support for using the High Performance Computing (HPC) facilities at Cranfield University, UK.

References

1. Steen, W. M. "Laser material processing-an overview." *Journal of Optics A: Pure and Applied Optics,* **5**(4), (2003), S3. doi: 10.1088/1464-4258/5/4/351.
2. Shin, Y. C., Benxin, W., Shuting, L., Gary, J. C., and Yao, Y. L. "Overview of Laser Applications in Manufacturing and Materials Processing in Recent Years." *Journal of Manufacturing Science and Engineering,* **142**(11), (2020). doi: 10.1115/1.4048397.
3. Eriksson, I., Gren, P., Powell, J., and Kaplan, A. "New high-speed photography technique for observation of fluid flow in laser welding." *Optical Engineering,* **49**(10) (2010), p. 100503. doi: 10.1117/1.3502567.

4. Norman, P., Engström, H., and Kaplan, A. "Theoretical analysis of photodiode monitoring of laser welding defects by imaging combined with modelling." *Journal of Physics D: Applied Physics,* **41**(19), (2008), p. 195502. doi: 10.1088/0022-3727/41/19/195502.
5. Zhang, Yanxi, Gao, Xiangdong, You, Deyong, and Zhang, Nanfeng. "Data-driven detection of laser welding defects based on real-time spectrometer signals." *IEEE Sensors Journal,* **19**(20) (2019), pp. 9364–9373. doi: 10.1109/JSEN.2019.2927268.
6. Swift-Hook, DT and Gick, AEF. "Penetration welding with lasers." *Welding journal,* **52**(11), (1973), 492s–499s.
7. Lankalapalli, Kishore N., Tu, Jay F., and Gartner, M. "A model for estimating penetration depth of laser welding processes." *Journal of Physics D: Applied Physics,* **29**(7), (1996), p. 1831. doi: 10.1088/0022-3727/29/7/018.
8. Dowden, J., Kapadia, P., and Postacioglu, N. "An analysis of the laser-plasma interaction in laser keyhole welding." *Journal of Physics D: Applied Physics,* **22**(6), (1989), p. 741. doi: 10.1088/0022-3727/22/6/004.
9. Carmignani, C., Mares, R., and Toselli, G. "Transient finite element analysis of deep penetration laser welding process in a singlepass butt-welded thick steel plate." *Computer methods in applied mechanics and engineering,* **179**(3-4), (1999), pp. 197–214. doi: 10.1016/S0045-7825(99)00043-2.
10. Ye, Xiao-Hu and Chen, Xi. "Three-dimensional modelling of heat transfer and fluid flow in laser full-penetration welding." *Journal of Physics D: Applied Physics,* **35**(10), (2002), p. 1049. doi: 10.1088/0022-3727/35/10/313.
11. Ki, Hyungson, Mohanty, PS, and Mazumder, Jyoti. "Modelling of high-density laser-material interaction using fast level set method." *Journal of Physics D: Applied Physics,* **34**(3), (2001), p. 364. doi: 10.1088/0022-3727/34/3/320.
12. Geiger, M., Leitz, K. H., and Koch, H. and Otto, A. "A 3D transient model of keyhole and melt pool dynamics in laser beam welding applied to the joining of zinc coated sheets." *Production Engineering,* **3**(2), (2009). doi: 10.1007/s11740-008-0148-7.
13. Abderrazak, K., Bannour, S., Mhiri, H., Lepalec, G., and Autric, M. "Numerical and experimental study of molten pool formation during continuous laser welding of AZ91 magnesium alloy." *Computational Materials Science,* **44**(3), (2009), pp. 858–866. doi: 10.1016/j.commatsci.2008.06.002.

Journal of Computational and Applied Mechanics, Vol. 17, No. 1, (2022), pp. 45–56
DOI: 10.32973/jcam.2022.003

TWO THEOREMS ON THE TORSIONAL RIGIDITY OF PIEZOELECTRIC BEAMS

István Ecsedi
Institute of Applied Mechanics, University of Miskolc
Miskolc-Egyetemváros, H-3515 Miskolc, Hungary
mechecs@uni-miskolc.hu

Ákos József Lengyel
Institute of Applied Mechanics, University of Miskolc
Miskolc-Egyetemváros, H-3515 Miskolc, Hungary
mechlen@uni-miskolc.hu

[Received: June 30, 2022; Accepted: September 18, 2022]

Abstract. In this paper two inequalities are presented for the torsional rigidity of homogeneous monoclinic piezoelectric beams. All results of the paper are based on the Saint-Venant theory of uniform torsion. The cross section of the considered elastic and piezoelectric beams may be simply connected or multiply connected two-dimensional bounded plane domain. Examples illustrate the proven inequality relations.

Mathematical Subject Classification: 74E10, 74F15, 74Q20
Keywords: piezoelectric beam, Saint-Venant's torsion, torsional rigidity

1. Introduction

Piezoelectric materials have several applications because of their unique behaviour. Piezoelectricity law is a constitute model that describes how the mechanical and electric fields are coupled within a material. Sensors and actuators are examples of active components made of linear piezoelectric materials which are widely used in smart structures. These structural components are often subjected to mechanical loading. The torsional deformation of these structural members is an important task. The present paper mainly deals with the torsional rigidity of monoclinic piezoelectric beams subjected to uniform torsion. Two theorems will be proven for the torsional rigidities of elastic beam and piezoelectric beam with the same cross sections, elastic stiffnesses and elastic flexibility (compliance) matrices. The proven inequality relations are illustrated in two examples.

The Saint-Venant torsion of linear piezoelectric beams has been considered by several researchers. Bisegna [1, 2] formulated and solved the Saint-Venant torsion problem for piezoelectric beams with a solid cross section by the use of Prandtl's stress function and electric displacement potential functions formulation. Yang studied the torsion of a solid circular ceramic cylinder which is polarized in tangential direction [3]. Rovenski et al. [4, 5] gave a torsion and electric potential functions formulation of

the Saint-Venant torsion for monoclinic homogeneous piezoelectric beams. In the two studies a coupled Neumann problem is derived for the torsion and electric potential functions. Exact and numerical solutions for elliptical and rectangular cross sections are presented in [4, 5]. Daví [6] obtained a coupled boundary-value problem for the torsion function and electric potential function from a three-dimensional linear static problem of a piezoelectric body by the application of the usual assumptions of the Saint-Venant's theory. Ecsedi and Baksa [7] gave a formulation of the Saint-Venant torsion for homogeneous monoclinic piezoelectric beams in terms of Prandtl's stress function and electric displacement potential function. The Prandtl stress function and electric displacement potential function satisfy a coupled Dirichlet problem in the multiply connected cross section of the piezoelectric beam [7]. In another paper by Ecsedi and Baksa a variational formulation is developed to solve the torsional deformation of homogeneous linear piezoelectric beams [8]. The variational formulation presented in [8] uses the torsion and electric potential functions as the independent quantities of the considered variational formulation. Rovenski and Abramovich [9] applied a linear analysis to non-homogeneous beams that consists of various monoclinic piezoelectric and elastic materials. Hassani and Faal [10] presented a work which deals with the torsional analysis of a cracked isotropic bar subjected to torsion. An outer piezoelectric coating layer is under both mechanical and electrical loading. The loading includes torque and electric displacement on the coating layer. The isotropic bar contains only cracks [10]. In a paper by Talebanpour and Hematiyan an approximate analytical method was formulated to solve the Saint-Venant torsion of orthotropic piezoelectric hollow bars [11]. Saint-Venant's torsion of an orthotropic non-homogeneous piezoelectric circular cylinder was studied in a paper of Ecsedi and Baksa [12].

The present paper deals with the Saint-Venant torsion of monoclinic homogeneous piezoelectric beams, focusing on torsional rigidity. Two inequality relations are proven for the torsional rigidity of the piezoelectric beams.

2. Formulation of the torsion problem in terms of torsion function and electric potential functions

The analytical approach presented by Rovenski et al. [4, 5] to the Saint-Venant torsion of piezoelectric beams is founded on Saint-Venant's semi-inverse method of uniform torsion. The analytical solution of the torsional problem for linearly electroelastic beams is based on the next displacement field according to the Saint-Venant theory and the assumption that the electric potential does not depend on the axial coordinate z

$$u = -\vartheta yz, \quad v = \vartheta xz, \quad w = \vartheta\omega(x,y), \tag{2.1}$$

$$\varphi = \vartheta\phi(x,y). \tag{2.2}$$

Here, ϑ is the rate of twist, u, v, w are the displacements in x, y and z directions, respectively, $\omega = \omega(x,y)$ is the torsion function, and $\varphi = \varphi(x,y)$ is the electric potential field. The origin of the coordinate system $Oxyz$ is placed at the left end cross section of the beam (Figure 1). It is not necessary that O coincides with the centre of the cross section at $z = 0$. The cross section A and its geometry are shown

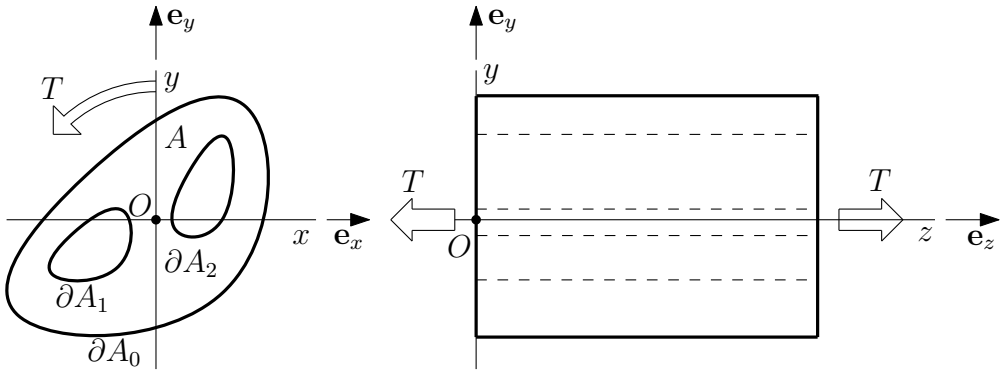

Figure 1. Piezoelectric beam with torsional load

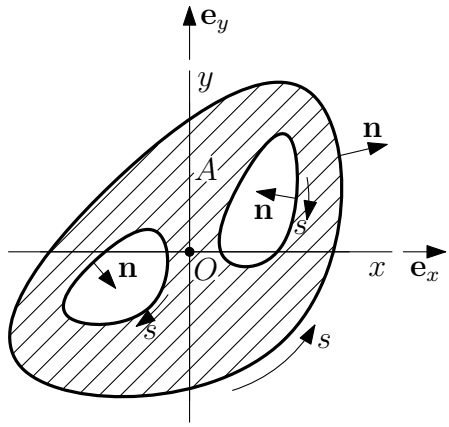

Figure 2. Multiply connected cross section

in Figure 2. The outer unit normal vector to the boundary curve ∂A is denoted by $\mathbf{n} = n_x\mathbf{e}_x + n_y\mathbf{e}_y$, where $\mathbf{e}_x$, $\mathbf{e}_y$ are the unit vectors in x and y directions, respectively. The arc-length defined on the boundary curve ∂A of the cross section A is denoted by s (Figure 2). The stress field, electric displacement and electric strength fields for a monoclinic piezoelectric beam in the case of Saint-Venant's torsion can be represented as [4, 5]

$$\boldsymbol{\tau}_z = \tau_{xz}\mathbf{e}_x + \tau_{yz}\mathbf{e}_y = \vartheta\mathbf{A}\cdot(\boldsymbol{\Omega} + \mathbf{e}\cdot\nabla\phi)\,, \tag{2.3}$$

$$\mathbf{D} = \vartheta\left(\mathbf{e}^{\mathrm{T}}\cdot\boldsymbol{\Omega} - \boldsymbol{\kappa}\cdot\nabla\phi\right), \tag{2.4}$$

$$\mathbf{E} = -\vartheta\nabla\phi, \quad \nabla = \frac{\partial}{\partial x}\mathbf{e}_x + \frac{\partial}{\partial y}\mathbf{e}_y, \tag{2.5}$$

where τ_{xz}, τ_{yz} are the shearing stresses, $\mathbf{D} = D_x\mathbf{e}_x + D_y\mathbf{e}_y$ is the electric displacement vector, $\mathbf{E} = E_x\mathbf{e}_x + E_y\mathbf{e}_y$ is the electric field vector, $\boldsymbol{\Omega} = \nabla\omega + \mathbf{e}_z\times\mathbf{R}$, $\mathbf{R} = x\mathbf{e}_x + y\mathbf{e}_y$,

$\mathbf{e}_z = \mathbf{e}_x \times \mathbf{e}_y$, cross between two vectors denotes their vector product,

$$\mathbf{A} = \begin{bmatrix} A_{55} & A_{54} \\ A_{45} & A_{44} \end{bmatrix}$$

is the matrix of elastic stiffness tensor ($A_{45} = A_{54}$),

$$\mathbf{e} = \begin{bmatrix} e_{15} & e_{25} \\ e_{14} & e_{24} \end{bmatrix}$$

is the matrix of the tensor of piezoelectric constants,

$$\boldsymbol{\kappa} = \begin{bmatrix} \kappa_{11} & \kappa_{12} \\ \kappa_{21} & \kappa_{22} \end{bmatrix}$$

is the matrix of the dielectric tensor ($\kappa_{12} = \kappa_{21}$), and the upper T in equation (2.4) indicates the operation of transpose and the scalar product is indicated by a dot.

From the equation of mechanical equilibrium, Gauss-Maxwell's equation, the stress boundary condition and electrical boundary conditions it follows that $\omega = \omega(x, y)$ and $\phi = \phi(x, y)$ is a solution of the next coupled Neumann's boundary-value problem [4, 5]

$$\nabla \cdot (\mathbf{A} \cdot \boldsymbol{\Omega} + \mathbf{e} \cdot \nabla\phi) = 0 \text{ in } A, \tag{2.6}$$

$$\nabla \cdot \left(\mathbf{e}^{\mathrm{T}} \cdot \boldsymbol{\Omega} - \boldsymbol{\kappa} \cdot \nabla\phi\right) = 0 \text{ in } A, \tag{2.7}$$

$$\mathbf{n} \cdot (\mathbf{A} \cdot \boldsymbol{\Omega} + \mathbf{e} \cdot \nabla\phi) = 0 \text{ on } \partial A, \tag{2.8}$$

$$\mathbf{n} \cdot \left(\mathbf{e}^{\mathrm{T}} \cdot \boldsymbol{\Omega} - \boldsymbol{\kappa} \cdot \nabla\phi\right) = 0 \text{ on } \partial A. \tag{2.9}$$

In equations (2.8) and (2.9)

$$\partial A = \sum_{i=1}^{p-1} \partial A_i \tag{2.10}$$

is the whole boundary curve of the hollow cross section A which consists of $p - 1$ holes, inner boundary curves.

The connection between the applied mechanical torque T and the rate of twist is [4, 5]

$$T = \vartheta S, \tag{2.11}$$

where S is the torsional rigidity of the electroelastic beam. Its value is obtained as

$$S = \int_A (\mathbf{e} \times \mathbf{R}) \cdot [\mathbf{A} \cdot \boldsymbol{\Omega} + \mathbf{e} \cdot \nabla\phi] \, \mathrm{d}A. \tag{2.12}$$

3. Formulation of the torsion problem in terms of Prandtl's stress function and electric displacement function

In terms of Prandtl's stress function $U = U(x, y)$ and the electric displacement function $F = F(x, y)$ the following coupled Dirichlet boundary-value problem can be derived [1, 2, 7]

$$\nabla \cdot (\mathbf{S} \cdot \nabla U + \mathbf{G} \cdot \nabla F) = -2 \text{ in } A, \tag{3.1}$$

$$\nabla \cdot \left(\mathbf{G}^{\mathrm{T}} \cdot \nabla U - \mathbf{H} \cdot \nabla F\right) = 0 \text{ in } A, \tag{3.2}$$

$$U = 0 \text{ and } F = 0 \text{ on } \partial A_0, \tag{3.3}$$

$$U = U_i = \text{constant on } \partial A_i \quad (i = 1, 2, \ldots, p), \tag{3.4}$$

$$F = F_i = \text{constant on } \partial A_i \quad (i = 1, 2, \ldots, p), \tag{3.5}$$

$$\oint_{\partial A_i} \mathbf{n} \cdot (\mathbf{S} \cdot \nabla U + \mathbf{G} \cdot \nabla F)\, \mathrm{d}s = 2A_i, \quad (i = 1, 2, \ldots, p-1), \tag{3.6}$$

$$\oint_{\partial A_i} \mathbf{n} \cdot \left(\mathbf{G}^{\mathrm{T}} \cdot \nabla U - \mathbf{H} \cdot \nabla F\right) \mathrm{d}s = 0, \quad (i = 1, 2, \ldots, p-1), \tag{3.7}$$

where

$$\mathbf{S} = \begin{bmatrix} s_{44} & -s_{45} \\ -s_{45} & s_{55} \end{bmatrix}$$

is the matrix of the elastic flexibility (compliance) tensor,

$$\mathbf{G} = \begin{bmatrix} g_{24} & -g_{14} \\ -g_{25} & g_{24} \end{bmatrix}$$

is the matrix of the piezoelectric impermeability tensor,

$$\mathbf{H} = \begin{bmatrix} \eta_{22} & -\eta_{12} \\ -\eta_{21} & \eta_{22} \end{bmatrix}$$

is the matrix of the dielectric impermeability tensor ($\eta_{12} = \eta_{21}$), and A_i is the area of the plane domain closed by the boundary curve ∂A_i ($i = 1, 2, \ldots, p$). The stress field $\boldsymbol{\tau}_z$ and electric displacement vector $\mathbf{D}$ can be represented as

$$\boldsymbol{\tau}_z = \vartheta \nabla U \times \mathbf{e}_z, \quad \mathbf{D} = \vartheta \nabla F \times \mathbf{e}_z. \tag{3.8}$$

The torsional rigidity in terms of Prandtl's stress function is as follows:

$$S = -\int_A \mathbf{R} \cdot \nabla U \mathrm{d}A = 2\left(\int_A U \mathrm{d}A + \sum_{i=1}^{p} U_i A_i\right). \tag{3.9}$$

4. Formulae for the torsional rigidity

In paper [8] it was proven that

$$S = \int_A (\boldsymbol{\Omega} \cdot \mathbf{A} \cdot \boldsymbol{\Omega} + 2\boldsymbol{\Omega} \cdot \mathbf{e} \cdot \nabla\phi - \nabla\phi \cdot \boldsymbol{\kappa} \cdot \nabla\phi)\, \mathrm{d}A. \tag{4.1}$$

Starting from the following equation

$$\begin{aligned} 0 = \int_{\partial A} \phi \mathbf{n} \cdot \left(\mathbf{e}^{\mathrm{T}} \cdot \boldsymbol{\Omega} - \boldsymbol{\kappa} \cdot \nabla\phi\right) \mathrm{d}s = \int_A \left(\nabla\phi \cdot \mathbf{e}^{\mathrm{T}} \cdot \boldsymbol{\Omega} - \nabla\phi \cdot \boldsymbol{\kappa} \cdot \nabla\phi\right) \mathrm{d}A + \\ + \int_A \phi \nabla \cdot \left(\mathbf{e}^{\mathrm{T}} \cdot \boldsymbol{\Omega} - \boldsymbol{\kappa} \cdot \nabla\phi\right) \mathrm{d}A = \\ = \int_A \boldsymbol{\Omega} \cdot \mathbf{e} \cdot \nabla\phi \mathrm{d}A - \int_A \nabla\phi \cdot \boldsymbol{\kappa} \cdot \nabla\phi \mathrm{d}A = 0 \end{aligned} \tag{4.2}$$

we can derive that

$$\int_A \boldsymbol{\Omega}\cdot\mathbf{e}\cdot\nabla\phi \mathrm{d}A = \int_A \nabla\phi\cdot\boldsymbol{\kappa}\cdot\nabla\phi \mathrm{d}A. \tag{4.3}$$

Combination of equation (4.1) with equation (4.3) gives

$$S = \int_A \left(\boldsymbol{\Omega}\cdot\mathbf{A}\cdot\boldsymbol{\Omega} + \nabla\phi\cdot\boldsymbol{\kappa}\cdot\nabla\phi\right)\mathrm{d}A, \tag{4.4}$$

which shows that $S > 0$ since $\mathbf{A}$ and $\boldsymbol{\kappa}$ are positive definite symmetric tensors [5, 7, 9]. In paper [7] it was proven that

$$S = \int_A \left(\nabla U\cdot\mathbf{S}\cdot\nabla U + \nabla F\cdot\mathbf{H}\cdot\nabla F\right)\mathrm{d}A. \tag{4.5}$$

Here, we note $\mathbf{S}$ and $\mathbf{H}$ are positive definite symmetric second order tensors.

5. Saint-Venant's torsion of elastic beam

The governing equations of Saint-Venant's torsion of elastic beam in terms of torsion function $\omega_0 = \omega_0(x, y)$ is obtained from equations (2.6–2.9) by the substitution

$$\mathbf{e} = \mathbf{0}. \tag{5.1}$$

In this case we have

$$\nabla\cdot(\mathbf{A}\cdot\boldsymbol{\Omega}_0) = 0 \text{ in } A, \tag{5.2}$$

$$\mathbf{n}\cdot\mathbf{A}\cdot\boldsymbol{\Omega}_0 = 0 \text{ on } \partial A, \tag{5.3}$$

$$\nabla\cdot(\boldsymbol{\kappa}\cdot\nabla\phi_0) = 0 \text{ in } A, \tag{5.4}$$

$$\mathbf{n}\cdot\boldsymbol{\kappa}\cdot\nabla\phi_0 = 0 \text{ on } \partial A. \tag{5.5}$$

From equations (5.4) and (5.5) it follows that

$$\nabla\phi_0 = \mathbf{0}, \quad \phi_0 = \text{constant}. \tag{5.6}$$

To prove this statement we consider the next equation

$$\int_A \phi_0\nabla\cdot(\boldsymbol{\kappa}\cdot\nabla\phi_0)\,\mathrm{d}A = \int_{\partial A}\phi_0\mathbf{n}\cdot\boldsymbol{\kappa}\cdot\nabla\phi_0\mathrm{d}s - \int_A \nabla\phi_0\cdot\boldsymbol{\kappa}\cdot\nabla\phi_0\mathrm{d}A = 0, \tag{5.7}$$

that is

$$\int_A \nabla\phi_0\cdot\boldsymbol{\kappa}\cdot\nabla\phi_0\mathrm{d}A = 0. \tag{5.8}$$

Since $\boldsymbol{\kappa}$ is the positive definite symmetric tensor from equation (5.8) it follows that

$$\nabla\phi_0 = \mathbf{0}, \quad \phi_0 = \text{constant in } A\cup\partial A. \tag{5.9}$$

The expression of the torsional rigidity for $\mathbf{e} = \mathbf{0}$ is as follows:

$$S_0 = \int_A (\mathbf{e}\times\mathbf{R})\cdot\boldsymbol{\Omega}_0\mathrm{d}A = \int_A \boldsymbol{\Omega}_0\cdot\mathbf{A}\cdot\boldsymbol{\Omega}_0\mathrm{d}A; \tag{5.10}$$

this expression follows from equation (4.4). The governing equations of Saint-Venant's torsion for elastic beams in terms of Prandtl's stress function are obtained from equations (3.1–3.7) by the substitution

$$\mathbf{G} = \mathbf{0}. \tag{5.11}$$

This substitution leads to the result

$$\nabla \cdot (\mathbf{S} \cdot \nabla U_0) = -2 \text{ in } A, \tag{5.12}$$

$$\nabla \cdot (\mathbf{H} \cdot \nabla F_0) = 0 \text{ in } A, \tag{5.13}$$

$$U_0 = 0 \text{ and } F_0 = 0 \text{ on } \partial A_0, \tag{5.14}$$

$$U_0 = U_{0i} = \text{constant on } \partial A_i, \quad (i = 1, 2, \ldots, p), \tag{5.15}$$

$$F_0 = F_{0i} = \text{constant on } \partial A_i, \quad (i = 1, 2, \ldots, p), \tag{5.16}$$

$$\oint_{\partial A_i} \mathbf{n} \cdot \mathbf{S} \cdot \nabla U_0 \mathrm{d}s = 2A_i, \quad (i = 1, 2, \ldots, p), \tag{5.17}$$

$$\int_{\partial A_i} \mathbf{n} \cdot \mathbf{H} \cdot \nabla F_0 \mathrm{d}s = 0, \quad (i = 1, 2, \ldots, p). \tag{5.18}$$

It is very easy to prove that if $F_0 = F_0(x, y)$ satisfies equations (5.13), $(5.14)_2$, (5.16) and (5.18) then we have

$$F_0 = F_0(x, y) = 0 \text{ in } A \cup \partial A. \tag{5.19}$$

The following equation is used to prove the above statement:

$$\begin{aligned} \int_A F_0 \nabla \cdot (\mathbf{H} \cdot \nabla F_0)\, \mathrm{d}A &= \int_{\partial A} F_0 \mathbf{n} \cdot \mathbf{H} \cdot \nabla F_0 \mathrm{d}s - \int_A \nabla F_0 \cdot \mathbf{H} \cdot \nabla F_0 \mathrm{d}A = \\ = \oint_{\partial A_0} F_0 \mathbf{n} \cdot \mathbf{H} \cdot \nabla F_0 \mathrm{d}s &+ \sum_{i=1}^{p} F_{0i} \oint_{\partial A_i} \mathbf{n} \cdot \mathbf{H} \cdot \nabla F_0 \mathrm{d}s - \int_A \nabla F_0 \cdot \mathbf{H} \cdot \nabla F_0 \mathrm{d}A = 0. \end{aligned} \tag{5.20}$$

From equation (3.4) it follows that

$$\int_A \nabla F_0 \cdot \mathbf{H} \cdot \nabla F_0 \mathrm{d}A = 0, \tag{5.21}$$

and since $\mathbf{H}$ is a positive definite two-dimensional second order tensor, this means that

$$\nabla F_0 = \text{constant}, \quad F_0 = 0 \text{ in } A \cup \partial A \tag{5.22}$$

according to the boundary condition $(5.14)_2$. The torsional rigidity of elastic beams in terms of $U_0 = U_0(x, y)$ can be represented as

$$S_0 = 2 \left(\int_A U_0(x, y) \mathrm{d}A + U_{0i} A_i \right) = \int_A \nabla U_0 \cdot \mathbf{S} \cdot \nabla U_0 \mathrm{d}A, \tag{5.23}$$

which follows from equation (4.5).

6. Inequality relations for the torsional rigidity

The proof of the inequality relations for the torsional rigidity is based on the Schwarz inequality

$$\int_A (\mathbf{P}\cdot\mathbf{M}\cdot\mathbf{P}+\mathbf{p}\cdot\mathbf{m}\cdot\mathbf{p})\,\mathrm{d}A \int_A (\mathbf{Q}\cdot\mathbf{M}\cdot\mathbf{Q}+\mathbf{q}\cdot\mathbf{m}\cdot\mathbf{q})\,\mathrm{d}A \geq \geq \left(\int_A (\mathbf{P}\cdot\mathbf{M}\cdot\mathbf{Q}+\mathbf{p}\cdot\mathbf{m}\cdot\mathbf{q})\,\mathrm{d}A\right)^2, \tag{6.1}$$

where $\mathbf{P}$, $\mathbf{p}$, $\mathbf{Q}$, $\mathbf{q}$ are arbitrary two-dimensional vectors

$$\mathbf{P}=P_x\mathbf{e}_x+P_y\mathbf{e}_y, \quad \mathbf{p}=p_x\mathbf{e}_x+p_y\mathbf{e}_y, \tag{6.2}$$

$$\mathbf{Q}=Q_x\mathbf{e}_x+Q_y\mathbf{e}_y, \quad \mathbf{q}=q_x\mathbf{e}_x+q_y\mathbf{e}_y, \tag{6.3}$$

$\mathbf{M}$, $\mathbf{m}$ are arbitrary two-dimensional positive definite symmetric second order tensors. Let

$$\mathbf{M}=\mathbf{A}, \quad \mathbf{m}=\boldsymbol{\kappa}, \quad \mathbf{P}=\boldsymbol{\Omega}, \quad \mathbf{p}=\nabla\phi, \quad \mathbf{Q}=\boldsymbol{\Omega}_0, \quad \mathbf{q}=\mathbf{0} \tag{6.4}$$

in inequality (6.1). We have

$$\int_A (\boldsymbol{\Omega}\cdot\mathbf{A}\cdot\boldsymbol{\Omega}+\nabla\phi\cdot\boldsymbol{\kappa}\cdot\nabla\phi)\,\mathrm{d}A \int_A (\boldsymbol{\Omega}_0\cdot\mathbf{A}\cdot\boldsymbol{\Omega}_0)\,\mathrm{d}A \geq \geq \left(\int_A (\boldsymbol{\Omega}\cdot\mathbf{A}\cdot\boldsymbol{\Omega}_0)\,\mathrm{d}A\right)^2, \tag{6.5}$$

A simple computation gives

$$\begin{aligned} \int_A (\boldsymbol{\Omega}\cdot\mathbf{A}\cdot\boldsymbol{\Omega}_0)\,\mathrm{d}A &= \int_A (\nabla\omega+\mathbf{e}_z\times\mathbf{R})\cdot\mathbf{A}\cdot\boldsymbol{\Omega}_0\mathrm{d}A = \\ &= \int_A \nabla\omega\cdot\mathbf{A}\cdot\boldsymbol{\Omega}_0\mathrm{d}A + \int_A (\mathbf{e}_z\times\mathbf{R})\cdot\mathbf{A}\cdot\boldsymbol{\Omega}_0\mathrm{d}A = \\ &\int_{\partial A} \omega\mathbf{n}\cdot\mathbf{A}\cdot\boldsymbol{\Omega}_0\mathrm{d}s - \int_A \omega\nabla\cdot(\mathbf{A}\cdot\boldsymbol{\Omega}_0)\,\mathrm{d}A + S_0 = S_0. \end{aligned} \tag{6.6}$$

From inequality (6.5) and equation (6.6) it follows that

$$S(\mathbf{A},\boldsymbol{\kappa},\mathbf{e}) \geq S_0(\mathbf{A},\boldsymbol{\kappa}). \tag{6.7}$$

This inequality relation is valid if the cross section of the piezoelastic beam and elastic beam ($\mathbf{e}=\mathbf{0}$) have the same cross section. By the use of Prandtl's stress function and elastic displacement formulation we can derive another inequality relation for the torsional rigidity. Let

$$\mathbf{M}=\mathbf{S}, \quad \mathbf{m}=\mathbf{H}, \quad \mathbf{P}=\nabla U, \quad \mathbf{p}=\nabla F, \quad \mathbf{Q}=\nabla U_0, \quad \mathbf{q}=\mathbf{0} \tag{6.8}$$

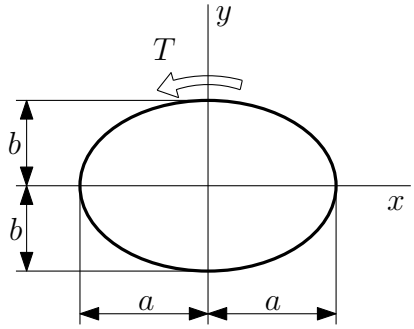

Figure 3. Solid elliptical cross section

in inequality (6.1). It is obvious that

$$\int_A (\nabla U \cdot \mathbf{S} \cdot \nabla U + \nabla F \cdot \mathbf{H} \cdot \nabla F)\,\mathrm{d}A \int_A (\nabla U_0 \cdot \mathbf{S} \cdot \nabla U_0)\,\mathrm{d}A \geq \geq \left(\int_A (\nabla U \cdot \mathbf{S} \cdot \nabla U_0)\,\mathrm{d}A \right)^2, \tag{6.9}$$

and we have

$$\begin{aligned} \int_A \nabla U \cdot \mathbf{S} \cdot \nabla U_0 \mathrm{d}A &= \int_{\partial A} U\mathbf{n} \cdot \mathbf{S} \cdot \nabla U_0 \mathrm{d}s - \int_A U \nabla \cdot (\mathbf{S} \cdot \nabla U_0)\,\mathrm{d}A = \\ &= \int_{\partial A_0} U\mathbf{n} \cdot \mathbf{S} \cdot \nabla U_0 \mathrm{d}s + \sum_{i=1}^{p} U_i \oint_{\partial A_i} \mathbf{n} \cdot \mathbf{S} \cdot \nabla U_0 \mathrm{d}s + 2\int_A U \mathrm{d}A = \\ &= 2\left(\int_A U \mathrm{d}A + \sum_{i=1}^{p} U_i A_i \right) = S. \end{aligned} \tag{6.10}$$

Substitution of equation (6.10) into inequality relation (6.9) gives the following inequality relation for the torsional rigidities $S(\mathbf{S}, \mathbf{G}, \mathbf{H})$ and $S_0(\mathbf{S}, \mathbf{H})$

$$S_0(\mathbf{S}, \mathbf{H}) \geq S(\mathbf{S}, \mathbf{G}, \mathbf{H}). \tag{6.11}$$

7. Illustration of inequality relations

The application of the inequalities (6.7) and (6.11) is illustrated by the example of a twisted orthotropic piezoelectric beam with a solid elliptical cross section (figure 3). The solution of the torsion problem of elliptical cross section shown in Figure 3 in terms of $\omega = \omega(x, y)$ and $\phi = \phi(x, y)$ is as follows:

$$\omega(x, y) = -\frac{c_\omega}{c} xy, \quad \phi(x, y) = -\frac{c_\varphi}{c} xy, \tag{7.1}$$

where

$$c_\omega = \left(a_{44}\kappa_{22} + e_{24}^2\right) a^4 + \left(a_{44}\kappa_{11} - a_{55}\kappa_{22}\right) a^2 b^2 - \left(a_{55}\kappa_{11} + e_{15}^2\right) b^4, \tag{7.2}$$

$$c_\varphi = 2a^2 b^2 \left(-a_{55}e_{24} + a_{44}e_{15}\right), \tag{7.3}$$

$$c = \left(a_{44}\kappa_{22} + e_{24}^2\right) a^4 + \left(a_{55}\kappa_{22} + a_{44}\kappa_{11} + 2e_{15}e_{24}\right) a^2 b^2 + \left(a_{55}\kappa_{11} + e_{15}^2\right) b^4. \tag{7.4}$$

Here we note that for orthotropic piezoelectric material $a_{45} = a_{54} = 0$ and $e_{25} = e_{14} = 0$. The expression of the torsional rigidity is

$$S\left(\mathbf{A}, \mathbf{e}, \boldsymbol{\kappa}\right) = \frac{a_{55}a^2\left(a_{44}\kappa_{22} + e_{24}^2\right) + a_{44}b^2\left(a_{55}\kappa_{11} + e_{15}^2\right)}{c} a^3 b^3 \pi. \tag{7.5}$$

From equation (7.5) we get

$$S_0\left(\mathbf{A}, \boldsymbol{\kappa}\right) = \frac{a_{55}a_{44}a^3b^3\pi}{a_{44}a^2 + a_{55}b^2}. \tag{7.6}$$

Combination of equation (7.5) with equation (7.6) gives

$$S\left(\mathbf{A}, \mathbf{e}, \boldsymbol{\kappa}\right) - S_0\left(\mathbf{A}, \boldsymbol{\kappa}\right) = \frac{\left(a_{44}e_{15} - a_{55}e_{24}\right)^2}{a^2 a_{44} + b^2 a_{55}} \frac{a^5 b^5 \pi}{K} \geq 0 \tag{7.7}$$

according to inequality (6.7) where

$$K = b^4 a_{55}\kappa_{11} + b^2 a^2 a_{55}\kappa_{22} + b^2 a^2 a_{44}\kappa_{11} + a^4 a_{44}\kappa_{22} + \left(e_{15}b^2 + e_{24}a^2\right)^2 \tag{7.8}$$

The Prandtl stress function and elastic displacement function formulation for the orthotropic piezoelectric beam when $s_{45} = s_{54} = 0$ and $g_{25} = g_{14} = 0$ can be represented as

$$U(x, y) = \frac{c_u}{C}\left(1 - \frac{x^2}{a^2} - \frac{y^2}{b^2}\right), \tag{7.9}$$

$$F(x, y) = \frac{c_f}{C}\left(1 - \frac{x^2}{a^2} - \frac{y^2}{b^2}\right). \tag{7.10}$$

Here,

$$c_u = a^2 b^2 \left(a^2\eta_{11} + b^2\eta_{22}\right), \tag{7.11}$$

$$c_f = a^2 b^2 \left(a_{55}g_{15} + b^2 g_{24}\right), \tag{7.12}$$

$$C = \left(a^2 s_{55} + b^2 s_{44}\right)\left(a^2\eta_{11} + b^2\eta_{22}\right) + \left(g_{15}a^2 + g_{24}b^2\right)^2. \tag{7.13}$$

The expression of torsional rigidity of the orthotropic piezoelectric solid elliptical cross section is as follows:

$$S\left(\mathbf{S}, \mathbf{G}, \mathbf{H}\right) = a^3 b^3 \pi \frac{\eta_{11}a^2 + \eta_{22}b^2}{\left(a^2 s_{55} + b^2 s_{44}\right)\left(a^2\eta_{11} + b^2\eta_{22}\right) + \left(g_{15}a^2 + g_{24}b^2\right)^2}. \tag{7.14}$$

From the formula (7.14) we can obtain the torsional rigidity of the elastic beam with the substitution $g_{15} = g_{24} = 0$

$$S_0\left(\mathbf{S}, \mathbf{H}\right) = \frac{\pi a^3 b^3}{s_{55}a^2 + s_{44}b^2}. \tag{7.15}$$

From formulae (7.14) and (7.15) it follows that

$$S_0(\mathbf{S},\mathbf{H}) - S(\mathbf{S},\mathbf{G},\mathbf{H}) =$$

$$= a^3b^3\pi\left(\frac{1}{s_{55}a^2+s_{44}b^2} - \frac{1}{\frac{(g_{15}a^2+g_{24}b^2)^2}{\eta_{11}a^2-\eta_{22}b^2}+s_{55}a^2+s_{44}b^2}\right) \geq 0 \tag{7.16}$$

according to the inequality relation (6.11). It must be noted that for a double connected elliptical cross section whose main axes are a, λa and b, λb $(0 < \lambda < 1)$ formulae (7.5) and (7.6) can be represented as

$$S(\mathbf{A},\mathbf{e},\boldsymbol{\kappa}) = \frac{a^3b^3\pi}{c}\left(1-\lambda^4\right)\left[a_{55}a^2\left(a_{44}\kappa_{22}+e_{24}^2\right)+a_{44}b^2\left(a_{55}\kappa_{11}+e_{15}^2\right)\right], \tag{7.17}$$

$$S_0(\mathbf{A},\boldsymbol{\kappa}) = a^3b^3\pi\left(1-\lambda^4\right)\frac{a_{55}a_{44}}{a_{44}a^2+a_{55}b^2}. \tag{7.18}$$

These equations show that equation (7.7) is valid for a hollow elliptical cross as well. A similar remark is valid for equation (7.16) since in this case

$$S(\mathbf{S},\mathbf{G},\mathbf{H}) = \frac{\pi a^3b^3}{\frac{(a^2g_{15}+b^2g_{24})^2}{\eta_{11}a^2+\eta_{22}b^2}+s_{55}a^2+s_{44}b^2}\left(1-\lambda^4\right), \tag{7.19}$$

$$S_0(\mathbf{S},\mathbf{H}) = \frac{\pi a^3b^3}{s_{55}a^2+s_{44}b^2}\left(1-\lambda^4\right). \tag{7.20}$$

8. Conclusion

This paper deals with the torsional rigidity of monoclinic piezoelectric beams subjected to uniform torsion. Two inequalities are presented for the torsional rigidity which concern the connection of torsional rigidities of piezoelectric and elastic beams. Both beams have the same cross sections and their elastic properties are also the same. This means that the elastic stiffness and elastic flexibility (compliance) matrices for the two beams are equal. An example illustrates the proven statements.

References

1. Bisegna, P. "The Saint-Venant problem in the linear theory of piezoelectricity." *Atti Dei Convegni Lincei-Accademia Nazionale Dei Lincei,* **140**, (1998), pp. 151–165.
2. Bisegna, P. "The Saint-Venant problem for monoclinic piezoelectric cylinders." *Zeitschrift für Angewandte Mathematik und Mechanik,* **78**, (1999), pp. 147–165. DOI: 10.1002/(SICI)1521-4001(199803)78:3<147::AID-ZAMM147>3.0.CO;2-Z.
3. Yang, J. *An Introduction to the Theory of Piezoelectricity.* Springer, Boston, MA, 2005.
4. Rovenski, V., Harash, E., and Abramovich, H. "Saint-Venant's Problem for Homogeneous Piezoelectric Beams." *TAE Report No.* 967, (2006), pp. 1–100.

5. Rovenski, V., Harash, E., and Abramovich, H. "Saint-Venant's problem for homogeneous piezoelectric beams." *Journal of Applied Mechanics,* **74**(6), (2007), pp. 1095–1103. DOI: 10.1115/1.2722315.
6. Daví, F. "Saint-Venant's problem for linear piezoelectric bodies." *Journal of Elasticity,* **43**(3), (1996), pp. 227–245. DOI: 10.1007/bf00042502.
7. Ecsedi, I. and Baksa, A. "Prandtl's formulation for the Saint–Venant's torsion of homogeneous piezoelectric beams." *International Journal of Solids and Structures,* **47**(22-23) (2010), pp. 3076–3083. DOI: 10.1016/j.ijsolstr.2010.07.007.
8. Ecsedi, I. and Baksa, A. "A variational formulation for the torsional problem of piezoelastic beams." *Applied Mathematical Modelling,* **36**(4), (2012), pp. 1668–1677. DOI: 10.1016/j.apm.2011.09.021.
9. Rovenski, V. and Abramovich, H. "Saint-Venant's problem for compound piezoelectric beams." *Journal of Elasticity,* **96**(2), (2009), pp. 105–127. DOI: 10.1007/s10659-009-9201-9.
10. Hassani, A. R. and Faal, R. T. "Torsion analysis of cracked circular bars actuated by a piezoelectric coating." *Smart Materials and Structures,* **25**(12), (2016), p. 125030. DOI: 10.1088/0964-1726/25/12/125030.
11. Talebanpour, A. and Hematiyan, M. R. "Torsional analysis of piezoelectric hollow bars." *International Journal of Applied Mechanics,* **6**(2), (2014), p. 1450019. DOI: 10.1142/S1758825114500197.
12. Ecsedi, I. and Baksa, A. "Saint-Venant torsion of non-homogeneous orthotropic circular cylinder." *Archive of Applied Mechanics,* **90**(4), (2020), pp. 815–827. DOI: 10.1007/s00419-019-01640-y.

Journal of Computational and Applied Mechanics, Vol. 17, No. 1, (2022), pp. 57–82
DOI: 10.32973/jcam.2022.004

EVALUATION OF THE SU2 OPEN-SOURCE CODE FOR A HYPERSONIC FLOW AT MACH NUMBER 5

Jia-Ming Yeap
Centre for Computational Engineering Sciences, Cranfield University, Cranfield, Bedfordshire, MK43 0AL, United Kingdom
jmryan93@gmail.com

Zeeshan A. Rana
Centre for Aeronautics, Cranfield University, Cranfield, Bedfordshire, MK43 0AL, United Kingdom
zeeshan.rana@cranfield.ac.uk

László Könözsy
Centre for Computational Engineering Sciences, Cranfield University, Cranfield, Bedfordshire, MK43 0AL, United Kingdom
laszlo.konozsy@cranfield.ac.uk

Karl W. Jenkins
Centre for Computational Engineering Sciences, Cranfield University, Cranfield, Bedfordshire, MK43 0AL, United Kingdom
k.w.jenkins@cranfield.ac.uk

[Received: May 23, 2022; Accepted: October 29, 2022]

Abstract. This paper presents the evaluation of the Stanford University Unstructured (SU2) open-source computational software package for a high Mach number 5 flow. The test case selected is an impinging shock wave turbulent boundary layer interaction (SWTBLI) on a flat plate where the experimental data of Schülein et al. [27] is used for validation purposes. Two turbulence models, the Spalart–Allmaras (SA) and the k-ω Shear Stress Transport (SST) within the SU2 code are evaluated in this study. Flow parameters, such as skin friction, wall pressure distribution and boundary layer profiles are compared with experimental values. The results demonstrate the performance of the SU2 code at a high Mach number flow and highlight its limitations in predicting fluid flow physics. At higher shock generator angles, the discrepancy between experimental and CFD data is more significant. Within the interaction and flow separation zones, a smaller separation bubble and delayed separation are predicted by the SA model while the k-ω SST model predicts early separation. Both models are able to predict wall pressure distribution correctly within the experimental values. However, discrepancies were observed in the prediction of skin friction due to the inability of the models to capture the boundary layer recovery after shock impingement.

Mathematical Subject Classification: 76N30, 76M10, 76M12, 76W05
Keywords: Shock Wave Turbulent Boundary Layer Interactions (SWTBLI), Turbulence Modeling, Flow Separation, Hypersonic Flows, Impinging Shock

1. Introduction

A hypersonic air-breathing propulsion (HAP) device scoops air from the atmosphere to generate thrust [1], in contrast to a rocket propulsion engine where on-board liquid oxygen is utilized for combustion. The obvious advantage of a HAP device is the reduction in payload requirement (on-board oxygen) for the aircraft; however, such propulsion systems suffer from low performance at subsonic speeds, and thus are dependent on other propulsion devices for the take-off procedure [2]. Ramjet and scramjet are both HAP devices used for flights above sonic conditions; combustion in a ramjet occurs at subsonic speeds, while for the scramjet combustion is carried out at supersonic speeds. The concept of scramjet engines was first devised around the 1950s [3], a period of time when the capability of Computational Fluid Dynamics (CFD) was very limited. The first successful flight of a scramjet engine, named HyShot-II and built at the University of Queensland, took place in July of 2002 [4]. Further experiments were conducted [5, 6] and detailed computational investigations have also been performed on the HyShot-II scramjet. Karl et al. [7] was perhaps the first to present the experimental investigations on the overall flow field of the HyShot-II and validated their findings through RANS (Reynolds-Averaged Navier–Stokes) modeling. This was followed by several further investigations on the same geometry. Berglund et al. [8], Fureby et al. [9] and Chapuis et al. [10] investigated the supersonic combustion phenomenon inside the HyShot-II scramjet combustor using both the time-averaged RANS and the time-accurate LES (Large Eddy Simulations) turbulence modeling approaches. You et al. [11] presented a detailed investigation on the fuel injection and mixing inside the same combustor to extend the understanding through RANS and DES (Detached Eddy Simulation) formulations. Many further studies have since been carried out [12, 13, 14] to further understand the flow dynamics around and inside the HyShot-II geometry. Owing to the complexities associated with the scramjet, a more generic model of the supersonic flow inside the combustion chamber with transverse sonic jet injection [15, 16, 17] was used to understand the complex flow characteristics and mixing of air with fuel where Shock Wave Turbulent Boundary Layer Interactions (SWTBLI) also play a major role.

One complex flow phonomenon in a supersonic combustion chamber is the SWTBLI. Typical applications of SWTBLI include supersonic/hypersonic engines, inlets of high speed air-breathing propulsion vehicles and high Mach number flows over control surfaces [18, 19]. Although efforts were exerted at the design stage to avoid any shock wave entering the combustion chamber of the HyShot-II [7, 12], a shock train was observed traveling inside the combustion chamber giving rise to the SWTBLI phenomenon. This type of interaction causes the boundary layer to separate and develop recirculation of flow. As the scramjet employs auto-ignition, this recirculation can have an effect on the combustion process and even results in unsteady unstart in HyShot-II [12, 13]. Shock wave boundary layer interaction can have ahuge influence on the nature of high Mach number flows, compromising the safety and risk management for a specific industrial system such as a supersonic engine inlet. The interaction between shocks and boundary layer can cause an abrupt deceleration in fluid flow

and thickening of the turbulent boundary layer [20]. In the separation zone, three-dimensional effects in the form of Goertler vortices have also been reported by several researchers [21, 22, 23, 24]. Along with the occurrence of flow separation, high pressure fluctuations and wall heat flux could be observed in the interaction region. The assumption of stable compressive deceleration in the freestream flow into a hypersonic air intake as an isentropic process is invalid in true flight conditions [18].

Most research in this area is still centered around test cases with simple geometries such as a flat plate and shock generator [21]. An impinging SWTBLI on a flat plate is considered as a canonical test case [25], along with some other typical SWTBLI configurations such as compression ramp and expansion-compression corner flows [26]. Schülein et al. [27] conducted detailed experiments on an impinging SWTBLI on a flat plate and presented results for the skin friction and heat transfer measurements, carrying out the experiment in the DLR Ludwieg-Tube (DNW-RNG) wind tunnel facility in Göttingen. The test model consisted of a flat plate of 500 mm in length and 400 mm in width, as well as a shock generator of 300 mm in length and 400 mm in width. In Figure 1, the shock generator is oriented at a shock generator angle β and its leading edge and trailing edge are positioned such that the shock impingement location is always 350 mm from the leading edge of flat plate at all freestream Mach numbers and shock generator angles. A Further comprehensive database of supersonic/hypersonic test cases of a Mach number of at least 3 was also reported [28, 29], ranging from an impinging shock to three-dimensional double fin configurations.

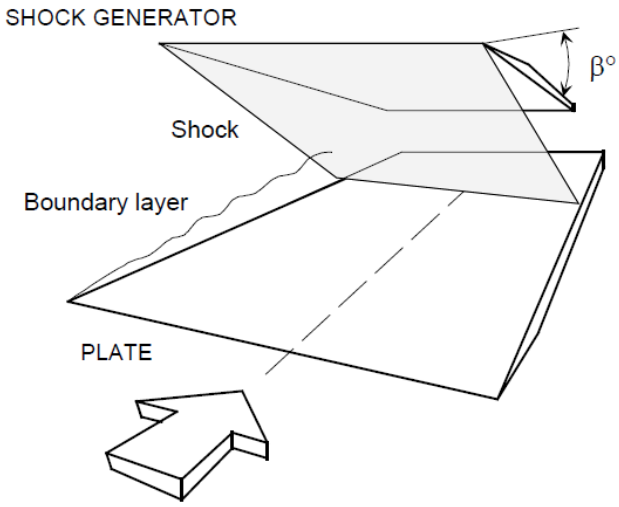

Figure 1. Sketch of the test model from Schülein et al. [27]

Fedorova et al. [30] conducted a CFD analysis of the experiment of Schülein et al. [27] using unsteady Favre-Averaged Navier–Stokes (FANS) equations along with the

k-ω turbulence model of Wilcox [40]. The results demonstrate that the disagreement between numerical and experimental data is greater with increasing interaction strength. At β of 6° and 10°, good agreement is reported for the flow parameters such as skin friction and boundary layer profiles; however, skin friction downstream of the impingement point was underestimated at all angles investigated. Leger and Poggie [31, 32] illustrated both, the weak and the strong interaction cases of an impinging SWTBLI on a flat plate and discussed the nature of the shock wave boundary layer interactions. They also observed the reduction in the wall shear stress and increase in the wall pressure across the SWTBLI region due to a double-shock event in the case of weak interactions. Several more experimental and numerical investigations were carried out for this particular arrangement and its variants. However, the experiment of Schülein et al. [27] remains the fundamental source of data for verification and validation of computational methods and turbulence models [33].

Reynolds-averaged modeling is considered to be a low accuracy approach in predicting skin friction and heat transfer distributions while it performs better in modeling primary separation and pressure fields. In a strong interaction case, the agreement of experimental and CFD data is reduced. This paper presents an attempt to evaluate the Stanford University Unstructured (SU2) open-source CFD software package [34, 35, 36] using compressible Reynolds-averaged turbulence modeling approaches for an impinging SWTBLI on flat plate at Mach number of 5 in comparison with the experimental data of Schülein et al. [27]. The main objective here is the validation of the numerical results performed with the use of the SU2 code for an impinging SWTBLI case at Mach number 5. Furthermore, another goal is to understand the limitations of the SU2 code for the investigations of complex flow phenomena of SWTBLI at a high Mach number flow. In this study, due to the constraint of computational resources for very high-speed flows, two-dimensional simulations have been performed.

2. Methodology and Computational Framework

2.1. **The SU2 open-source code.** The SU2 code is an open-source Computational Fluid Dynamics (CFD) software package, first developed by Aerospace Design Laboratory at Stanford University. One of the motivations behind the SU2 code is to solve problems which involve discretization of Partial Differential Equations (PDEs) such as Navier-Stokes and optimization of PDE-constrained problems. It is a software collection based on programming languages such as C++, Python, OpenMPI and Metis. Gradient-based adjoint solver capability is included in the development of the SU2 code through mesh adaption process driven by a specific function such as lift or drag. The SU2 code is based on Finite Volume (FV) or Finite Element (FE) methods and complete description of the SU2 code along with its structure can be found in [34, 35, 36]. Since the first introduction of the SU2 open-source code, it has been validated for a number of benchmark cases such as low Mach flows over an NACA0012 aerofoil [34, 35], supersonic or hypersonic flow regimes [34] as in a Lockheed N+2 aircraft at Mach number of 1.7, and the RAM-C II flight test vehicle at the Mach number of 16 with a plasma solver including additional sets of equations and source terms to take into account non-equilibrium effects [36].

2.2. **Governing equations of high-speed compressible flows.** The governing equations of high-speed compressible, viscous, heat-conducting flows, i.e., the instantaneous mass, momentum and enegy conservation equations, are considered [40] as

$$\frac{\partial \rho}{\partial t} + \frac{\partial}{\partial x_i}\left(\rho u_i\right) = 0, \tag{2.1}$$

$$\frac{\partial}{\partial t}\left(\rho u_i\right) + \frac{\partial}{\partial x_j}\left(\rho u_i u_j\right) = -\frac{\partial p}{\partial x_j} + \frac{\partial \tau_{ij}}{\partial x_j}, \tag{2.2}$$

$$\frac{\partial}{\partial t}\left(\rho E\right) + \frac{\partial}{\partial x_j}\left(\rho u_j E\right) = -\frac{\partial}{\partial x_j}\left(p u_j\right) + \frac{\partial}{\partial x_j}\left(u_i \tau_{ij} + \lambda \frac{\partial T}{\partial x_j}\right), \tag{2.3}$$

where ρ is the fluid density, u_i is the component of the velocity vector ($i = 1{,}2$ for two-dimensional and $i = 1{,}2{,}3$ for three-dimensional problems), p is the pressure field which is a function of the density, τ_{ij} describes the components of the viscous stress tensor, E is the total energy per unit mass, λ is the thermal conductivity, and T is the temperature. The elements of the viscous stress tensor can be expressed by

$$\tau_{ij} = \mu\left(\frac{\partial u_i}{\partial x_j} + \frac{\partial u_j}{\partial x_i}\right) - \frac{2}{3}\mu \frac{\partial u_k}{\partial x_k}\delta_{ij}, \tag{2.4}$$

where μ is the temperature dependent dynamic viscosity of the fluid, and δ_{ij} is the Kronecker delta ($\delta_{ij} = 1$ when $i = j$ and $\delta_{ij} = 0$ when $i \neq j$). For an ideal (perfect) gas, the relationship among pressure, density and temperature in the governing equations (2.1)–(2.3) can be computed by the equation of state as

$$p = \rho R T, \tag{2.5}$$

where R is the perfect (ideal) gas constant. The thermal conductivity λ in the energy equation (2.3) can be expressed by

$$\lambda = \frac{\mu c_p}{Pr}, \tag{2.6}$$

where c_p is the specific heat, and Pr is the dimensionless Prandtl number. In the thermal conductivity λ expression (2.6), the specific heat can be computed as

$$c_p = \frac{\gamma R}{\gamma - 1}, \tag{2.7}$$

where γ is the specific heat ratio. In this numerical study, the SU2 code has been used for solving the Reynolds-Averaged Navier–Stokes (RANS) equations, i.e., the instantaneous governing Eqs. (2.1)–(2.3) after Reynolds-averaging. Therefore, the effective viscosity μ_{eff} is introduced instead of the dynamic viscosity μ of the fluid for turbulence modeling. In that case, the effective viscosity μ_{eff} can be decomposed into the sum of the dynamic μ and the turbulent eddy viscosity μ_t as

$$\mu_{eff} = \mu + \mu_t. \tag{2.8}$$

The effective thermal conductivity λ_{eff} can also be introduced for turbulence modeling purposes and can be decomposed into two parts as follows:

$$\lambda_{eff} = \frac{\mu}{Pr} + \frac{\mu_t}{Pr_t}, \tag{2.9}$$

where Pr_t is the turbulent Prandtl number. Note that in a compressible fluid flow solver, the Sutherland law has to be satisfied by dynamic viscosity μ and turbulent eddy viscosity μ_t, which are included in the appropriately chosen turbulence models. Based on user preferences, the SU2 solver can be configured to perform computations in either dimensional or non-dimensional form. A wide selection of boundary conditions is available in the SU2 compressible solver, including Euler-type wall (inviscid), no-slip wall with isothermal and adiabatic options, symmetry wall, far-field and periodic boundary conditions. At the inlet and outlet sections and surfaces, characteristic-based boundary conditions such as mass flow rate, supersonic inlet properties, stagnation conditions, back pressure at the outlet and supersonic outlet can be prescribed. Two engineering turbulence models are available in the SU2 code which are evaluated in the present numerical study, namely the Spalart–Allmaras (SA) one-equation turbulence model [37] and the k-ω Shear Stress Transport (SST) model of Menter [38], which are based on Boussinesq hypothesis and whose basic concepts are described briefly subsequently. In the present study, for the sake of simplicity and due to the constraint of computational resources for very high-speed flows, two-dimensional simulations have been performed and their results are analyzed in comparison with the experimental data of Schülein et al. [27]. The motivation of this study is to analyze the behavior of the SU2 open-source CFD code for high Mach numbers, where a knowledge gap still exists.

2.2.1. *The Spalart–Allmaras (SA) turbulence model.* A linear relationship between the turbulent Reynolds shear stresses and the mean velocity gradients is assumed in the Boussinesq eddy viscosity hypothesis, and the SA one-equation turbulence model neglects the contribution of the turbulent kinetic energy (TKE) k in the Reynolds stress tensor. Therefore, the turbulent Reynolds shear stress can be expressed by

$$\overline{u'v'} = -\nu_t \left(\frac{\partial U}{\partial y} + \frac{\partial V}{\partial x} \right), \tag{2.10}$$

where U and V are averaged velocity components in y and x spatial directions for two-dimensional flows. In the SA model, turbulent eddy viscosity is predicted through a new variable $\widehat{\nu}$ which is considered as a transport quantity in the model. This means that an additional transport equation for the scalar variable $\widehat{\nu}$ has to be solved and a closure function f_{v1} has to be computed in each iteration. The dynamic eddy viscosity coefficient μ_t of the SA semi-empirical turbulence model can be defined by

$$\mu_t = \rho \widehat{\nu} f_{v1}, \tag{2.11}$$

where the closure function can be expressed by

$$f_{v1} = \frac{\chi^3}{\chi^3 + c_{v1}^3}, \quad \text{where} \quad \chi = \frac{\widehat{\nu}}{\nu}. \tag{2.12}$$

For the additional transport equation $\widehat{\nu}$ to be solved in the SA model, the convective and viscous fluxes, as well as the source terms, can be expressed with vector notation as

$$\frac{\partial \widehat{\nu}}{\partial t} + (\mathbf{u} \cdot \nabla)\, \widehat{\nu} = c_{b1} \hat{S} \widehat{\nu} - c_{w1}\, f_w \left(\frac{\widehat{\nu}}{d_w} \right)^2 + \frac{1}{\sigma} \nabla \cdot \left[(\nu + \widehat{\nu})\, \nabla \widehat{\nu} \right] + \frac{c_{b2}}{\sigma} \left| \nabla \widehat{\nu} \right|^2, \tag{2.13}$$

where $\mathbf{u}$ is the velocity vector, d_w is the distance to the nearest surface, and the scalar quantity $\hat{S}$ in the production term can be formulated as

$$\hat{S} = \left|\underline{\underline{\Omega}}\right| + \frac{\widehat{\nu}}{\kappa^2 d_w^2} f_{v2}, \tag{2.14}$$

where $\left|\underline{\underline{\Omega}}\right|$ is the magnitude of the vorticity tensor. The SA model engineering turbulence model has three closure functions (f_{v1}, f_{v2} and f_w) and a total of eight closure coefficients (c_{b1}, c_{b2}, c_{w1}, c_{w2}, c_{w3}, c_{v1}, σ and κ) recorded in the references [35, 39]. For further details on the SA model, see [37].

2.2.2. *The k-ω Shear Stress Transport (SST) turbulence model.* The k-ω SST turbulence model of Menter [38] is a variant of two-equation k-ω models, which involves zonal or blending approach between the conventional k-ω and the k-ϵ model. In the near-wall region, the standard k-ω model is adopted while the k-ϵ model modified for high Reynolds number flows which is modeling the outer region of the boundary layer. In the k-ω SST model, the eddy viscosity μ_t is defined by

$$\mu_t = \frac{\rho a_1 k}{\max\left(a_1\omega, S\,F_2\right)}, \tag{2.15}$$

where $S = \sqrt{2S_{ij}S_{ij}}$ is the magnitude of the rate-of-strain tensor and F_2 is the second blending function. Two additional transport equations for the turbulent kinetic energy k and the specific rate of dissipation ω can be considered as

$$\rho\frac{\partial k}{\partial t} + \rho\left(\mathbf{u}\cdot\nabla\right)k = P_k - \rho\beta^\star\omega k + \nabla\cdot\left[\left(\mu + \sigma_k\mu_t\right)\nabla k\right], \tag{2.16}$$

$$\rho\frac{\partial \omega}{\partial t} + \rho\left(\mathbf{u}\cdot\nabla\right)\omega = \frac{\gamma}{\nu_t}P_\omega - \rho\beta_\star\omega^2 + \\ + \nabla\cdot\left[\left(\mu + \sigma_\omega\mu_t\right)\nabla\omega\right] + 2\rho\left(1 - F_1\right)\frac{\sigma_{\omega 2}}{\omega}\nabla k\cdot\nabla\omega, \tag{2.17}$$

where P_k and P_ω are the production terms of the k and ω transport equations. For turbulence modeling, the values of the constants used in transport Eqs. (2.16) and (2.17), and the relevant blending functions can be found in [38, 40].

2.3. **Numerical solution of the governing equations.** The SU2 code employs Finite Volume (FV) or Finite Element (FE) methods where the numerical flux terms are computed across the control volumes in a dual grid structure with a standard edge-based algorithm and a median-dual vertex based scheme. The governing equations can be considered in a semi-discretized form as

$$\int_{\Omega_i}\frac{\partial U_i}{\partial t}d\Omega + \sum_{j\in N(i)}\left(\tilde{F}^c_{ij} + \tilde{F}^v_{ij}\right)\Delta A_{ij} - S_U\left|\Omega_i\right| = \int_{\Omega_i}\frac{\partial U_i}{\partial t}d\Omega + R_i(U_i) = 0, \tag{2.18}$$

where U_i is the components of the vector of conservative variables, the convective/advective $\tilde{F}^c_{ij}$ and the viscous/diffusion $\tilde{F}^v_{ij}$ fluxes are predicted at the midpoint of each edge, and S_U represents any additional source terms. The convective terms can be discretized in either an upwind or central scheme while diffusion terms are approximated from the average of flow gradients at each node computed with either Green-Gauss or least-squares methods [34]. Source terms involved in the consideration

of other effects are reconstructed with piecewise constant relations. In the present numerical study, for approximating the convective flux terms, the flux-difference-splitting method of Roe is selected in the SU2 code as

$$\tilde{F}^c_{ij} = \tilde{F}\left(U_i, U_j\right) = \frac{1}{2}\left(\tilde{F}^c_i + \tilde{F}^c_j\right) \cdot \overrightarrow{n}_{ij} - \frac{1}{2}\widetilde{K}\left|\widetilde{\lambda}\right|\widetilde{K}^{-1}(U_i - U_j), \tag{2.19}$$

where $\widetilde{\lambda}$ is the local eigenvalue of the scheme. The numerical prediction of convective fluxes is first-order accurate in space while second-order accuracy is achieved with the Monotone Upstream-centered Scheme for Conservation Laws (MUSCL) approximation and slope limiters such as Venkatakrishnan [41] or Barth-Jespersen slope limiter, respectively. In terms of time integration, numerical computations can be performed with implicit and explicit schemes. Although explicit schemes such as Runge-Kutta are available in the SU2 code, the general setup for steady-state problems are carried out with the Euler implicit scheme. The SU2 code employs a local time-stepping approach when each cell moves forward at a different local time step, which is adopted in the numerical setup for faster convergence to steady-state solutions. On the other hand, unsteady problems can be configured with a dual time-stepping approach which can be first- or second-order accurate in time.

3. Simulation Setup

In this study, compressible Reynolds-averaged simulations have been carried out at three shock generator angles β of 6°, 10°, and 14° as specified in the experimental data of Schülein et al. [27]. The computational domains for each shock generator angle are created according to the coordinates of leading and trailing edges of shock generator as in the experiment of Schülein et al. [27], and two-dimensional (2D) investigations are carried out in this work. For each angle, three levels of meshes are created with the GMSH mesh generator software: coarse, medium and fine. Their description is presented in Table 1. The hybrid meshes are generated at the coarse grid level for each shock generator angle (see Figure 2). Structured quadrilateral cells are created in the boundary layer or near-wall regions of shock generator and the flat plate with y^+ of approximately 1.5 at the medium grid level. The remaining region is then populated with triangular cells, forming an unstructured hybrid meshing strategy. Grid clustering is observed towards the walls and within the region near the shock impingement point for achieving better accuracy in these regions, where $x \approx 0.330 - 0.350\ m$. The grid points in the inflation layer on the bottom wall are clustered towards the shock impingement location (with a growth rate of 1.1) for obtaining better accuracy in the simulations. In the SU2 configuration file, supersonic inlet and outlet boundary conditions are defined at the inlet and outlet sections, respectively. Isothermal no-slip walls are defined for the shock wave generator, flat plate and bottom surfaces while an Euler-type inviscid wall condition is prescribed for the section in front of the leading edge of shock wave generator. The freestream conditions used for the current study are summarized in Table 2.

Table 1. Description of two-dimensional hybrid meshes

Mesh	**Number of Cells**		
	$\beta = 6°$	$\beta = 10°$	$\beta = 14°$
Coarse ($y^+ = 5$)	105 955	106 089	104 495
Medium ($y^+ = 1.5$)	210 954	211 297	209 581
Fine ($y^+ = 0.5$)	405 483	407 584	406 157

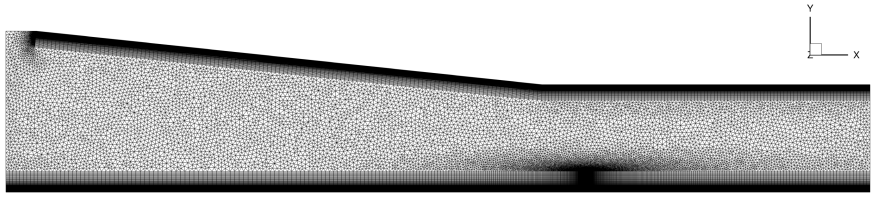

(a) Mesh for $\beta = 6°$.

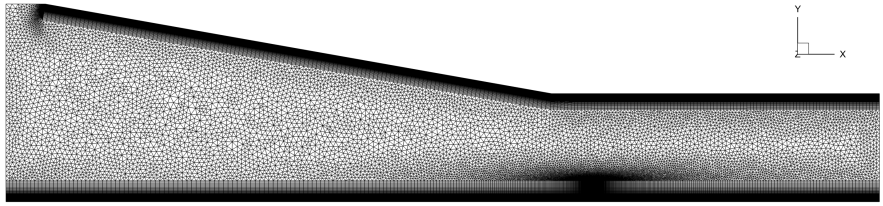

(b) Mesh for $\beta = 10°$.

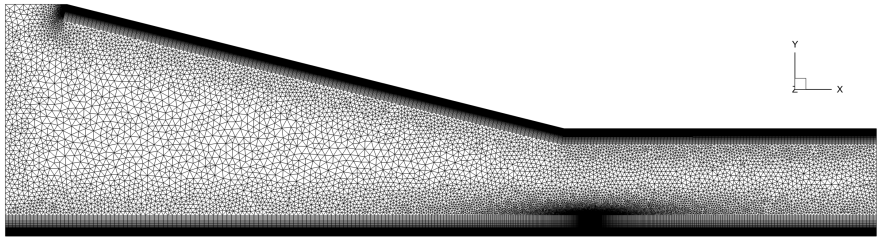

(c) Mesh for $\beta = 14°$.

Figure 2. 2D coarse meshes for various shock generator angles

Table 2. Freestream conditions

Flow Parameters	**Values**
Mach Number, Ma	5.0
Unit Reynolds Number, $Re_{1,\infty}$	$3.6736{\cdot}10^6$
Flow Velocity, U_∞	828.561 m/s
Static Pressure, P_∞	4006.88 Pa
Stagnation Pressure, $P_{0,\infty}$	$2.12{\cdot}10^6 Pa$
Static Temperature, T_∞	68.33 K
Stagnation Temperature, $T_{0,\infty}$	410 K
Density, ρ_∞	0.20428 kg/m^3
Dynamic Viscosity, μ_∞	$4.60741{\cdot}10^{-6}$ $N{\cdot}s/m^2$

3.1. **Grid convergence/mesh sensitivity study.** First of all, a grid convergence study is carried out, using Reynolds-averaged turbulence modeling approaches, at the shock generator angle of β=10° in a 2D impinging SWTBLI case for both SA and k-ω SST turbulence models. Steady-state solutions are computed with the Euler implicit scheme and a maximum Courant number of $CFL_{max} = 1.0$, where the skin friction coefficients C_f are monitored as a parameter for the Grid Convergence Index (GCI) [42, 43] calculations. At the location of $x = 0.376$ m, the GCI and the Richardson extrapolation values for skin friction coefficient $C_{f,h=0}$ are computed which are presented in Table 3 and plotted in Figure 3, where h is the normalized wall distance. The obtained computational results for the SA and the k-ω SST turbulence models demonstrate high levels of certainty (96.3% and 105.2%).

Table 3. Grid convergence study on the β=10° case

Turbulence Model	**Richardson Extrapolation** ($C_{f,h=0}$)	**GCI** (%)
SA	$5.682{\cdot}10^{-3}$	0.963%
k-ω SST	$4.730{\cdot}10^{-3}$	1.052%

In Figure 3, it can be seen that the skin friction coefficient obtained with the SA model is decreases with the grid refinement while the opposite is true for k-ω SST turbulence model. The experimental data for C_f at this particular location is within the range of 5.2–5.6 (x10^{-3}) in different experiments. Therefore, it is appropriate to conclude that the SA model predicts the C_f better than the k-ω SST turbulence model. In conclusion, grid convergence is achieved within the asymptotic range of convergence for both engineering turbulence models, thus the medium grid level is sufficient for further simulations of the two-dimensional impinging SWTBLI problem using a Reynolds-averaged turbulence modeling approach.

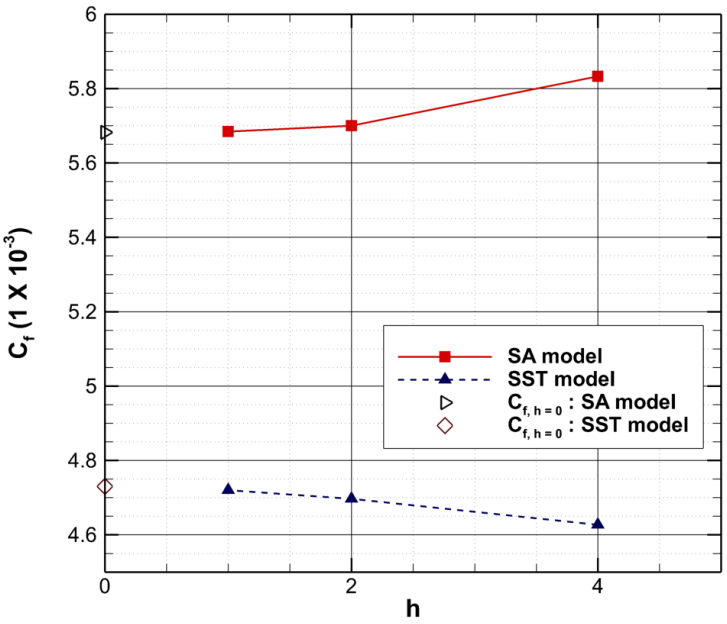

Figure 3. The obtained numerical values of the skin friction coefficient C_f and the Richardson extrapolation ($C_{f,h=0}$) for $\beta = 10°$

4. Results and Discussion

In this section, the compressible solver of the SU2 open-source code is utilized to analyze a Mach number 5 flow for a 2D impinging SWTBLI where different shock generator angles are investigated in comparison with the experimental data of Schülein et al. [27] and computational data by Leger and Poggie [31, 32]. The medium grid level is assumed to be appropriate for the validation of the results.

4.1. **Weak interaction case ($\beta = 6°$).** At $\beta = 6°$, a weak interaction event has been modeled and good agreement between CFD and experimental data is achieved for both the SA and k-ω SST turbulence models, including parameters such as skin friction, wall pressure and boundary layer profiles. In Figure 4, the skin friction coefficient C_f is plotted along the flat plate at β=6°. Previous experimental data and CFD results are also plotted as reference data for comparison. From the skin friction plot, as expected for a weak interaction case, no flow separation is predicted by all approaches, except for the k-ω SST model, where a very small separation region is observed. Better agreement is observed before the shock impingement region as compared to after it at the location $x = 0.350$ m. A drop in skin friction values is observed, as expected from [29] however, the location of such drop is different for each turbulence model. This drop in skin friction is predicted to be the earliest at around x≈0.330 m with the k-ω SST model, followed by the SA model at x≈0.336

m. A quantitatively smaller drop in skin friction is modeled with the SA model, as the one-equation model is more resistant to flow separation and change in wall shear stress.

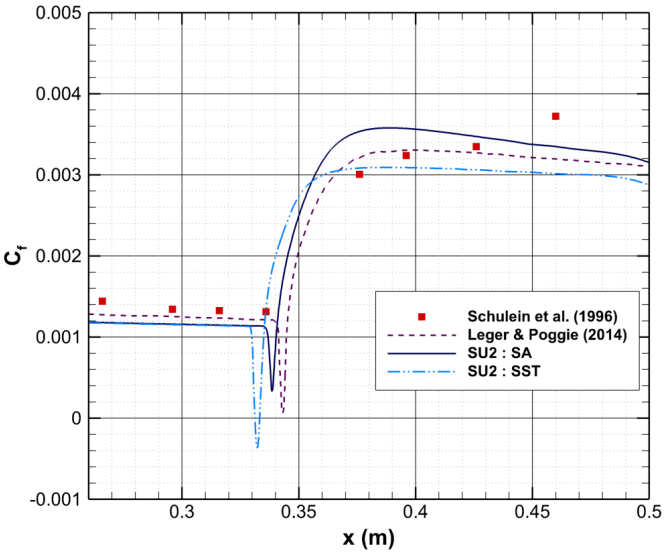

Figure 4. Skin friction distribution for $\beta = 6°$

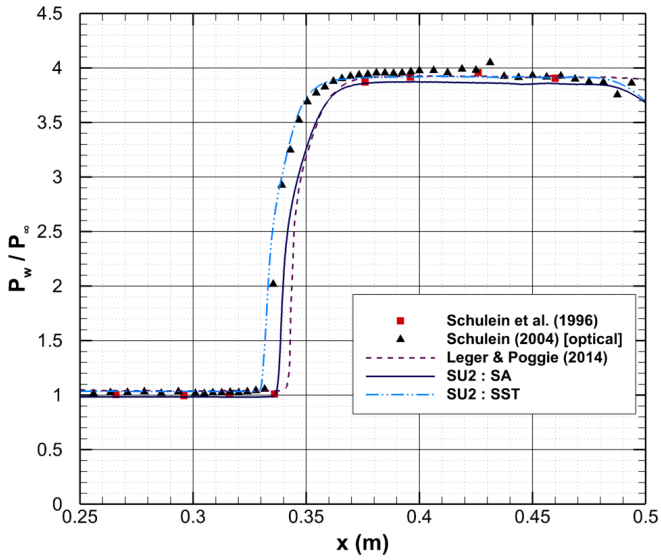

Figure 5. Wall pressure distribution for $\beta = 6°$

Figure 5 presents the wall pressure p_w distribution on the flat plate for β=6° where both turbulence models provide good agreement. A pressure jump is predicted in both cases; pressure change with the k-ω SST model (x $\approx$ 0.331 m) is very close to that of the experimental data of Schülein et al. [27]. Pressure rise is over-predicted by the SA model at the location of x $\approx$ 0.337 m whereas the Negative SA model (SA-neg) [29] predicts it at the location of x $\approx$ 0.342 m. Across the pressure jump near the interaction point, pressure ratios in all cases are estimated to be within the range, $p_3/p_1 \approx$ 3.865-3.913. This is close to the value reported by Brown [18] which is $p_3/p_1 \approx 3.762$. A pressure plateau region is observed after the interaction point, which shows close agreement with the experimental data of Schülein et al. [27].

In Figure 4, it can be observed that the C_f profile after the shock impingement is not in very close agreement with the experimental data. This could be due to the turbulence models being incapable of modeling the boundary layer recovery accurately despite this, the order of magnitude is captured reasonably well. On the other hand in Figure 5, close agreement can be seen between the pressure profiles before and after the shock impingement. This trend has been observed in all three angles of attacks and is visible in the plots below. At all three shock generator angles, dimensionless velocity profiles are investigated at different sections as reported by Schülein et al. [27]. All of the sections are located downstream of the interaction point where the compression waves are formed. For all sections, the typical trend of the viscous sublayer and the log-layer in a turbulent boundary layer is modeled by both turbulence models. However, within the log-layer, a close fit between experimental data and the law of the wall curve is not observed. Besides, the transition from log-layer to defect-layer at all sections predicted by both models with the use of the SU2 code is not closely matched with the measurements of Schülein et al. [27]. At a location furthest away from the interaction point, the best match between the k-ω SST dimensionless velocity profile and experimental data is shown in Figure 6. This is possibly due to the flow behavior at the location, which is least affected by compression waves and the shock formation. Discrepancies between experimental and CFD results can be due to the poor performance of the Reynolds-averaged turbulence modeling approach in accounting for non-equilibrium viscous behaviour and complex shock system.

At a fixed streamwise range, density contours computed with the SU2 code are further compared along with the Schlieren visualization by Schülein et al. [27] in Figure 7. The shock impingement point is predicted slightly earlier at x $\approx$ 0.330 m with the k-ω SST model while a later point is predicted at the location of x $\approx$ 0.336 m with the SA model. In comparison with reference data, earlier interaction between incidence shock and turbulent boundary layer is predicted by both turbulence models available in the SU2 compressible fluid flow solver. The SU2 code can predict general flow topology such as incidence and reflected shocks at $\beta = 6°$.

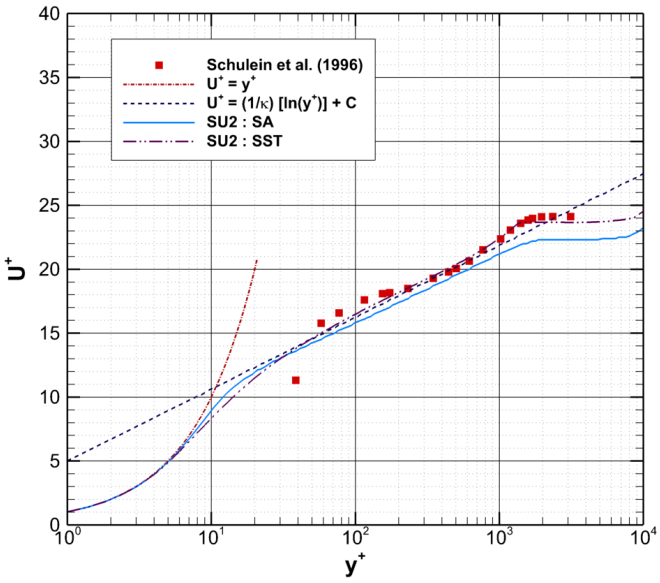

Figure 6. Dimensionless velocity profile for $\beta = 6°$ at x = 0.460 m

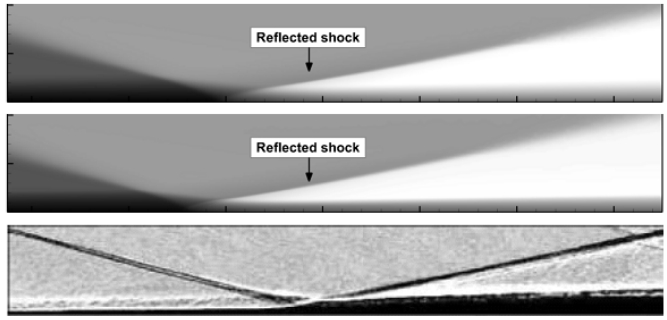

Figure 7. Density contours in comparison with the Schlieren visualization for $\beta = 6°$ (from top to bottom: SU2 SA model, SU2 k-ω SST model and the experiment of Schülein et al. [27])

4.2. **Incipient interaction case ($\beta = 10°$).** Figure 8 presents the skin friction coefficients C_f as computed at $\beta = 10°$ in comparison with the experimental data of Schülein et al. [27], and CFD data taken from the NASA Wind-US code and from Leger and Poggie [31, 32]. The results are similar for different approaches, except for the interaction region in the range of 0.321 $m < x < 0.350$ m. Downstream of the location x ≈ 0.350 m, the skin friction plateau level is underpredicted by CFD simulations of the Wind-US, US3D and SU2 codes. The SA model of the SU2 code

shows better agreement with the experimental data within this region. However, it is possible that the uncertainties associated with the experimental data of Schülein et al. [27] cause such discrepancies. In terms of the slope associated with the rise in the skin friction after the shock interaction, the trend predicted by the SU2 code is closely fitted with that of experimental data (see Figure 8). Overall, the skin friction distribution over the flat plate is well modeled by the SU2 compressible fluid flow solver, except for the shock interaction and separation zones.

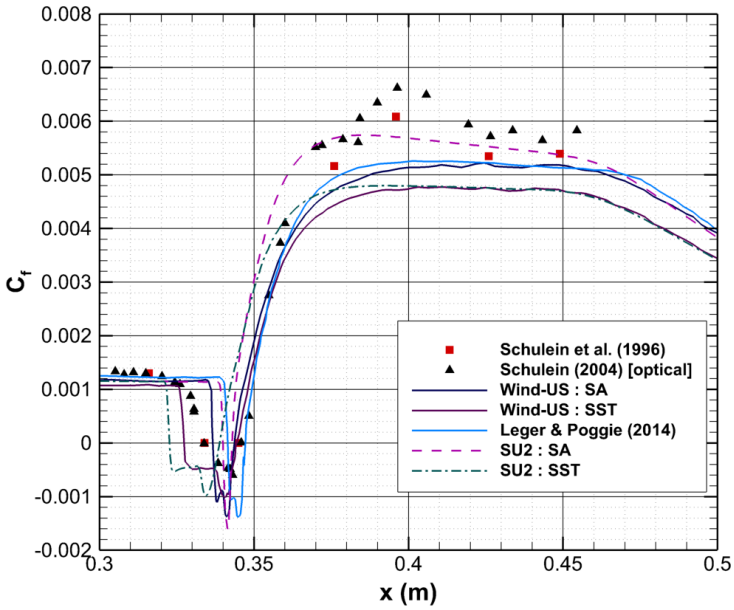

Figure 8. Skin friction distribution for $\beta = 10°$

Within the shock interaction region, flow separation is predicted with the SA and the k-ω SST turbulence models using the SU2 code. Based on the results from the Wind-US and the SU2 codes, an earlier flow separation is observed in the case of the k-ω SST model as compared to that of the SA model. As experimental measurements lead to a flow separation at x $\approx$ 0.334 m, the Mach number 5 flow over the flat plate separates at x $\approx$ 0.322 m in the case of the k-ω SST model while delayed flow separation is predicted at x $\approx$ 0.340 m with the SA model. In comparison with the experimental data of Schülein et al. [27] at x $\approx$ 0.345 m, reattachment points occur earlier in the case of the k-ω SST model at x $\approx$ 0.339 $m$and at around x $\approx$ 0.343 m with the SA model. Separation bubble size is predicted by the SA model to be about one-third of the experimental value, which is significantly smaller than the value predicted with the k-ω SST model (50% greater in size in comparison with the experimental data). The results are consistent with those reported in the literature [27], where the flow separation is underestimated by the SA model and overestimated with the k-ω SST

model. The discrepancies between these results are possibly due to the limitations of the Reynolds-averaged modeling in flows with complex shock formation and thermo-chemical effects.

Wall pressure distribution p_w at $\beta = 10°$ is plotted in Figure 9. Close agreement is obtained with both turbulence models investigated here for the wall pressure distribution. Pressure rise is predicted to be the earliest with the k-ω SST model at x $\approx 0.321\ m$, followed by the SA model and the SA-neg model, which computes a later pressure jump at x $\approx 0.340\ m$ than in the experiments at x $\approx 0.332\ m$. The Pressure plateau level after the interaction point is computed to be around $p_3/p_1 \approx 7.65$-7.71, which is similar to that reported by Brown [18], $p_3/p_1 \approx 7.63$. The pressure distributions are captured very well in comparison with experimental data, and it can be concluded that the Reynolds-averaged modeling approach in the SU2 code is capable of calculating accurate wall pressure distribution p_w for a moderate interaction event involving an impinging SWTBLI on a flat plate at Mach number of 5.

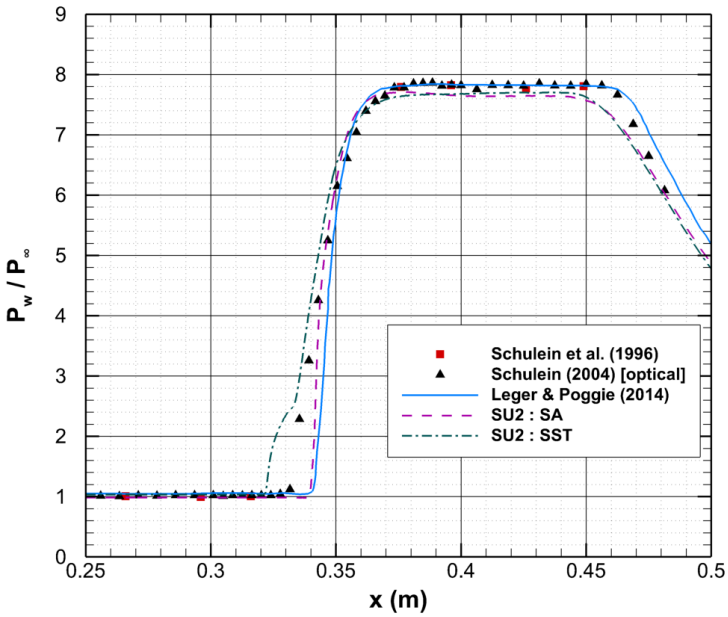

Figure 9. Wall pressure distribution for $\beta = 10°$

The dimensionless velocity profile for $\beta = 10°$ is plotted in Figure 10. Within the viscous sublayer, the curves modeled by both turbulence models investigated here are in agreement with the profile of $U^+ = y^+$. The CFD results as computed by the SU2 code are also closely matched with the law of the wall at all sections. However, experimental values are observed to be slightly deviated from the law of the wall. The main discrepancy between experimental and the CFD dimensionless velocity profiles is found within the defect-layer. In this region, the k-ω SST model is deduced to be

superior to the SA model in predicting the flow behavior of SWTBLI case at Mach number of 5. Dimensionless velocity profiles of the k-ω SST model are quite similar to those obtained in the experiments at all sections, with only a slight difference in the transition from the log-layer to the defect-layer.

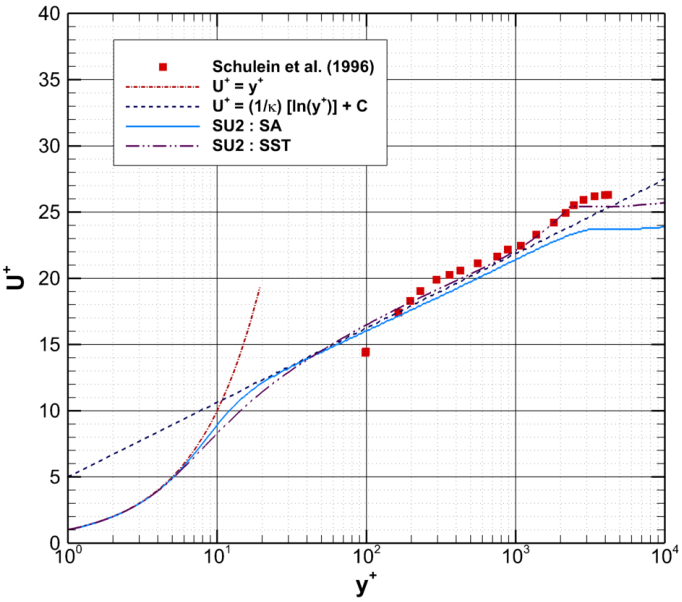

Figure 10. Dimensionless velocity profile for $\beta = 10°$ at x = 0.460 m

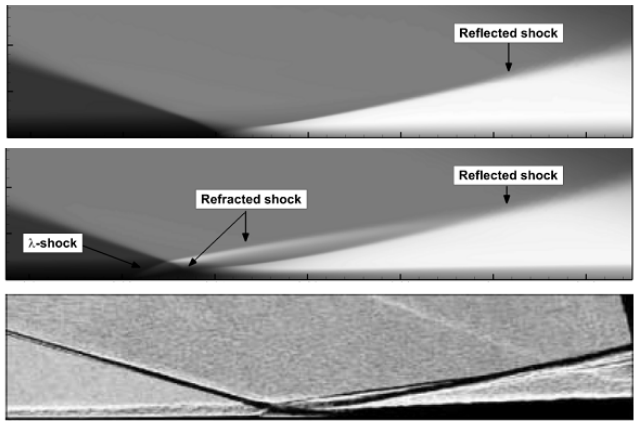

Figure 11. Density contours in comparison with the Schlieren visualization for $\beta = 10°$ (from top to bottom: SU2 SA model, SU2 k-ω SST model and the experiment of Schülein et al. [27])

In Figure 11, the density fields computed by the SU2 solver are generated compared to the Schlieren images from the experiment [27]. The formation of two refracted shocks from the incidence shock and the λ-shock upstream of the separation region can be observed from the density contour of the k-ω SST model. Two refracted shocks are created when expansion waves are formed as oblique shock penetrates the separation bubble. Reflected shock is then formed from the merging of both refracted shocks and compression waves downstream of the interaction point. The type of shocks observed in the Schlieren images are consistent with that predicted with the k-ω SST model. Only reflected shock is observed in the density field of the SA model due to its small separation bubble size. In addition, the separation region is predicted to begin earlier with the k-ω SST model, as it is known to overestimate separation size.

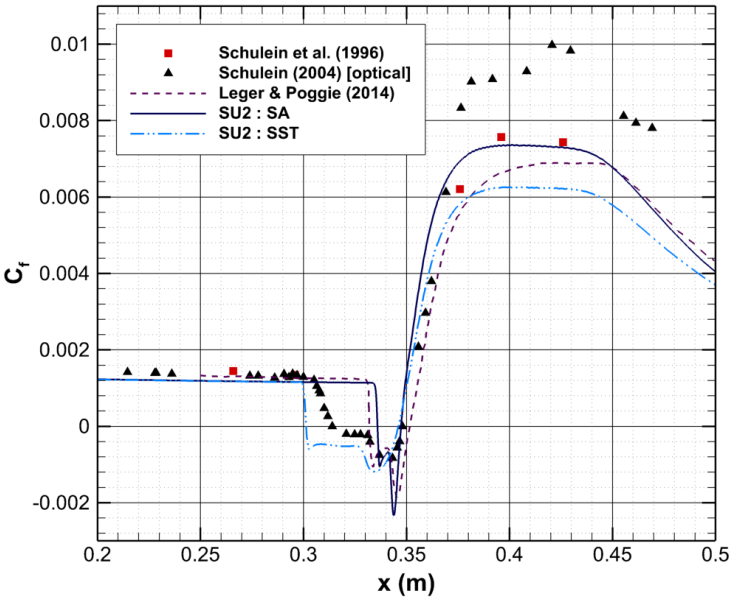

Figure 12. Skin friction distribution for $\beta = 14°$

4.3. **Strong interaction case ($\beta = 14°$).** A strong interaction case at $\beta = 14°$ is investigated in this subsection. The discrepancy between experimental and computational results is found to be the most significant at this angle. Figure 12 presents the skin friction coefficients C_f over the flat plate, plotted with reference to experimental and CFD data taken from the literature [27, 31, 32]. In this case, the extent of the shock interaction is much greater than at $\beta = 10°$, which spans a range of $0.300\ m < x < 0.350\ m$. As the interaction strength is the strongest at $\beta = 14°$, the discrepancies between experimental and computational results are more significant. Downstream of the interaction region, skin friction values are underestimated with all CFD approaches employed here. The SA model of the SU2 code predicts the skin

friction plateau level closest to the experimental data of Schülein et al. [27]. The skin friction is observed to increase at the same rate for both experimental and CFD curves. Separation points are estimated at x $\approx$ 0.336 m and x $\approx$ 0.301 m with the SA and the k-ω SST models, respectively. In comparison with the experimental data of Schülein et al. [27] at x $\approx$ 0.314 m, early flow separation is predicted with the k-ω SST model, while separation predicted with the SA model is delayed. Close agreement is obtained by both turbulence models for reattachment points at x $\approx$ 0.347 m. Separation and reattachment points predicted by the SA and the SA-neg model are observed to be similar. The separation bubble observed in the SA model is one-third that of the experiment, while separation bubble size predicted with the k-ω SST model is about 40% larger than the experimental data in [27]. This could be due to the nature of the SA model in underestimating wall shear stress, while excessive turbulence kinetic energy might be modeled with the k-ω SST model in this case.

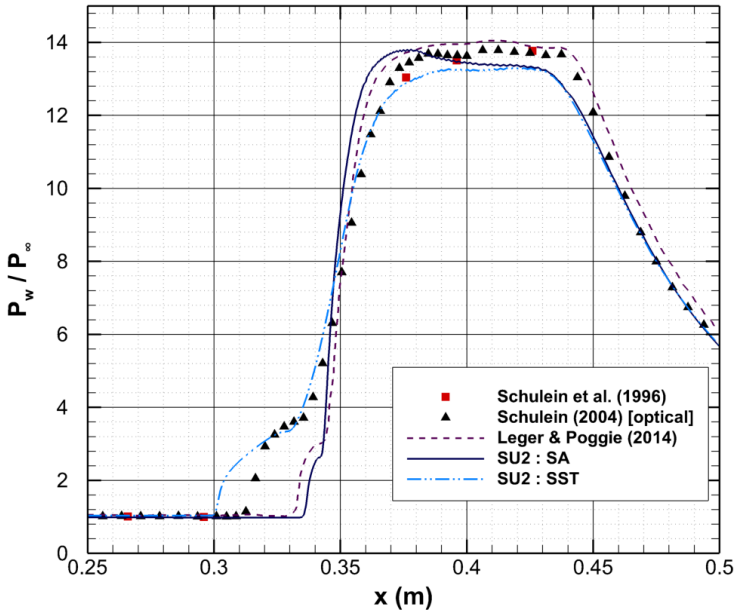

Figure 13. Wall pressure distribution for $\beta = 14°$

In Figure 13, the wall pressure distribution p_w across the flat plate at $\beta = 14°$ is plotted along with the experimental data [27]. In this case, greater discrepancy in data is observed downstream of the shock interaction region due to the strong interaction strength. Wall pressure values are slightly underestimated post-interaction by both turbulence models. Initial pressure jumps are estimated at x $\approx$ 0.335 m and x $\approx$ 0.300 m with the SA and the k-ω SST models, while x $\approx$ 0.313 m is measured in the experiment. A second inflection point at $p_w/p_\infty \approx$ 3.71-4.02 is observed with the k-ω SST model at x $\approx$ 0.335 m, which coincides with the experimental data. In

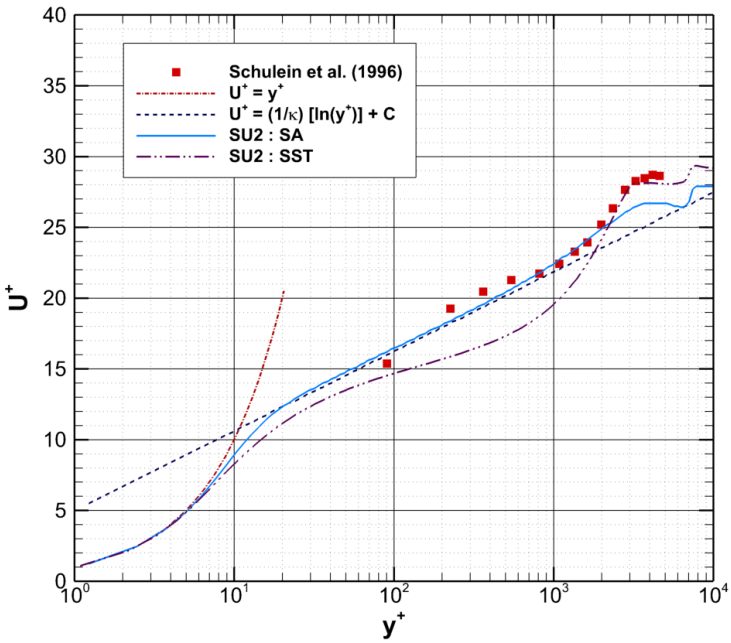

Figure 14. Dimensionless velocity profile for $\beta = 14°$ at x = 0.460 m

contrast, a second inflection point is predicted at a lower pressure, $p_w/p_\infty \approx 2.71$, x ≈ 0.343 m. Therefore, better agreement is achieved by the k-ω SST model as compared to the SA model. The pressure plateau level downstream of interaction region at $\beta = 14°$ is computed about $p_3/p_1 \approx$ 13.25-13.44, while it is reported by Brown [18] as $p_3/p_1 \approx 13.62$. As compared to the results at $\beta = 10°$, the difference in pressure plateau levels is slightly greater at $\beta = 14°$. This is due to poor performance of the typical Reynolds-averaged modeling in simulations involving significant flow separation and pressure change across the shock interaction zone.

In Figure 14, the velocity profile of the k-ω SST model is observed to deviate from the law of the wall; however, the transition predicted from the log-layer to the defect-layer is consistent with experimental measurements [27]. The velocity profile of the SA model follows the law of the wall, although it fails to predict correctly the defect-layer at this location. In the sections further downstream of the shock impingement point, modeled boundary layer profiles are fairly close to the experimental data with differences for the defect-layer. It can be concluded that the transition from the log-layer to the defect-layer is poorly estimated by both turbulence models in a strong interaction case. This is due to the assumptions made in the turbulence models that simplify flow problems based on subsonic benchmark test cases which do not include the shock interaction. In future studies, the role of coefficients and functions in URANS modeling can also be investigated.

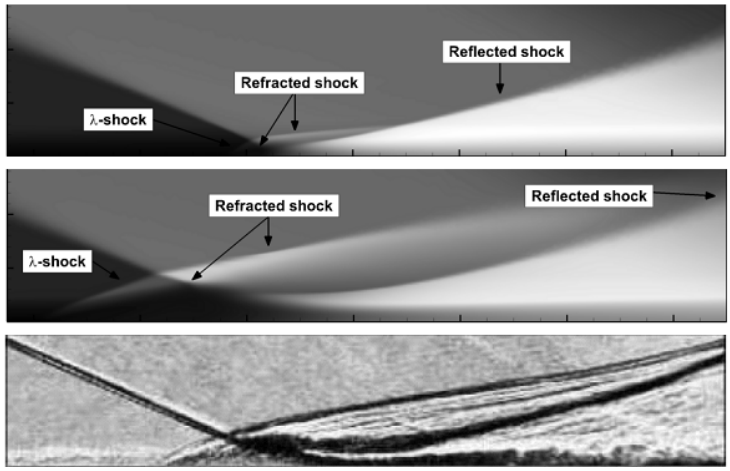

Figure 15. Density contours in comparison with the Schlieren visualization for $\beta = 14°$ (from top to bottom: SU2 SA model, SU2 k-ω SST model and the experiment of Schülein et al. [27])

The simulated density fields are plotted with the Schlieren images in Figure 15. Flow separation is predicted to be earlier in the k-ω SST model, while it is delayed in the SA model. Separation size in the k-ω SST is around 50% larger than in the experiment [27], while the SA model gives a separation region which is half of that. Two refracted shocks observed with the k-ω SST model are more distinct than with the SA model, where weaker shocks are formed instead. In addition, expansion waves spanning from one of the refracted shock are clearly shown in the density contour of the k-ω SST model. The density field of the k-ω SST model closely resembles the structure of the shock system observed in the experiment, including the angles of the λ-shock foot and refracted shocks formed at the triple point. It can be concluded that the SA model is unable to predict the degree of flow separation and SWTBLI in a strong interaction case, whereas the k-ω SST model tends to overestimate the separation size and produce stronger shocks in the flow field.

5. Conclusions and Future Work

The open source SU2 CFD code has been evaluated in this study at a Mach number of 5 where an impinging SWTBLI on a flat plate is investigated and compared to the experimental data of Schülein et al. [27]. The results presented demonstrate the strengths and weakness of the SU2 code for the investigation of such a high Mach number flow. For the 2D impinging SWTBLI case, the SA and the k-ω SST turbulence models are used to compute the flow field. These turbulence modeling approaches were validated against the experimental data for parameters such as skin friction, wall pressure distribution and boundary layer profiles. The discrepancies between computational and experimental data become more significant with higher

shock generator angles β, which indicates increasing shock interaction strength. It can also be observed that neither turbulence model was capable of capturing the boundary layer recovery after the shock impingement, which resulted in discrepancy in the results for C_f. However, pressure profiles were captured very well for all three angles. Both turbulence models are concluded to be less reliable within the shock interaction and separation regions. This is due to the inherent working principle of Reynolds-averaged modeling, which does not resolve small and large scale eddies in the flow field. At all β angles, earlier flow separation is predicted with the k-ω SST model, while the flow field is less sensitive to separation for SU2 simulations with the SA model. The SA model is deduced to be better in the prediction of reattachment points, while the complex shock system at higher β angles is better computed by the k-ω SST model. A larger separation size and stronger shock formation are predicted with the k-ω SST model as compared to the SA model. With both turbulence models Wall pressure distributions are captured well within the experimental values. Velocity profile results are plotted to be less accurate in comparison with experimental data at higher β values. Although the SA model predicts better velocity curves at some sections, both turbulence models are unable to solve the SWTBLI case with high reliability and accuracy for a strong interaction case. Based on the evaluation of the SU2 open-source code for the Schülein et al. [27] case, the compressible solver is found to be suitable for a preliminary or rough assessment of high Mach flows with SWTBLI phenomenon in the industry. However, for research purposes, more sophisticated three-dimensional unsteady turbulence modeling approaches such as LES and DES should be included in the SU2 solver. Moreover, other cases with high Mach number flows and SWTBLI such as compression ramps or double fins can be taken as further validation steps for the current SU2 solver.

Acknowledgement. This research work was financially supported by the Centre for Computational Engineering Sciences at Cranfield University under the project code EEB6001R. All the simulations are carried out on the Crescent and the Delta High Performance Computing (HPC) facility and authors would like to acknowledge Dr. Michael Knaggs for his continuous support. Authors would also like to say thanks to Dr. Erich Schülein for allowing them to use figures from his research for the purpose of flow comparison. For the purpose of open access, the authors have applied a Creative Commons Attribution (CC BY) licence to any author accepted manuscript version arising. The authors declare no conflict of interest.

References

1. Cecere, D., Ingenito, A., Romagnosi, L., Bruno, C. and Giacomazzi, E.: Shock/boundary layer/heat release interaction in the HyShot II scramjet combustor. In *Proceedings of 46th AIAA Joint Propulsion Conference & Exhibit*, Nashville, TN, USA, 2010. DOI: 10.2514/6.2010-7066
2. Segal, C.: In The Scramjet Engine: Processes and Characteristics. *Cambridge University Press*, 2009, ISBN 9780511627019. DOI: 10.1017/CBO9780511627019
3. Schetz, J. A., and Billig, F. S.: Studies of scramjet flowfields. In *Proceedings of 23rd AIAA Joint Propulsion Conference*, San Diego, California, USA, 1987. DOI: 10.2514/6.1987-2161

4. Smart, M. K., Hass, N. E. and Paull, A.: Flight data analysis of the HyShot 2 scramjet flight experiment. *AIAA Journal*, **44**(10), (2006), 2366–2375. DOI: 10.2514/1.20661

5. Mass, N. E., Smart, M. K. and Paull, A.: Flight data analysis of HyShot 2. In *A Collection of Technical Papers–13th AIAA/CIRA International Space Planes and Hypersonic Systems and Technologies Conference*, Vol. 2, 2005. DOI: 10.2514/6.2005-3354

6. Laurence, S., Schramm, J. M., Karl, S. and Hannemann, K.: An experimental investigation of steady and unsteady combustion phenomena in the HyShot II combustor. In *Proceedings of 17th AIAA International Space Planes and Hypersonic Systems and Technologies Conference*, 2011, p. 14. DOI: 10.2514/6.2011-2310

7. Karl, S., Hannemann, K., Mack, A. and Steelant, J.: CFD analysis of the HyShot II scramjet experiments in the HEG shock tunnel. In *Proceedings of 15th AIAA International Space Planes and Hypersonic Systems and Technologies Conference*, American Institute of Aeronautics and Astronautics, USA, 2008, p. 16. DOI: 10.2514/6.2008-2548

8. Berglund, M. and Fureby, C.: LES of supersonic combustion in a scramjet engine model. *Proceedings of the Combustion Institute*, **31**(2), (2007), 2497–2504. DOI: 10.1016/j.proci.2006.07.074

9. Fureby, C., Chapuis, M., Fedina, E. and Karl, S.: CFD analysis of the HyShot II scramjet combustor. *Proceedings of the Combustion Institute*, **33**(2), (2011), 2399–2405. DOI: 10.1016/j.proci.2010.07.055

10. Chapuis, M., Fedina, E., Fureby, C., Hannemann, K., Karl, S. and Schramm, J. M.: A computational study of the HyShot II combustor performance. *Proceedings of the Combustion Institute*, **34**(2), (2013), 2101–2109. DOI: 10.1016/j.proci.2012.07.014

11. You, Y., Luedeke, H. and Hannemann, K.: Injection and mixing in a scramjet combustor: DES and RANS studies. *Proceedings of the Combustion Institute*, **34**(2), (2013), 2083–2092. DOI: 10.1016/j.proci.2012.10.001

12. Karl, S., Laurence, S., Schramm, J. M. and Hannemann, K.: CFD analysis of unsteady combustion phenomena in the HyShot-II scramjet configuration. In *Proceedings of 18th AIAA/3AF International Space Planes and Hypersonic Systems and Technologies Conference*, American Institute of Aeronautics and Astronautics, USA, 2012, p. 13. DOI: 10.2514/6.2012-5912

13. Wen, C. Y., Chen, Y. S. and Chen, J. Y.: Numerical simulation of complex internal viscous flow in the HyShot-II scramjet model. In *Proceedings of 17th AIAA International Space Planes and Hypersonic Systems and Technologies Conference*, American Institute of Aeronautics and Astronautics, USA, 2011, p. 9. DOI: 10.2514/6.2011-2382

14. Pecnik, R., Terrapon, V. E., Ham, F., Iaccarino, G. and Pitsch, H.: Reynolds–Averaged Navier–Stokes simulations of the HyShot II scramjet. *AIAA Journal*, **50**(8), (2012), 1717–1732. DOI: 10.2514/1.J051473

15. Ben-Yakar, A; Mungal, G. and Hanson, R.: Time evolution and mixing characteristics of hydrogen and ethylene transverse jets in supersonic crossflows. *Physics of Fluids*, **18**(2), (2006), 315–323. DOI: 10.1063/1.2139684

16. Rana, Z. A., Thornber, B. and Drikakis, D.: Transverse jet injection into a supersonic turbulent cross-flow. *Physics of Fluids*, **23**(4), (2011), 046103. DOI: 10.1063/1.3570692

17. Rana, Z. A., Thornber, B. and Drikakis, D.: Dynamics of sonic hydrogen injection and mixing inside scramjet combustor. *Engineering Applications of Computational Fluid Mechanics*, **7**(1), (2013), 13–39. DOI: 10.1080/19942060.2013.11015451

18. Brown, J.: Shock wave impingement on boundary layers at hypersonic speeds: computational analysis and uncertainty. In *Proceedings of 42nd AIAA Thermophysics Conference*, American Institute of Aeronautics and Astronautics, USA, 2011, p. 63. DOI: 10.2514/6.2011-3143

19. Gaitonde, D. V.: Progress in shock wave/boundary layer interactions. *Progress in Aerospace Sciences*, **72**, (2015), 80–99. DOI: 10.1016/j.paerosci.2014.09.002

20. Titchener, N. and Babinsky, H.: Shock wave/boundary-layer interaction control using a combination of vortex generators and bleed. *AIAA Journal*, **51**(5), (2013), 1221–1233. DOI: 10.2514/1.J052079

21. Dolling, D. S.: Fifty years of shock-wave/boundary-layer interaction research: What next? *AIAA Journal*, **39**(8), (2001), 1517–1531. DOI: 10.2514/2.1476

22. Fang, J., Yao, Y., Zheltovodov, A., Li, Z. and Lu, L.: Direct numerical simulation of supersonic turbulent flows around a tandem expansion-compression corner. *Physics of Fluids*, **27**(12), (2015), 125104. DOI: 10.1063/1.4936576

23. Knight, D., Yan, H., Panaras, A. and Zheltovodov, A.: Advances in CFD prediction of shock wave turbulent boundary layer interactions. *Progress in Aerospace Sciences*, **39**(2–3), (2003), 121–184. DOI: 10.1016/S0376-0421(02)00069-6

24. Dussauge, J. - P.; Dupont, P. and Debiève, J. - F.: Unsteadiness in shock wave boundary layer interactions with separation. *Aerospace Science and Technology*, **10**(2), (2006), 85–91. DOI: 10.1016/j.ast.2005.09.006

25. Pirozzoli, S. and Bernardini, M.: Direct numerical simulation database for impinging shock wave/turbulent boundary-layer interaction. *AIAA Journal*, **49**(6), (2011), 1307–1312. DOI: 10.2514/1.J050901

26. Diop, M., Piponniau, S., and Pierre, D.: On the length and time scales of a laminar shock wave boundary layer interaction. In *Proceedings of 54th AIAA Aerospace Sciences Meeting*, American Institute of Aeronautics and Astronautics, USA, 2016, p. 18. DOI: 10.2514/6.2016-0073

27. Schülein, E., Krogmann, P. and Stanewsky, E.: Documentation of two-dimensional impinging shock/turbulent boundary layer interaction flow. *DLR report 223-96 A49, 69S*, 1996. DOI: https://elib.dlr.de/37537/

28. Settles, G. S. and Dodson, L. J.: Supersonic and hypersonic shock/boundary-layer interaction database. *AIAA Journal*, **32**(7), (1994), 1377–1383. DOI: 10.2514/3.12205

29. Settles, G. S. and Dodson, L. J.: Hypersonic shock/boundary-layer interaction database. In *Proceedings of 22nd Fluid Dynamics, Plasma Dynamics and Lasers Conference*, Honolulu, HI, USA, 1991. DOI: 10.2514/6.1991-1763

30. Fedorova, N. N. and Fedorchenko, I. A.: Computations of interaction of an incident oblique shock wave with a turbulent boundary layer on a flat plate. *Journal of Applied Mechanics and Technical Physics*, **45**(3), (2004), 358–366. DOI: 10.1023/B:JAMT.0000025017.49191.14

31. Leger, T. J. and Poggie, J.: Computational analysis of shock wave turbulent boundary layer interaction. In *Proceedings of 52nd Aerospace Sciences Meeting*, American Institute of Aeronautics and Astronautics, USA, 2014. DOI: 10.2514/6.2014-0951

32. Leger, T., Bisek, N. and Poggie, J.: Computations of turbulent flow over a sharp fin at Mach 5. *Journal of Thermophysics and Heat Transfer*, **30**(2), (2016), 394–402. DOI: 10.2514/1.T4698

33. Fang, J., Yao, Y., Zheltovodov, A. A. and Lu, L.: Numerical simulations of two-dimensional and three-dimensional shock wave/turbulent boundary layer interactions. In *ICMAR 2014*, Novosibirsk, Russia, 2014. DOI: http://eprints.uwe.ac.uk/24250

34. Palacios, F., Economon, T. D., Aranake, A., Copeland, S. R., Lonkar, A., Lukaczyk, T., Manosalvas, D., Naik, K., Padron, S., Tracey, B., Variyar, A. and Alonso, J.: Stanford University Unstructured (SU2): analysis and design technology for turbulent flows. In *Proceedings of 52nd Aerospace Sciences Meeting, AIAA SciTech Forum*, American Institute of Aeronautics and Astronautics, USA, 2014-0243. DOI: 10.2514/6.2014-0243

35. Palacios, F., Alonso, J., Colonno, M., Aranake, A., Campos, A., Copeland, S., Economon, T., Lonkar, A., Lukaczyk, T. and Taylor, T.: Stanford University Unstructured (SU2): An open source integrated computational environment for multiphysics simulation and design. In *Proceedings of 51st AIAA Aerospace Sciences Meeting including the New Horizons Forum and Aerospace Exposition, Aerospace Sciences Meetings*, American Institute of Aeronautics and Astronautics, USA, 2013. DOI: 10.2514/6.2013-287

36. Economon, T., Mudigere, D., Bansal, G., Heinecke, A., Palacios, F., Park, J., Smelyanskiy, M., Alonso, J. and Dubey, P.: Performance optimizations for scalable implicit RANS calculations with SU2. *Computers & Fluids*, **129**, (2016), 146–158. DOI: 10.1016/j.compfluid.2016.02.003

37. Spalart, P. and Allmaras, S.: A one-equation turbulence model for aerodynamic flows. In *Proceedings of 30th Aerospace Sciences Meeting and Exhibit, Aerospace Sciences Meetings*, Reno, NV, USA, 1992. DOI: 10.2514/6.1992-439

38. Menter, F. R.: Two-equation eddy-viscosity turbulence models for engineering applications. *AIAA Journal*, **32**(8), (1994), 1598–1605. DOI: 10.2514/3.12149

39. Chorin, A. J.: A numerical method for solving incompressible viscous flow problems. *Journal of Computational Physics*, **135**(2), (1997), 118–125. DOI: 10.1006/jcph.1997.5716

40. Wilcox, D. C.: *Turbulence Modeling for CFD*. DCW industries La Canada, CA, 1998, ISBN-10: 1928729088.

41. Venkatakrishnan, V.: Convergence to steady state solutions of the euler equations on unstructured grids with limiters. *Journal of Computational Physics*, **118**(1), (1995), 120–130. DOI: 10.1006/jcph.1995.1084

42. Roache, P. J.: *Verification and Validation in Computational Science and Engineering*. Hermosa Publishers, Albuquerque, New Mexico, 1998, ISBN-10: 0913478083.

43. AIAA: Guide for the Verification and Validation of Computational Fluid Dynamics Simulations. *AIAA G-077-1998*, 1998, eISBN: 978-1-56347-285-5. DOI: 10.2514/4.472855

44. Schülein, E.: Skin friction and heat flux measurements in shock/boundary layer interaction flows. *AIAA Journal*, **44**(8), (2006), 1732–1741. DOI: 10.2514/1.15110

Notes for Contributors
to the Journal of Computational and Applied Mechanics

Aims and scope. The aim of the journal is to publish research papers on theoretical and applied mechanics. Special emphasis is given to articles on computational mechanics, continuum mechanics (mechanics of solid bodies, fluid mechanics, heat and mass transfer) and dynamics. Review papers on a research field and materials effective for teaching can also be accepted and are published as review papers or classroom notes. Papers devoted to mathematical problems relevant to mechanics will also be considered.
Frequency of the journal. Two issues a year (approximately 80 pages per issue).

Submission of Manuscripts. Submission of a manuscript implies that the paper has not been published, nor is being considered for publication elsewhere. Papers should be written in standard grammatical English. The manuscript is to be submitted in electronic, preferably in pdf, format. The text is to be 130 mm wide and 190 mm long and the main text should be typeset in 10pt CMR fonts. Though the length of a paper is not prescribed, authors are encouraged to write concisely. However, short communications or discussions on papers published in the journal must not be longer than 2 pages. Each manuscript should be provided with an English Abstract of about 50–70 words, reporting concisely on the objective and results of the paper. The Abstract is followed by the Mathematical Subject Classification – in case the author (or authors) give the classification codes – then the keywords (no more than five). References should be grouped at the end of the paper in numerical order of appearance. Author's name(s) and initials, paper titles, journal name, volume, issue, year and page numbers should be given for all journals referenced.
The journal prefers the submission of manuscripts in LaTeX. Authors should select the $\mathcal{AMS}$-LaTeX article class and are not recommended to define their own LaTeX commands. Visit our home page for further details concerning how to edit your paper.
Manuscripts should be sent to either to the Editorial Office of JCAM:

jcam@uni-miskolc.hu

or directly to an editor: László Baranyi

laszlo.baranyi@uni-miskolc.hu (fluid mechanics and heat transfer)

or BalázsTóth

balazs.toth@uni-miskolc.hu (solid mechanics).

The eventual supply of an accepted for publication paper in its final camera-ready form will ensure more rapid publication. Format requirements are provided by the home page of the journal from which sample LaTeX files can be downloaded:

`http://www.mech.uni-miskolc.hu/jcam/`

These sample files can also be obtained directly (via e-mail) from Balázs Tóth.

One issue of the journal will be provided free of charge and mailed to the correspondent author. Since JCAM is an open access journal each paper can be downloaded freely from the homepage of the journal.

The Journal of Computational and Applied Mechanics is abstracted in Zentralblatt für Mathematik and in the Russian Referativnij Zhurnal.

Secretariat of the Vice-Rector for Research and International Relations, University of Miskolc
Responsible for publication: Prof. Dr. Zita Horváth, rector
Published by the Miskolc University Press under the leadership of Attila Szendi
Responsible for duplication: Works manager Erzsébet Pásztor
Number of copies printed: 75
Put to the Press on November 20, 2022
Number of permission: MERT.2022-325.ME.
ISSN 2732–0189 (Online)
ISSN 1586–2070 (Print)

A Short History of the Publications of the University of Miskolc

The University of Miskolc (Hungary) is an important center of research in Central Europe. Its parent university was founded by the Empress Maria Teresia in Selmecbánya (today Banska Štiavnica, Slovakia) in 1735. After the first World War the legal predecessor of the University of Miskolc moved to Sopron (Hungary) where, in 1929, it started the series of university publications with the title *Publications of the Mining and Metallurgical Division of the Hungarian Academy of Mining and Forestry Engineering* (Volumes I.-VI.). From 1934 to 1947 the Institution had the name Faculty of Mining, Metallurgical and Forestry Engineering of the József Nádor University of Technology and Economic Sciences at Sopron. Accordingly, the publications were given the title *Publications of the Mining and Metallurgical Engineering Division* (Volumes VII.-XVI.). For the last volume before 1950 – due to a further change in the name of the Institution – *Technical University, Faculties of Mining, Metallurgical and Forestry Engineering, Publications of the Mining and Metallurgical Divisions* was the title.

For some years after 1950 the Publications were temporarily suspended.

After the foundation of the Mechanical Engineering Faculty in Miskolc in 1949 and the movement of the Sopron Mining and Metallurgical Faculties to Miskolc, the Publications restarted with the general title *Publications of the Technical University of Heavy Industry* in 1955. Four new series - Series A (Mining), Series B (Metallurgy), Series C (Machinery) and Series D (Natural Sciences) - were founded in 1976. These came out both in foreign languages (English, German and Russian) and in Hungarian. In 1990, right after the foundation of some new faculties, the university was renamed to University of Miskolc. At the same time the structure of the Publications was reorganized so that it could follow the faculty structure. Accordingly three new series were established: Series E (Legal Sciences), Series F (Economic Sciences) and Series G (Humanities and Social Sciences). The latest series, i.e., the series H (European Integration Studies) was founded in 2001. The eight series are formed by some periodicals and such publications which come out with various frequencies.

Papers on computational and applied mechanics were published in the

Publications of the University of Miskolc, Series D, Natural Sciences.

This series was given the name Natural Sciences, Mathematics in 1995. The name change reflects the fact that most of the papers published in the journal are of mathematical nature though papers on mechanics also come out.

The series

Publications of the University of Miskolc, Series C, Fundamental Engineering Sciences

founded in 1995 also published papers on mechanical issues. The present journal, which is published with the support of the Faculty of Mechanical Engineering and Informatics as a member of the Series C (Machinery), is the legal successor of the above journal.

Journal of Computational and Applied Mechanics

Volume 17, Number 1 (2021)

Contents

Contributed Papers